Estimation Techniques and Mitigation Tools for Ionospheric effects on GNSS Receivers

POLITECNICO DI TORINO

SCUOLA DI DOTTORATO

Research Doctorate Course in

Ingegneria Elettronica e delle Comunicazioni

XXVII Ciclo

Doctorate Dissertation

Estimation Techniques and Mitigation Tools for Ionospheric effects on GNSS Receivers

Rodrigo M. Romero Gaviria

Tutor

Prof. Fabio Dovis

Coordinator of the Research Doctorate Course

Prof. Ivo Montrosset

02 March 2015

To my family

Acknowledgments

I am extremely grateful to all those who contributed with valuable suggestions for the research activity presented in this thesis.

Foremost, I would like to express my sincere thanks to my supervisor, Prof. Fabio Dovis, for his guidance and help that I received during the past three years.

Special thanks to all of my colleagues, friends and family for their encouragement. Last but not least, I would like to express my gratitude to all those who were part, together with me, of that great family we called TRANSMIT.

Table of contents

Acknowledgments I

1 Introduction **1**

1.1 Research Objectives 3

1.2 Thesis Outline 4

1.3 Publications arising from this thesis 5

2 GNSS Signals and Receivers **7**

2.1 GNSS Overview 7

2.1.1 GNSS Infrastructure 8

2.1.2 GNSS Positioning 10

2.2 GPS and Galileo Signal Structure 12

2.2.1 GPS L1 Signal 13

2.2.2 Galileo E1 Signal 17

2.3 GNSS Receivers 20

2.3.1 Acquisition 22

2.3.2 Tracking 23

2.3.3 Position Velocity and Time 27

3 Ionospheric Scintillations **28**

3.1 The Ionosphere 28

3.2 Ionospheric Scintillations 33

3.2.1 Equatorial and Polar Scintillations 35

3.3 Scintillation Effects on GNSS Receivers 38

3.4 Measuring Ionospheric Scintillations with GNSS Receivers . . 40

3.4.1 Amplitude Scintillation 41

3.4.2 Phase Scintillation 44

3.4.3 Galileo Measurements 45

3.5 Modeling Ionospheric Scintillation for GNSS Signal Simulation 46

3.5.1 Global Ionospheric Scintillation Model (GISM) 46

3.5.2 WideBand Model (WBMOD) 47

3.5.3 Cornell Model 48

3.6 Summary 56

4 Monitoring of Ionospheric Scintillations over Equatorial Regions **57**

4.1 The Receiver Front End 58

4.2 Detrending Issues when Monitoring Amplitude Scintillations via $S4$ 63

4.3 Detrending Issues when Monitoring Phase Scintillations via *Phi60* 65

4.4 Ionospheric Scintillations over Vietnam: Campaign overview 72

4.4.1 Scintillation Monitoring with GPS 74

4.4.2 Scintillation Monitoring with Galileo 77

4.4.3 Strong Scintillation Activity over Hanoi 79

4.5 Summary 81

5 Radio Frequency Interference in GNSS 82

5.1 Classification of Interference 83

5.2 Interference Effect on GNSS Receiver Outputs 84

5.3 Potential Interference sources 86

5.4 Interference signal description 87

5.4.1 Continuous Wave Interference 88

5.4.2 Wideband Interference 90

5.4.3 Chirp Interference 92

5.5 Summary 93

6 Interference Effect in GNSS-based Estimation of Ionospheric Scintillation Activity 95

6.1 Scintillation - Interference Scenario 96

6.1.1 Effects on S4 97

6.1.2 Effects on Phi60 105

6.2 Characterization of Continuous Wave Interference on GPS Scintillation Measurements 111

6.2.1 CWI Effect According to Scintillation Level 111

6.2.2 CWI Effect According to Frequency Offset 118

6.2.3 CWI Effect According to Power 122

6.2.4 The Galileo Case 129

6.3 Summary 133

7 Countermeasures to Interference in GNSS **135**

7.1 Frequency Domain Techniques . . . 137

7.1.1 Notch filter . . . 137

7.2 Time Domain Techniques . . . 139

7.2.1 Pulse Blanking . . . 139

7.3 Space Domain Techniques . . . 140

7.4 Transformed Domain Techniques . . . 141

7.4.1 Wavelet Packet Decomposition . . . 144

7.4.2 WPD based Interference Mitigation . . . 145

7.5 Interference Mitigation in a Scintillation Scenario . . . 147

7.5.1 Notch filter study case . . . 148

7.5.2 Wavelet decomposition study case . . . 150

7.5.3 A Comparative case . . . 153

7.6 Summary . . . 155

8 Training Research and Applications Network to Support the Mitigation of Ionospheric Threats **156**

8.1 TRANSMIT PROJECT . . . 157

8.2 The TRANSMIT Prototype . . . 159

8.3 Scientific and Industrial Applications Reliant on GNSS (Processor overview) . . . 161

8.3.1 Processor Overview . . . 161

8.3.2 Carrier Tracking Architecture . . . 163

8.3.3 A user interface for the proposed tool . . . 166

8.4 Summary . . . 167

9 Final Conclusions and Future Activities **169**

9.0.1 Summary of Contributions 169

9.0.2 Future Work 172

Bibliography **173**

List of tables

2.1 GNSS frequency plans. 13

3.1 Characteristics of simulated signals. 52

3.2 Receiver configuration. 53

4.1 Hanoi Data Collection Set-Up 74

5.1 CWI scenario set-up. 89

5.2 WBI scenario set-up. 91

5.3 Jamming scenario set-up. 92

6.1 Scintillation-Interference scenario set-up. 98

6.2 Summarizing results of S4 peaks due to interference. 103

6.3 CWI effect according to scintillation level. 112

6.4 CWI effect according to frequency offset. 119

6.5 CWI Effect According to Power 123

List of figures

2.1 The effect of the clock bias on distance measurement. 12

2.2 GNSS frequency bands. 14

2.3 Auto-correlation and cross-correlation of GPS C/A codes. . . . 16

2.4 Typical Gold spectrum (amplitude). 17

2.5 Baseband power spectral density of GPS C/A and Galileo BOC(1,1) signals. 20

2.6 GNSS receiver model. 21

2.7 Example of Cross Ambiguity Function. 23

2.8 General model of tracking loop. 25

3.1 Typical day and night profiles of electron density in the ionosphere. 30

3.2 Illustration of scattering mechanism originating ionospheric scintillation. 34

3.3 Global frequency of scintillation disturbances at solar maximum. 35

3.4 Equatorial fountain effect. 36

3.5 Illustration of solar activity effect on the Earth's Atmosphere. 37

3.6 Receiver diagram for amplitude (power) measurements. 41

3.7 Receiver diagram for phase measurements. 44

3.8 Mechanization of Cornell model. 50

3.9 Scintillation histograms according to Cornell model inputs. . . 52
3.10 Comparison of estimated C/N_0. 53
3.11 Detrended signals. Amplitude. 53
3.12 Detrended signals. Phase. 54
3.13 Estimated C/N_0 vs Amplitude Histogram. 54
3.14 Detrended Phase vs Phase Histogram. 55
3.15 Scintillation Indices: $S4$. 55
3.16 Scintillation Indices: $Phi60$. 55
4.1 Simplified diagram of GNSS Receiver front end. 58
4.2 Accuracy vs. Power requirements for commercial oscillators. . 61
4.3 Signal Intensity detrending. Butterworth filter with delay. . . 64
4.4 Signal Intensity detrending. Butterworth filter with delay corrected. 64
4.5 Signal Intensity detrending. Mean value. 65
4.6 $S4$ for different Detrending Methods 65
4.7 Scintillation indices. $S4$ 66
4.8 Scintillation indices. *Phi60* 67
4.9 Differential phase experiment set-up 69
4.10 Amplitude scintillation indices for reference and target satellites 70
4.11 Corrupted phase vs Differenced phase 70
4.12 Differenced detrended phase vs Reference detrended profile . . 71
4.13 Power Spectral Densities of detrended phases samples 71
4.14 PHI60 comparison: Differential method vs. High quality oscillator 72
4.15 Installation Set-Up Hanoi 73

4.16 Processing scintillating signals with the software receiver. . . . 75

4.17 Detrended amplitudes for different PLL integration times. . . 76

4.18 $S4$ for different PLL integration times. 76

4.19 Detrended phases for different PLL integration times. 77

4.20 $Phi60$ for different PLL integration times. 77

4.21 Scintillation indices from GALILEO signals. $S4$. 78

4.22 Scintillation indices from GALILEO signals. $Phi60$. 78

4.23 Skyplot over Hanoi on 10/04/2013. 79

4.24 Recorded scintillation activity over Hanoi on 10/04/2013. $S4$. 80

4.25 Recorded scintillation activity over Hanoi on 10/04/2013. $Phi60$. 80

5.1 Potential interference sources in GNSS bands. 86

5.2 GPS Signal under CWI (1). 90

5.3 GPS Signal under CWI (2). 90

5.4 GPS Signal under WBI (1). 91

5.5 GPS Signal under WBI (2). 92

5.6 GPS signal under jamming interference (1). 93

5.7 GPS signal under jamming interference (2). 93

6.1 Illustration of a scenario where both scintillation and interference affect the GNSS signal. 96

6.2 SI vs. SI_{trend} in interference scenarios. Filter Detrending. . . 99

6.3 SI vs. SI_{trend} in interference scenarios. Mean value Detrending. 99

6.4 Detrended SI in interference Scenario. Filter Detrending. . . . 100

6.5 Detrended SI in interference Scenario. Mean value Detrending. 100

6.6 Measured S4 under CWI. 101

6.7 Measured $S4$ under WBI. AWGN case. 102

6.8 Measured $S4$ under WBI. Chirp signal case. 102

6.9 Signal intensity under CWI. 104

6.10 Detrended signal intensity under CWI: AGC disabled. 104

6.11 Measured S4 under Interference: AGC disabled, CWI case. . . 104

6.12 Measured S4 under Interference: AGC disabled, WBI case. . . 105

6.13 Phase observables under CWI. Phase Error. 106

6.14 Phase observables under CWI. Detrended Phase. 106

6.15 Phi60 under CWI. 107

6.16 PSD of detrended phases samples under CWI when not aligned with a spectral component 107

6.17 PSD of detrended phases samples under CWI when aligned with a spectral component 108

6.18 Phase scintillation measurements under WBI: AWGN case. (1) 108

6.19 Phase scintillation measurements under WBI: AWGN case. (2) 109

6.20 Phase scintillation measurements under WBI: Chirp Signal case.109

6.21 Phi60 under interference: Case AGC turned off: CWI 110

6.22 Phi60 under interference: Case AGC turned off: WBI 110

6.23 CWI effect in a weak scintillation scenario. 113

6.24 Phase errors PRN1. 114

6.25 CWI effect in a moderate scintillation scenario. C/N_0. 115

6.26 CWI effect in a moderate scintillation scenario. Scintillation indices. 116

6.27 Phase errors. 116

6.28 CWI effect in a strong scintillation scenario. C/N_0. 117

6.29 CWI effect in a strong scintillation scenario. Scintillation indices. 117

6.30 Phase errors. 118

6.31 CWI effect in a moderate scintillation scenario. $f_{offset} = 25KHz$ (1) 120

6.32 CWI effect in a moderate scintillation scenario. $f_{offset} = 25KHz$ (2). 120

6.33 CWI effect in a moderate scintillation scenario $f_{offset} = 525KHz$ (1). 121

6.34 CWI effect in a moderate scintillation scenario. $f_{offset} = 525KHz$ (2). 121

6.35 CWI effect in a moderate scintillation scenario $f_{offset} = 1025KHz$ (1). 122

6.36 CWI effect in a moderate scintillation scenario $f_{offset} = 1025KHz$ (2). 123

6.37 CWI effect in a moderate scintillation scenario. High Power Case (1). 124

6.38 CWI effect in a moderate scintillation scenario. High power Case (2). 125

6.39 CWI effect in a strong scintillation scenario. High power Case (1). 126

6.40 CWI effect in a strong scintillation scenario Moderate power case. 127

6.41 CWI effect in a moderate scintillation scenario Weak power case. 128

6.42 CWI effect in Galileo E1B signal (1). 130

6.43 CWI effect in Galileo E1B signal (2). 131

6.44 CWI effect in Galileo E1B signal (3). 132

6.45 CWI effect in Galileo E1B signal (4). 133

7.1 Notch filter frequency response. 138

7.2 Digital pulse blanking implementation. 139

7.3 Transformed Domain technique block diagram. 142

7.4 Transformed Domain technique within the receiver processing chain. 143

7.5 Wavelet Packet Decomposition. 145

7.6 Wavelet Decomposition. 146

7.7 Wavelet mitigation. 147

7.8 CWI in a strongly scintillating scenario (1). 149

7.9 Notch filter interference mitigation 149

7.10 Notch filtered mitigated signal 150

7.11 CWI in a strongly scintillating scenario (2). 151

7.12 Wavelet packet mitigated signal. 152

7.13 Spectra of mitigated signal. 153

7.14 Receiver outputs. 154

8.1 Schematic diagram of TRANSMIT prototype network and modeled data flow. 159

8.2 General overview of the processor. 163

8.3 Tracking architectures comparison. 166

8.4 Graphical user interface. 167

List of Acronyms

ACF	Auto Correlation Function
ADC	Analog to Digital Converter
AGC	Automatic Gain Control
AWGN	Additive White Gaussian Noise
BOC	Binary Offset Carrier
BPSK	Binary Phase Shift Keying
CAF	Cross Ambiguity Function
C/A	Coarse/Acquisition
C/N_0	Carrier-to-Noise-Density Ratio
CBOC	Composite Binary Offset Carrier
CCF	Cross Correlation Function
CDMA	Code Division Multiple Access
CW	Continuous Wave
CWI	Continuous Wave Interference
DLL	Delay Lock Loop
EA	Equatorial Anomaly
EGNOS	European Geostationary Navigation Overlay System
FLL	Frequency Lock Loop
FFT	Fast Fourier Transform
GISM	Global Ionospheric Scintillation Model
GLONASS	Global Orbiting Navigation Satellite System
GNSS	Global Navigation Satellite System
GPS	Global Positioning System

IF	Intermediate Frequency
IIR	Infinite Impulse Response
ISMR	Ionospheric Scintillation Monitoring Receiver
KF	Kalman Filter
LNA	Low Noise Amplifier
LO	Local Oscillator
MBOC	Multiplexed Binary Offset Carrier
NBI	Narrow-band Interference
NBP	Narrow Band Power
NCO	Numerically Controlled Oscillator
OCXO	Oven Controlled Oscillator
PLL	Phase Lock Loop
PSD	Power Spectral Density
PRN	Pseudo-Random Noise
PVT	Position Velocity and Time
RF	Radio Frequency
RFI	Radio Frequency Interference
SAKF	Scintillation based Kalman Filter
SBAS	Satellite-based Augmentation System
SI	Signal Intensity
SIS	Signal-In-Space
STEC	Slant Total Electron Content
TEC	Total Electron Content
TCXO	Temperature Compensated Oscillator
TD	Transformed Domain
UHF	Ultra High Frequency
USRP	Universal Software Radio Peripheral

VHF	Very High Frequency
vTEC	Vertical Total Electron Content
WAAS	Wide Area Augmentation System
WBI	Wide-band Interference
WPD	Wavelet Packet Decomposition
WT	Wavelet Transform
WBMOD	WideBand Model
WBP	Wide Band Power
XO	Cristal Oscillator

Chapter 1

Introduction

Navigation is defined as the science of getting a craft or person from one place to another. The development of radio in the past century brought fort new navigation aids that enabled users, or rather their receivers, to compute their position with the help of signals from one or more radio-navigation system [1].

The U.S. Global Positioning System (GPS) was envisioned as a satellite system for three-dimensional position and velocity determination fulfilling the following key attributes: global coverage, continuous/all weather operation, ability to serve high-dynamic platforms, and high accuracy. It represents the fruition of several technologies, which matured and came together in the second half of the 20th century. In particular, stable space-born platforms, ultra-stable atomic frequency standards, spread spectrum signaling, and microelectronics are the key developments in the realization and success of GPS [2].

While GPS was under development, the Soviet Union undertook to develop a similar system called GLObalnaya NAvigatsionnaya Sputnikovaya Sistema (GLONASS). Both GLONASS and GPS were designed primarily for the military, but have transitioned in the past decades towards providing civilian and Safety-of-Life services as well. Other Global Navigation Satellite Systems

(GNSS) are now being developed and deployed by governments, international consortia, and commercial interests. Among these are the European system Galileo and the Chinese system Beidou [2]. Other regional systems are the Japanese Quasi-Zenith Satellite System and the Indian Gagan.

GNSS have become a crucial component in countless modern systems, e.g. in telecommunication, navigation, remote sensing, precise agriculture, aviation and timing. One of the main threats to the reliable and safe operation of GNSS are the variable propagation conditions encountered by GNSS signals as they pass through the upper atmosphere of the Earth.

In particular, irregular concentration of electrons in the ionosphere induce fast fluctuations in the amplitude and phase of GNSS signals called scintillations [3]. The latter can greatly degrade the performance of GNSS receivers, with consequent economical impacts on service providers and users of high performance applications. New GNSS navigation signals and codes are expected to help mitigate such effects, although to what degree is still unknown. Furthermore, these new technologies will only come on line incrementally over the next decade as new GNSS satellites become operational. In the meantime, GPS users who need high performance navigation solution, e.g., offshore drilling companies, might be forced to postpone operations for which precision position knowledge is required until the ionospheric disturbances are over [4]. For this reason continuous monitoring of scintillations has become a priority in order to try to predict its occurrence. Indeed, it is a growing scientific and industrial activity, as evidenced in [5], [6], [7] and [8].

However, Radio Frequency (RF) Interference from other telecommunication systems might threaten the monitoring of scintillation activity. Currently, the majority of the GNSS based application are highly exposed to unintentional or intentional interference issues [9]. The extremely weak power of the GNSS signals, which is actually completely buried in the noise floor at the user receiver antenna level, puts interference among the external error contributions that most degrade GNSS performance.

It is then of interest to study the effects these external systems may have on the estimation of ionosphere activity with GNSS. In this dissertation, we investigate the effect of propagation issues in GNSS, focusing on scintillations, interference and the joint effect of the two phenomena.

1.1 Research Objectives

Having considered the basic motivations behind this work, the research was organized according to the following steps:

- Study and analyze the existing methods to monitor ionospheric scintillations with GPS. More specifically to understand the theoretical basis behind amplitude and phase scintillation measurements in order to clearly identify their merits and, more importantly, their limitations when implemented by means of GNSS receivers.
- Investigate and analyze the signal processing tweaks needed in order to monitor scintillations through low cost software receivers. In particular, the incidence that a low cost oscillator in the front-end has in the estimation of phase scintillations must be analyzed and overcome.
- Analyze and implement the necessary adjustments in the receiver signal processing in order to take advantage of new GNSS systems such as Galileo, in order to maximize the monitoring probes of the ionosphere from a single GNSS receiver.
- Investigate the most suitable methods for ionospheric scintillation simulation on GNSS signals to allow for controlled analysis and testing of receiver architectures when subjected to scintillating signals.
- Analyze and investigate the effects that Continuous Wave and Wideband interferences have over the estimation of scintillation activity with both GPS and Galileo signals. More specifically, perform analysis on the

basis of the interference signal characteristics such as power, bandwidth and frequency offset with respect to the GNSS signals.

- Investigate suitable interference mitigation techniques in order tailored to the type of interference signals under analysis. In particular, explore the feasibility of retrieving the original scintillation measurement once the interference signals has been partially or completely mitigated.

1.2 Thesis Outline

In order to give an overview, this section provides the outline of the thesis. The thesis is organized in eight chapters:

Chapter 1, the present, serves as an introduction to the thesis where the basic motivation and objectives of the research are described.

Chapter 2 provides an overview of the modern GNSS infrastructure and frequency plans. The GNSS receiver architecture is introduced along with signal processing operations the receiver has to perform in order to compute a position.

Chapter 3 introduces the phenomenon of ionospheric scintillations, the effects it has on GNSS signals /applications as well as the basis for estimating scintillation activities using GNSS receivers. It also gives an overview on scintillation models in order to simulate scintillating signals to test GNSS receiver architectures.

Chapter 4 discusses hardware and software considerations to take into account when deploying units to monitor scintillation activity. Results are demonstrated through a real data campaign that was ran over an equatorial region.

Chapter 5 gives an overview of of the main terrestrial sources potentially generating interference signals in GNSS bands. The effects these signals can

have over the GNSS receiver processing stages is also summarized, together with examples of common interferences in the GNSS context.

Chapter 6 introduces the effects of interference when monitoring ionospheric scintillations for several type of interferences. Then it will focus on the Continuous wave type interferences only, where several remarks are drawn based on different interference characteristics such as power and frequency offset.

Chapter 7 gives an overview of the existing mechanisms available in GNSS to counter interference signals. It then takes to analyse the use these techniques can have in a scintillation plus interference environment, in order to adequately retrieve scintillation information embedded in the GNSS signal.

Chapter 8 serves as an overview of the Marie Curie TRANSMIT project, which funded the research presented here, and the framework of which this work was performed. A collaborative software tool developed with project partners is also presented in this chapter.

Finally, Chapter 9 provides summary and remarks of the thesis.

1.3 Publications arising from this thesis

- Romero R., Dovis F., Ionospheric Scintillation: A Comparison between GPS and Galileo 4th International Colloquium on Scientific and Fundamental Aspects of the Galileo Programme, 2013. (Chapters 3 and 4).

- Romero R., Dovis F., Effect of interference in the calculation of the amplitude scintillation index S4. International Conference on Localization and GNSS (ICL-GNSS), 2013. (Chapters 5 and 6).

- Romero R., Dovis F., Towards Analyzing the Effect of Interference Monitoring in GNSS Scintillation . Mitigation of Ionospheric Threats to

GNSS: an Appraisal of the scientific and technological outputs of the TRANSMIT project, 2014. (Chapters 5 and 6).

- Romero R., Susi M., Vuckocvic M., Dovis, F., Andreotti M., Aquino M., A GPS and Galileo carrier tracking architecture robust to ionospheric scintillation. European Navigation Conference (ENC 2014). (Chapters 6, 7 and 8).

- Susi M., Romero R., Dovis F., Aquino M., Andreotti M. Design of a Robust Receiver Architecture for Scintillation Monitoring. In IEEE/ION PLANS 2014. (Chapters 6, 7 and 8).

- Shaikh M.M., Notarpietro R., Romero R., Dovis F. Impact of Ionospheric Horizontal Asymmetry on Electron Density Profiles Derived by GNSS Radio Occultation. In Proc. of Institute Of Navigation (ION) GNSS+ 2013. (Chapter 8).

Chapter 2

GNSS Signals and Receivers

This chapter gives a general overview of GNSS, presenting a summary of the infrastructure, positioning method and frequency plans. For GPS and Galileo a more detailed review on their signal structure is given, as signals from both of these systems will be the focus of the analysis in Chapters ahead. A summary of the the usual operations carried out by the GNSS receiver signal processing chain is also presented.

2.1 GNSS Overview

Before satellite navigation was developed, earlier radio navigation systems used terrestrial long wave radio transmitters instead of satellites. These positioning systems broadcasted a radio pulse from a known master location, followed by repeated pulses from a number of slave stations. The delay between the reception and sending of the signal at the slaves was carefully controlled, allowing the receivers to compare the delay between reception and the delay between sending . From this the distance to each of the slaves could be determined, providing a position estimate (fix) [10]. Examples of such systems are the long range terrestrial systems to date : DECCA, LORAN, and OMEGA.

The space age began in 1957 with the launch of Sputnik I by the Soviet Union. The pattern of Doppler shifts in the signals transmitted by the satellite and measured from a single ground station at a known position was discovered to be enough to determine the orbit of the satellite. It was then deducted that if the satellite orbits were known, a radio receiver measuring the Doppler shifts could determine its position on earth.

The first satellite based radio navigation system born from this concept was the U.S. TRANSIT, also known as NAVSAT (for Navy Navigation Satellite System). Early space-based systems such as TRANSIT and the Russian Tsikida provided two-dimensional high-accuracy positioning services. However, position fix frequency was dependant on latitude and only suitable for low-dynamic users. Such shortcomings led to the development of the U.S. GPS in the early 1970's [1].

GPS was envisioned as a satellite system for three-dimensional position and velocity determination. Its program was approved in 1973, when the number of satellites, their position and the relative inclination were optimized to ensure an adequate global coverage [10].

While GPS was under development, the Soviet Union undertook to develop a similar system called GLONASS. Other Global Navigation Satellite Systems (GNSS) aiming to provide global coverage are now being developed and deployed by governments, international consortia, and commercial interests. Among these are the European system Galileo and the Chinese system Beidou [2]. Other regional systems are the Japanese Quasi-Zenith Satellite System and the Indian Gagan.

2.1.1 GNSS Infrastructure

The elements that compose these systems can be categorized into three segments: Space segment, Control segment and User segment.

Space segment: the space segment is the constellation of satellites. Different systems have different orbits, including the orbit radium and the number of orbits. The first operational GPS satellite was launched in February 1989. As of January 2015, there are 31 active satellites in the GPS constellation. This is more than the designed 24 satellites, in order to provide redundant measurements to the receiver and guarantee global coverage in case of outages. GPS satellites are on six orbital planes with an inclination of about 55 degrees to the equator. The mean altitude of a GPS satellite is about $20200km$ above the surface of the earth with a linear velocity of around $3.9km/s$, giving an orbital period of 11 hours and 59 minutes.

The European system, Galileo, is planned to have 30 satellites on three orbital planes at $29600km$ altitude. At present it has three active In-Orbit Validation (IOV) satellites (out of four). Two additional satellites, the so called Full Operational Capability or FOC satellites were recently launched in August 2014, but unfortunately were placed in wrong orbits. The Russian GLONASS has 28 satellites in constellation with 24 in operation. The Chinese COMPASS possess at the moment 17 active satellites on orbits, which provide a regional coverage over the Asia-Pacific area.

Control segment: The control segment consists of a network of ground that continually monitor the satellites. It consists of master control stations, data uploading stations and monitoring stations. Their functions are to coordinate the activities between satellites, monitor the orbits and health status of satellites, synchronize the atomic clocks and exchange information for the construction of navigation messages.

User segment: The User segment consists of the GNSS receivers and the user community. The receivers can receive and process the GNSS signal to obtain their position and time. Based on this information, different applications are developed. Details of GNSS receivers will be explained in Section 2.3.

2.1.2 GNSS Positioning

Modern GNSS systems work on the principle of *trilateration*, an estimation of the position based on measurements of distances. If $\mathbf{u} = (x_u,y_u,z_u)$ and $\mathbf{s} = (x_s,y_s,z_s)$ are respectively the locations of a receiver and a satellite in the Earth Centered Earth Fixed (ECEF) coordinate systems, then the receiver to satellite vector $\mathbf{r}$ can be denoted as:

$$\mathbf{r} = \mathbf{s} - \mathbf{u} \tag{2.1}$$

The magnitude of $\mathbf{r}$ is defined as

$$r = \|\mathbf{r}\| = \|\mathbf{s} - \mathbf{u}\| \tag{2.2}$$

which is the geometric distance from the satellite to the receiver. In (2.2), r can be measured from multiplying the signal propagation time by the speed of light. As radio waves travel at a known speed, if the transit time of a signal from a transmitting station can be measured then the distance between transmitter and the observer can be determined. Each satellite transmits a long digital pattern (a pseudo-random code) as part of its signal at a given time. Timing information is embedded within the satellite ranging signal in order to enable the receiver to calculate when the signal left the satellite based on the satellite clock time. By noting the time when the signal was received, the satellite-to-user propagation time can be computed, thus, the distance is obtained from multiplying that propagation time by the speed of light.

In the case of GNSS the position reference of the transmitters are the satellites. Despite being in constant movement their position, $\mathbf{s}$, can be estimated with an error no larger than a few meters and passed down to the receiver through the navigation message. Only the position of the receiver $\mathbf{u}$ is unknown. Given distances to three satellites which locations are known, the receiver can compute his position unambiguously by solving the set of three independent quadratic equations. However, to accurately measure the travel

time of the signal it is necessary that the clocks at the satellites and receivers be maintained synchronized since the radio signals travel at about $3*10^8 m/s$, and a synchronization error of $1us$ would result in an error of $300m$ in distance measurement [2].

Clocks onboard satellites of a given GNSS constellation are synchronized. In the case of GPS, the synchronization is referenced to an internal system time scale called GPS system time. Atomic clocks onboard satellite are expensive and not a viable option for receiver manufacturing when compared to the inexpensive quartz oscillators. The requirement of a very expensive clock in the receiver is easily sidestepped by the use of a fourth satellite. The bias in the receiver clock at the instant of the measurements affects the observed transit times for all satellites in the same way. Therefore, the measured distance is in fact not the geometric range but a pseudorange, given by:

$$\rho = c[\tau + (\delta t_u - \delta t^s)] \tag{2.3}$$

where δt_u and δt^s are the offsets from the common system time of the receiver and satellite clocks. The latter is known, as the ground control segment of GNSS uploads to the satellites the correction for the system time offset, which is then broadcasted to the user via the navigation message. Substituting (2.3) into (2.2) leaves the receiver clock bias δt_u as the fourth unknown to be estimated in addition to the three coordinates of position (x_u,y_u,z_u). As a consequence, a minimum of four satellite signals are needed in order to compute a fix [2]. The concept of GNSS based location is shown in Figure 2.1.

GNSS positioning is then the solution to the following set of equations:

$$\begin{cases} \rho_1 = \sqrt{(x_{s_1} - x_u)^2 + (y_{s_1} - y_u)^2 + (z_{s_1} - z_u)^2} + c\delta t_u \\ \rho_2 = \sqrt{(x_{s_2} - x_u)^2 + (y_{s_2} - y_u)^2 + (z_{s_2} - z_u)^2} + c\delta t_u \\ \rho_3 = \sqrt{(x_{s_3} - x_u)^2 + (y_{s_3} - y_u)^2 + (z_{s_3} - z_u)^2} + c\delta t_u \\ \rho_4 = \sqrt{(x_{s_4} - x_u)^2 + (y_{s_4} - y_u)^2 + (z_{s_4} - z_u)^2} + c\delta t_u \end{cases} \tag{2.4}$$

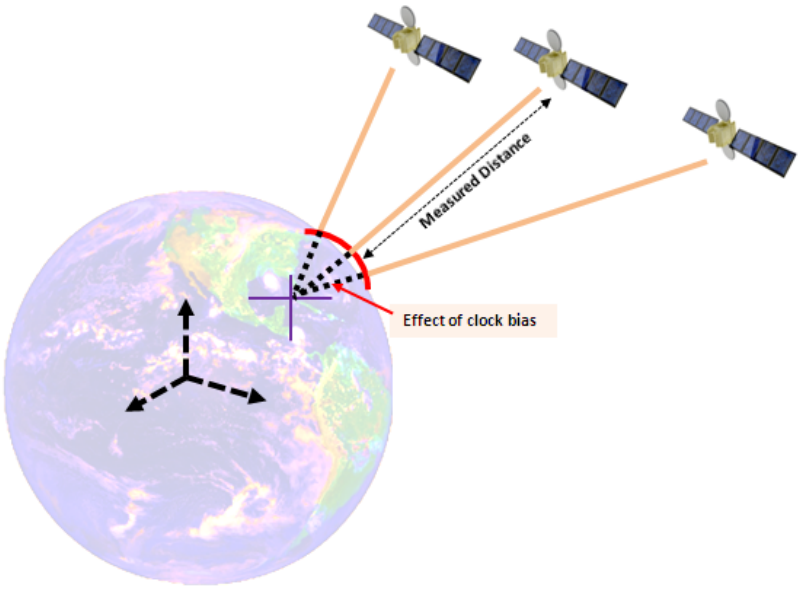

Figure 2.1: The effect of the clock bias on distance measurement.

Solving (2.4) gives the user location and the value of δt_u, allowing the user to synchronize its own receiver to the GNSS time scale [1]. If more than four satellites are in view then a better estimation of the positioning solution is achieved.

2.2 GPS and Galileo Signal Structure

GNSS systems broadcast different ranging signals on different carrier frequencies. Each ranging signal consists of a RF carrier which is modulated by a Pseudo-Random Noise (PRN) code and a data signal. The former allows the receiver to determine the travel time of radio signal from satellite to receiver. The latter carries the navigation message that is subsequently used by the receiver to determine the position of the satellites, clock bias parameters and other complementary information.

A summary of the frequency plans and modulation schemes for the four global systems is given in Table 2.1 and Figure 2.2 as in [11].

Table 2.1: GNSS frequency plans.

System	GPS	GLONASS	Galileo	COMPASS
Country	USA	Russia	European Union	China
Modulation / Coding	BPSK / CDMA	BPSK / FDMA,CDMA	BOC / CDMA	BOC / CDMA
Number of Satellites (Planned)	36	31	30	35
Carriers	-L1=1.57542GHz, -L2=1.22760GHz -L3=1.38105GHz -L4=1.37991GHz -L5=1.17645GHz	-L1,FDMA = 1602 + n × 0.5625 MHz -L2, FDMA =1246 + n × 0.4375 MHz -L1,CDMA=1.5754GHz -L2,CDMA=1.242GHz -L3,CDMA=1.20714GHz -L5,CDMA=1176.45GHz	-E1-L1-E2=1.559-1.592GHz -E6=1.260-1.300GHz -E5=1.164-1.215GHz	-B1=1.561098GHz -B1-2=1.589742GHz -B2=1.20714GHz -B3=1.26852GHz

GPS L1 C/A (Coarse/Acquisition) remains the GNSS signal most widely used for scintillation monitoring and will be reviewed in more detail in following sections. Galileo signals on the same band will also be reviewed, as they have been designed with the aim to be interoperable with the already existing GPS receiver infrastructure.

2.2.1 GPS L1 Signal

The GPS L1 signal consist of a civilian and a military signal. The civilian signal is usually referred as C/A signal and the military signal (transmitted also on a second band, L2) as P(Y). The transmitted signal on L1 can be written as:

$$x^{(k)}(t) = AP_k(t)D_k(t)\sin(2\pi f_{L1}t + \phi_1) + AC_k(t)D_k(t)\cos(2\pi f_{L1}t + \phi_1) \quad (2.5)$$

where $x^{(k)}$ is the signal from the *k-th* satellite, A is the amplitude of the P code; $P_k(t) = \pm 1$ and $C_k(t) = \pm 1$ are the binary P code and C/A code; $D_k(t)$ is the navigation data; f_{L1} is the L1 frequency; and ϕ_1 is the initial phase. Further analysis will focus solely in the in-phase component of (2.5), the civil signal C/A.

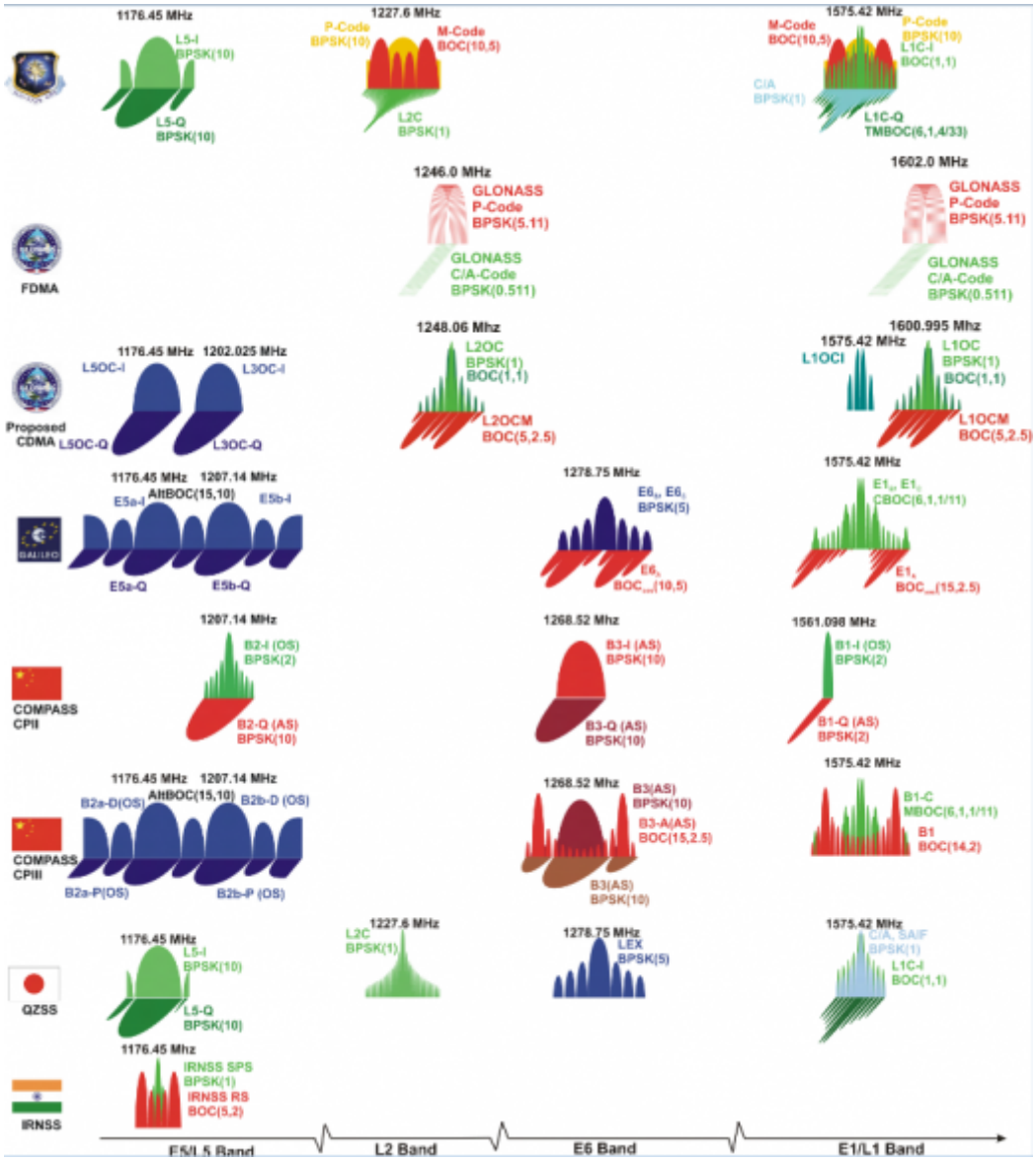

Figure 2.2: GNSS frequency bands.

2.2.1.1 Signal Amplitude

The signal amplitude for the *k-th* satellite is related to the transmitted signal power P_T as $A = \sqrt{\frac{P_T}{2}}$. The transmitted signal power level for the C/A code signal are set to guarantee a minimum received power level of $-160dBW$ for a user equipment employing a $0dBic$ antenna on the ground.

2.2.1.2 Navigation Data

Navigation data $D_k(t)$ is a binary sequence modulated onto the carrier frequency by means of Binary Phase Shift Keying (BPSK) modulation. Each +1 or -1 of the navigation data is called a bit, and the bit stream carries the information required from the satellite for position fixing. The rate of this data is different for different GNSS systems. In the case of GPS C/A this rate is $R_b = \frac{1}{T_b} = 50Hz$. The start of each data bit is perfectly synchronized with the start of the PRN code period.

2.2.1.3 PRN Code

For spread spectrum signals, the PRN code allows the use of very low power levels at the transmitting end by employing a very large bandwidth for the signal. The received signal is actually buried under noise floor. Due to this spreading, the transmitted signal appears as random noise to all the other system, avoiding data reading and more importantly, it allows the multiplexing of different satellite signals on a single carrier frequency. As was the case of the navigation data, the code uses BPSK to modulate the transmitted carrier. Each elemental pulse of +1 or -1 is called a chip, with a chip being much shorter than a bit. The C/A signal uses Gold codes due to their high auto-correlation and low cross-correlation properties. C/A codes have length of $L_c = 1023$ chips and rate of $R_c = 1.023Mcps$. The PRN codes of the C/A signal are periodic.

The key to successful operation of any GNSS receiver is the correlation property of PRN codes. If Doppler is zero, when the incoming code is correlated with a perfectly synchronized local code a peak is obtained, called auto-correlation function (ACF) peak. But if the correlation is carried out with a code of a different satellite we will get almost zero correlation, called cross-correlation function (CCF). This process, as seen in Figure 7.14, helps to identify different satellites and also to synchronize the local code of the receiver

with the incoming code.

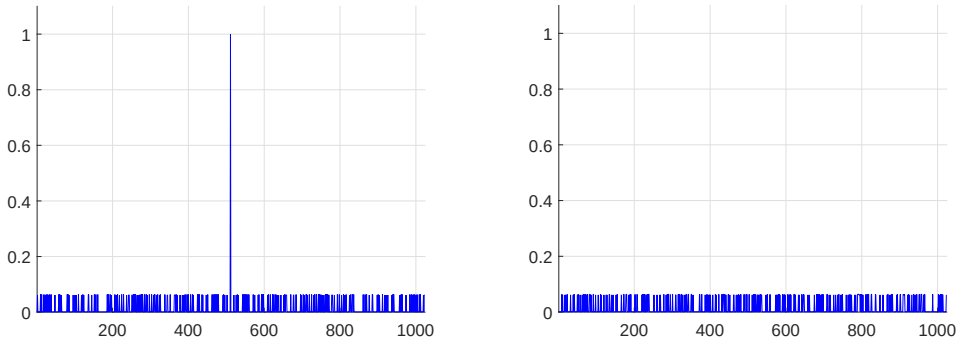

(a) ACF (b) CCF

Figure 2.3: Auto-correlation and cross-correlation of GPS C/A codes.

The ideal ACF is a delta function in the point where two codes are perfectly synchronized. However, some sidelobes appear which are very low compared to the main peak. When the time shift is constrained to be an integer multiple of a chip width, the ACF for any Gold sequence is equal to one of the four following values [2]:

$$< \mathbf{C_i}, \mathbf{C_i} > \in \left\{ 1, -\frac{1}{L_c}, -\frac{\beta(n)}{L_c}, \frac{\beta(n)-2}{L_c} \right\} \tag{2.6}$$

$$\beta(n) = 1 + 2^{\lfloor \frac{n+2}{2} \rfloor} \tag{2.7}$$

where $< \mathbf{C_i}, \mathbf{C_i} >$ represents the ACF of the PRN code from i-th satellite, $L_c = 2^n - 1$ is the length of the code and the symbol $\lfloor a \rfloor$ denotes the greatest integer larger than a. Unity autocorrelation only occurs for zero shift; the other values are the ACF sidelobes.

CCF of Gold codes take three values:

$$< \mathbf{C_i}, \mathbf{C_j} > \in \left\{ -\frac{1}{L_c}, -\frac{\beta(n)}{L_c}, \frac{\beta(n)-2}{L_c} \right\} \tag{2.8}$$

where $< \mathbf{C_i}, \mathbf{C_j} >$ represents the CCF between two different PRN codes from i-th and j-th satellites. ACF and CCF operations allow the receiver to separate the signals of different satellites and make the alignment between the local and received codes to achieve a coarse estimation of the signal received time.

The C/A code spectrum consists of discrete line components separated in frequency by the inverse code period, equal to 1 KHz, due to its periodicity. The lines are not uniform in height and have a $(\sin(x)/x)^2$ type power spectral envelope [10], as seen in Figure 2.4.

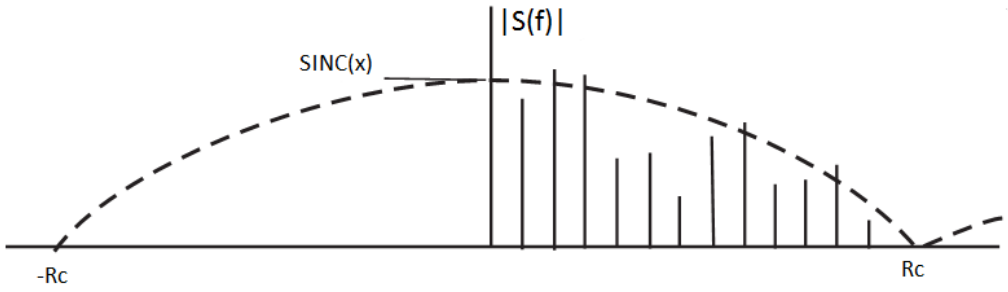

Figure 2.4: Typical Gold spectrum (amplitude).

When the GPS codes are combined with the 50 Hz navigation message data, there is essentially an imperceptible effect on the resulting autocorrelation functions [1]. However, the navigation message breaks the periodicity of the code. The final signal spectrum is a convolution of the C/A line spectrum with the narrow spectral component of the type $sinc(x)/x$ from the navigation message. When these are modulated onto the L-band carrier, there is a translation to L-band of the power spectrum from the baseband frequencies.

2.2.2 Galileo E1 Signal

The European Galileo system was designed to be inter-operable with the existing GPS. It shares with GPS some of the signal carrier frequencies: The E1 band has a carrier frequency at 1575.42 MHz as GPS L1 and the E5a has a carrier at are 1575.42 MHz, same as GPS L5. In this way, GNSS receivers can seamlessly combine GPS and Galileo signals in their positioning and timing applications.

The use of Galileo signals is expected to increase with the availability of the full Galileo constellation in the coming decade. It aims to provide a variety of new, high accuracy services such as [11] [12]:

- The Open Service (OS): Provides positioning, velocity and timing information that can be accessed free of direct user charge. This service is suitable for mass-market applications, such as in-car navigation and hybridisation with mobile telephones. The Open Service is accessible to any user equipped with a receiver, with no authorisation required. In general, Open Service applications will use a combination of Galileo and GPS signals, which will improve performance in severe environments such as urban areas.

- The Commercial Service (CS): Aimed at market applications requiring higher performance than offered by the Open Service. It provides added value services on payment of a fee. Galileo CS uses combination of two encrypted signals for higher data throughput rate and higher accuracy authenticated data.

- The Public Regulated Service (PRS): Will be used by groups such as police, coast-guards and customs. Civil institutions will control the access to the encrypted PRS. The PRS is operational at all times and in all circumstances, including during periods of crisis. A major PRS driver is the robustness of its signal, which protects it against jamming and spoofing.

- The Search and Rescue Service (SAR): Galileo satellites will be able to pick up signals from emergency beacons carried on ships, planes or persons and ultimately send these back to national rescue centres. From this, a rescue centre can know the precise location of an accident.

The whole transmitted Galileo E1 signal consists of the multiplexing of the three following components:

- The E1 Open Service Data channel $e_{E1-B}(t)$

- The E1 Open Service Pilot channel $e_{E1-C}(t)$

- The E1 PRS channel, also denoted as E1-A

Our focus is on the Open Service components. The E1 Open Service (OS) modulation receives the name of CBOC (Composite Binary Offset Carrier) and is a particular implementation of MBOC (Multiplexed BOC) [13]. MBOC(6,1,1/11) is the result of multiplexing a wideband signal, BOC(6,1), with a narrowband signal, BOC(1,1), in such a way that 1/11 of the power is allocated, in average, to the high frequency component. A data component given by:

$$e_{E1-B}(t) = d_{E1-B}(t)c_{E1-B}(t)s_{CBOC}(t) \tag{2.9}$$

and a pilot component given by:

$$e_{E1-C}(t) = c_{E1-C}(t)s_{CBOC}(t) \tag{2.10}$$

where $d_{E1-B}(t)$ is the navigation binary signal, $c_{E1-B}(t)/c_{E1-C}(t)$ are the spreading codes and $s_{CBOC}(t)$ are the Composite Binary Offset Carriers CBOC (6,1,1/11). The BOC modulation applies a squared subcarrier to a BPSK signal so that the maximum of the power spectrum is shifted with respect to the center frequency. For comparison, the Power Spectral Density (PSD) of the GPS C/A and the Galileo basic BOC(1,1) are shown in Figure 2.5. It is observed how the BOC is shifted with respect to C/A code PSD due to the presence of sub-carrier in the Galileo signal-in-space (SIS).

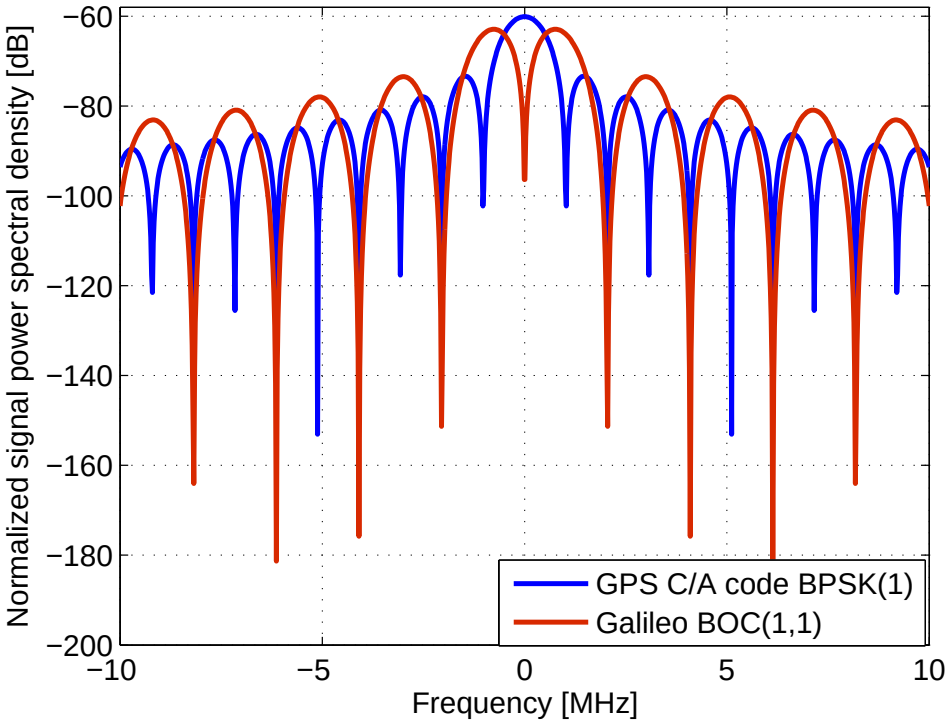

Figure 2.5: Baseband power spectral density of GPS C/A and Galileo BOC(1,1) signals.

2.3 GNSS Receivers

This Section gives an overview of the main operations performed by the GNSS receiver. More detailed information can be found in [1], [10] and [2]. The receiver model that will be used as foundation for our analysis can be seen in Figure 2.6.

The GNSS receiver is separated into two functional blocks: an analog part and digital part.

- Analog part: this part consists of the receiver antenna, mixers, filters, amplifiers and Analog-to-Digital Convertor (ADC). In this part, the signals are analogue. The main goal of this part is to receive the weak satellite signals, pre-amplify them and downconvert them from RF to

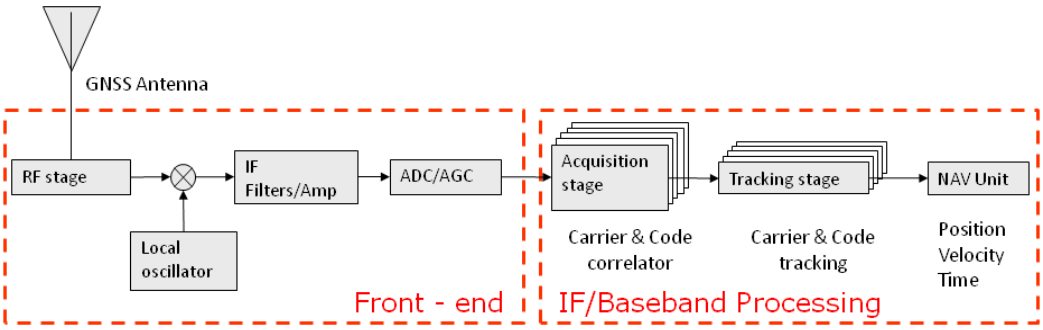

Figure 2.6: GNSS receiver model.

an Intermediate Frequency (IF), typically in the range of MHz. At the end of this part, the IF signals are sampled and converted to digits as input for the digital part.

- Digital part: It is the most critical part of a GNSS receiver. The main processes of this part are acquisition, tracking, demodulation of the navigation message and the PVT computation. In the design of these functions, important SIS characteristics (e.g.,Doppler range and rate) have to be considered. These functions can be implemented both in hardware and software.

The basic tasks of any GNSS receivers are:

- To capture and separate the Signals In Space (SIS) transmitted by the satellites in view;
- To measure the pseudorange of each received signal;
- To demodulate the navigation message;
- To estimate the Position, Velocity and Time (PVT).

These tasks take place in the digital part of the receiver and are described next.

2.3.1 Acquisition

The fundamental task of the receiver is to synchronize its local time scale with the satellite time scale, which is the GNSS time scale, in order to estimate the position by ranging measurements. The initial synchronization process takes place during the acquisition stage in all channels of the receiver in order to obtain a rough alignment between the codes broadcasted by the satellites and the locally generated ones [1][2].

Further analysis will focus solely in the in-phase component of (2.5), the civil signal C/A. The received GPS C/A signal can be written as:

$$y^{(k)}(t) = \sqrt{2P_R}C_k(t-\tau)D_k(t-\tau)\cos(2\pi(f_{L1}+f_d)t+\phi_1)+N(t) \quad (2.11)$$

where $y^{(k)}$ is the received signal from the k-th satellite, P_R is the total power of the signal; $C_k(t-\tau) = \pm 1$ is the C/A code; $D_k(t-\tau)$ is the navigation data; f_{L1} is the L1 frequency; f_d is the Doppler shift, ϕ_1 is the initial phase and $N(t)$ is the (non-filtered) noise contribution.

The received signal contains a number of unknown parameters like the PRN code delay, the Doppler frequency, the unknown carrier phase and the unknown data bits as it is seen from (2.11). In the acquisition stage only code delay and Doppler are treated as unknown parameters in order to restrict the computations to two-dimensions and fasten the whole process [1]. However, it is still a time consuming task, as the receiver must test all possible alignments (combinations of code phase and doppler shifts) until the correlation peak is detected. To do this, the receiver sets a search space, which is a grid of points to estimate the pair (τ,f_d) based on the evaluation of the Cross Ambiguity Function (CAF). CAF is defined as the correlation between the incoming signal and a local replica of the desired satellite signal to acquire, where the delay and Doppler shift are variable. Estimation is usually performed on the squared envelop of the CAF, in order to be insensitive to the phase of the incoming signal and also to the sign of the bits in case a data

channel is acquired. Figure 2.7 shows an example of CAF. More details on the acquisition strategy can be found in [1] and [2].

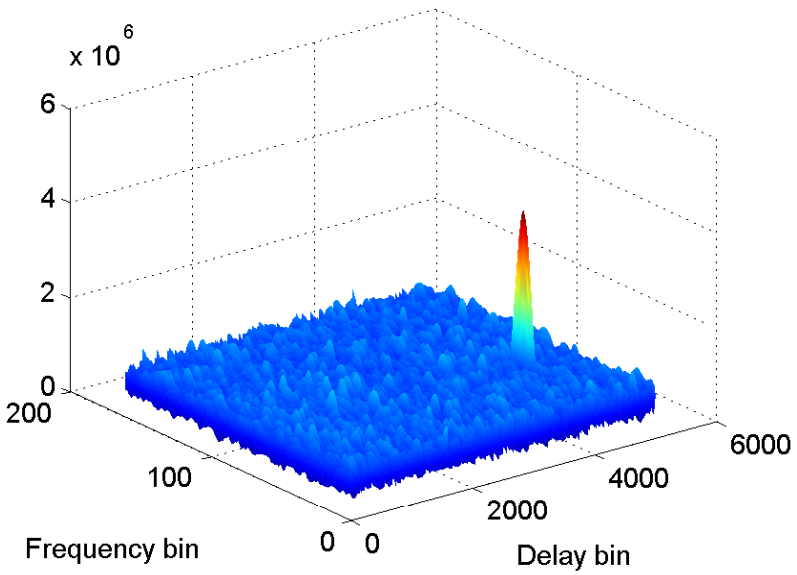

Figure 2.7: Example of Cross Ambiguity Function.

Modern acquisition strategies are based on the Fast Fourier Transform (FFT) to speed up the process by searching in parallel either the frequency doppler or the code delay [14]. These two parameters will be used by the tracking stage to precisely calculate the delay and frequency shift.

2.3.2 Tracking

The tracking stage is responsible of refining the code delay and doppler shift estimates from the acquisition and then keeping track of their evolution as the time passes. Two coupled loops are required, a Delay Lock Loop (DLL) for the code and a Phase Lock Loop (PLL) for the carrier tracking. The DLL continuously adjusts the local code replica to keep it aligned with the code of the incoming signal. When the two codes are perfectly aligned, the PRN code is removed from the signal (code wipe-off), leaving just the carrier modulated by the navigation messages. This signal is the input of the PLL,

which estimates the carrier frequency to perform a carrier wipe-off. After carrier wipe-off the DLL can synchronize the local carrier and the incoming carrier. This process continuously goes on during the receiver operations [1]. If any of the loops loses its lock the other loop automatically loses the lock.

Generally, the carrier loop is the weaker loop as the carrier wavelength is much shorter than the chip duration and also because the carrier loop has to track all the dynamics, while the code loop has to track only the dynamic difference between the carrier loop and the code loop in this aiding process [15]. For these reason, more emphasis is put on the improvement of the carrier tracking loops.

There is not only the PLL for carrier tracking but a variety of other architectures have been designed as well, such as frequency locked loop (FLL). The PLL is able to track both the instantaneous phase and frequency of the incoming carrier, while FLL is only able to track the carrier frequency. Other configurations include FLL assisted PLL and Kalman Filters based carrier tracking loops.

All three types of signal trackers, DLL, PLL and FLL, are sophisticated systems and can be modeled as control systems like the one shown in Figure 2.8. The first operation to be performed is the correlation between the incoming signal and a locally generated replica signal. During this operation, L samples of the incoming signal are mixed with the locally generated signal and the result is integrated to produce an output which is subsequently used by the discriminator. The most common approach in GNSS is to deploy a bank of well known early-prompt-late correlators, where early and late correlator outputs are used by the code discriminator while the prompt correlator is utilized by phase/frequency discriminators.

Discriminators are highly non-linear functions carefully chosen to extract the parameter to be estimated and suppress the effect of other unknown parameters. For example, the PLL discriminator must be sensitive only to carrier

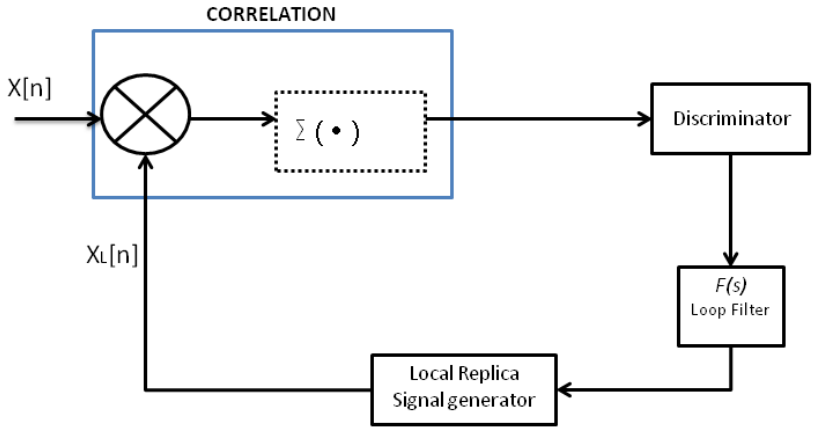

Figure 2.8: General model of tracking loop.

phase errors but insensitive to code phase errors and data modulation.

The loop filter is used to combine the present and past values of the error signal to estimate the code delay rate or phase rate depending on the loop type and produce the command signal for the local replica signal generator. Hence its function is two-fold: firstly, as the received signal and, thus, the discriminator output is corrupted by thermal noise, the filter is required to provide a degree of noise rejection. Secondly, it enables the processing of higher order dynamics.

The local replica signal generator is the *plant* that we wish to control. In PLL and FLL this local signal generator is usually the so-called numerically controlled oscillator (NCO) or simply local oscillator (LO) while in DLL it is usually termed as code generator (CG). The NCO in PLL or FLL is akin to the CG in DLL, except that it produces the replica carrier rather than the replica code.

The performance of the tracking stage of any GNSS receiver is assessed using two parameters:

- *Tracking Jitter*: Tracking jitter measures the capability of the loop to reduce the system noise which includes thermal noise and oscillator noise.

Oscillator noise is further categorized into vibration-induced jitter and Allan-deviation induced jitter of both satellite and user platform.

- *Dynamic Stress Error*: Dynamic stress error measures the capability of the loop to sustain the signal dynamics without losing the lock. This error depends on the loop noise bandwidth, B and order of the loop.

2.3.2.1 Tracking High Dynamic Signals

Given the signal dynamics normally encountered in GNSS applications a second order loop filter is sufficient to track through most of the changes in the signal. In the context of scintillations, particularly for moderate to strong activity, the higher dynamics encountered in the signal are better followed with a higher order loop, such as the classical third order loop. This filter can be used for unaided carrier loops, remaining stable for bandwidth of less than 18Hz [1]. The overall transfer function for a third order PLL is given by:

$$H(s) = \frac{2w_n s^2 + 2w_n^2 s + w_n^3}{s^3 + 2w_n^2 s + w_n^3} \tag{2.12}$$

where s is the Laplace variable and w_n is the natural frequency of the filter. The noise bandwidth of this filter is defined to be:

$$B_n = \frac{w_n(a_3 b_3^2 + a_3^2 - b_3}{4(a_3 b_3 - 1)} \tag{2.13}$$

where $a_3 = 1.1$ and $b_3 = 2.4$ are the filter coefficients, leaving the relationship between bandwidth and natural frequency as:

$$B_n = 0.7845 w_n \tag{2.14}$$

The classical third order PLL will be the one considered as tracking architecture for the analysis in the following chapters.

2.3.3 Position Velocity and Time

The PVT or navigation solution involves the simultaneous solutions of four unknowns: three dimensional position of the user's receiver and the receiver clock bias, as it was analysed in Section 2.4. PVT analysis does not make part of the work analysed in further sections, for more details on the system positioning solution the reader can refer to [2].

Chapter 3

Ionospheric Scintillations

Scintillations are random fluctuations in the received signal amplitude and phase. Isaac Newton was the first to associate this phenomenon with the atmosphere. Later, when astronomy moved to radio frequencies, its effects had been discovered by monitoring signals from other galaxies [16].

A GNSS signal, being allocated in the L band, is subject to amplitude and phase scintillations caused by its propagation through the ionosphere. The effect of signal scintillation is important for navigation and geodetic applications, because it affects receiver performance to a point where it may lose lock of the signals and stop tracking, thus not providing any positioning solution.

This chapter will review ionospheric scintillations in the context of GNSS. A summary of the effect at receiver level will be presented as well as the most relevant models of the phenomena in the context of satellite navigation.

3.1 The Ionosphere

How a radio signal propagates through the Earth's atmosphere depends to a great degree on the signal carrier frequency. Indeed, the atmosphere affects GNSS signals by causing ray bending, signal delays, and frequency, amplitude

and phase fluctuations. In the atmosphere, the ionosphere is a layer of ionized electrons surrounding Earth at altitudes from about 50 to 1000km.

Solar radiation and cosmic rays ionize the upper parts of the atmosphere and create free electrons and positively charged ions. The amount of solar radiation which reaches the Earth's atmosphere depends on time of day, time of year and the number of sunspots. Its intensity also varies through an 11 year solar cycle [16] [17]. A typical vertical profile of ionospheric electron density is divided into regions D, E and F according to different ionization and recombination principles [18]:

- **D region** is the lowest part of the ionosphere, extending from about 50 to 90km. This region is formed by two different layers: the D layer (with a maximum of ionization at about 65km) and the C layer (with a maximum of ionization at about 55km). During quiet conditions this region is present only at daylight hours; however additional D-layers may be produced at any time of day or night by high-energy electrons and protons originating from the sun, and associated with geomagnetic disturbances.

- **E region** extends from about 90 to 140km above the Earth. It is characterized by a single maximum of electron density, the E layer, at about 120km and it is mainly a diurnal region. The free electron concentration in this region is strongly dependent on the solar zenith angle, with a daily maximum in correspondence of the maximum elevation and a seasonal maximum in summer. During quiet conditions the E layer may have a residual of ionization at nighttime.

- **F region** extends from about 140 to 500km. During the day there are two separate layers in the F region, the F1 and F2 layers. At night these two layers combine to form a single F layer, usually called F2 layer. The F1 layer is the lower part of the daytime F layer. It exists only during daylight hours, disappearing at night. The F2 layer is present 24 hours

a day but varies in altitude with geographical location, solar activity, and local time.

Figure 3.1 shows the ionosphere layers together with their daily variation.

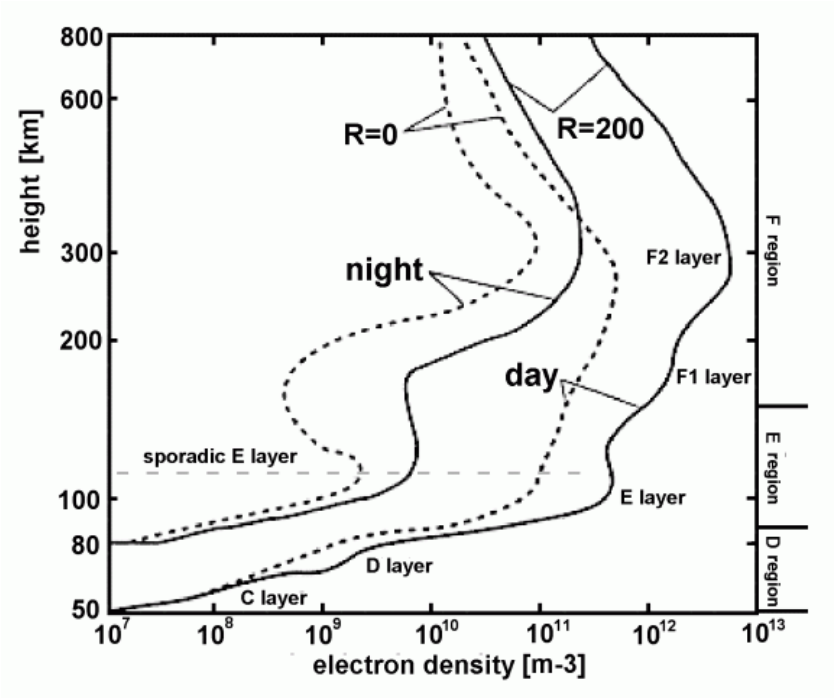

Figure 3.1: Typical day and night profiles of electron density in the ionosphere.

The ionosphere is a dispersive medium, as its refractive index and corresponding dielectric constant are dependent on signal frequency. The refractive index determines how is the signal propagation speed in the medium in relation to the signal propagation speed in vacuum or speed of light. This dependency is caused by plasma ionization and in turn is a function of the number of free electrons.

A GNSS signal in general, as seen in Chapter 2, consists of a carrier modulated by a spreading code. When the signal goes through the ionosphere the code is delayed and the carrier, on the contrary, is advanced according to the refractive index. If these effects are not accounted for, the measurements become corrupted by errors. Therefore, GNSS signal propagation through

the ionosphere should be modeled, and these models should be used when we retrieve code and carrier observables.

The total delay depends on refractive index along the ray path. Refractive index depends in turn on the Total Electron Content (TEC) from the satellite to the receiver antenna. TEC is defined as the total number of electron in a tube of $1m^2$ cross-section along the GNSS signal path trough the ionosphere. The slant TEC or sTEC is calculated along the ray path from a satellite to a receiver and is therefore a function of satellite and user position. Being unique to each user, sTEC can not be used for mapping the ionosphere. Therefore vertical TEC (vTEC) or TEC along the local vertical is used. Maps of vTEC can be supplied to users and each user should recalculate vTEC to line of sight sTEC for each satellite [16].

There are several possibilities to compensate for the ionospheric effect on GNSS signals. When performing single frequency measurements, ionosphere errors can be corrected in part by making use of Satellite Augmentation System (SBAS) service, if the receiver supports it, such as the U.S. Wide Area Augmentation System WAAS or the European Geostationary Navigation Overlay Service EGNOS to obtain information of the condition of the nearby ionosphere from a network of reference stations. Single frequency measurements also have the possibility to use reduced vTEC maps with model parameters broadcasted by GNSS satellites, as is the case in GPS and its background ionosphere model Klobuchar and Galileo with NeQuick . However, models provide only an approximate correction, for up to 70% of the ionosphere delay [10].

The Klobuchar model was developed in 1975 keeping in mind limited computation memory and capability of receivers, therefore, the model algorithm is very fast and has minimum complexity [19]. One of the main criteria of the algorithm design was to fit best the daily period with the largest TEC values, i.e. afternoon period. It is a single layer model, thus it does not require knowledge of vertical electron density profiles and can be implemented using

only ground-based observations, in this case a GPS global network. GPS satellites broadcast eight parameters for the single-layer model, which should be used by the single-frequency user to correct for the ionosphere delay. It is estimated that this model corrects for more than 50% of error due to the ionosphere [16].

NeQuick, on the other hand, is a more complex electron density model allowing to distinguish ionosphere features not possible to identify with Klobuchar model [20]. It is a multi-layer model able to calculate electron density profile at any given location in the ionosphere. Therefore, sTEC is obtained by integrating electron density along the line of sight and can be directly translated to the ionospheric error between any two given points [16]. A comprehensive comparison of background ionosphere models can be found in [21].

Errors can also be corrected entirely in the case of dual frequency measurements by taking advantage of the dispersive nature of the ionosphere [1]. This approach called ionosphere-free combination can remove about 99% of the ionospheric error [18].

However, a second group of ionospheric variations include sudden ionospheric disturbances or small rapid changes in the electron density. Even though these phenomena are often observed, they do not show any behaviour pattern and cannot be modeled by empirical models [21]. When these electron density irregularities appear in the ionosphere they can disrupt further the propagation of the radio waves, introducing fluctuations in amplitude and phase called scintillations [3].

The ionosphere drifts with respect to the earth at a velocity in the range of $100 m/s$ at low latitudes, velocity that may reach values ten times higher at high latitudes. When electron density irregularities are present, due to the motion of both the transmitter (satellite) and the medium (ionosphere) with respect to the receiver, scattering inside the medium causes the phase

fluctuations and concurrent intensity fluctuations in the signal known as scintillations [22]. Ionospheric scintillation is responsible for signal degradation of several telecommunication systems from the VHF up to the C band and affects in particular the performance of satellite based navigation systems. Following sections focus on this particular phenomenon.

3.2 Ionospheric Scintillations

Ionospheric scintillations, rapid fluctuations in the received signal amplitude and phase of transionospheric radio signals, are originated from a scattering effect in the ionosphere due to zones with irregular electron concentration.

The fact that the source of scintillations is in the atmosphere of the Earth was discovered in the 1950s by analyzing radio signals from other galaxies . Further research on these extragalactic sources and later research with satellite data have established that scintillation is caused specifically by TEC irregularities mostly in the F layer [16]. As presented in Section 3.1, electron concentration along the propagation path of satellite signals in the ionosphere cause GNSS signals to experience range delays when traveling through. However, under perturbed conditions electron concentration irregularities can induce scintillation phenomenon.

The irregularities causing scintillation can be classified in two major groups: Irregularities with enhanced ionization and irregularities with depleted ionization or plasma bubbles. According to the source, irregularities can be classified as either global large-scale irregularities or local small-scale ones. Large-scale irregularities originate through the influence of the sun and the geomagnetic field. Local irregularities may appear as a result of volcanoes eruptions, earthquakes, and other disturbances.

The wave scattering mechanism that cause scintillation depends on the size of the irregularities which cause the scattering in comparison to the Fresnel

zone. Fresnel Zone length is defined as the fundamental length scale when diffraction effects are important, as:

$$l_F = \sqrt{\lambda H} \tag{3.1}$$

where λ is wavelength and H is distance from a receiver to the Fresnel zone. In terms of scintillation, Fresnel length defines the scale at which irregularities produce amplitude scintillation when a receiver is at distances farther than H. The structures that are larger than that contribute directly to phase, as their contribution to amplitude is suppressed by Fresnel filtering[16].

During scintillation, the ionosphere does not absorb the signal. Instead, irregularities in the index of refraction scatter the signal in random directions with respect to the principal propagation direction. As the signal continues to propagate down to the ground, small changes in the distance of propagation along the scattered ray-path cause the signal to self-interfere, alternately attenuating or reinforcing the signal measured by the user. The average received power is unchanged, as brief, deep fades are followed by longer, shallower enhancements [23]. This process is illustrated in Figure 3.2.

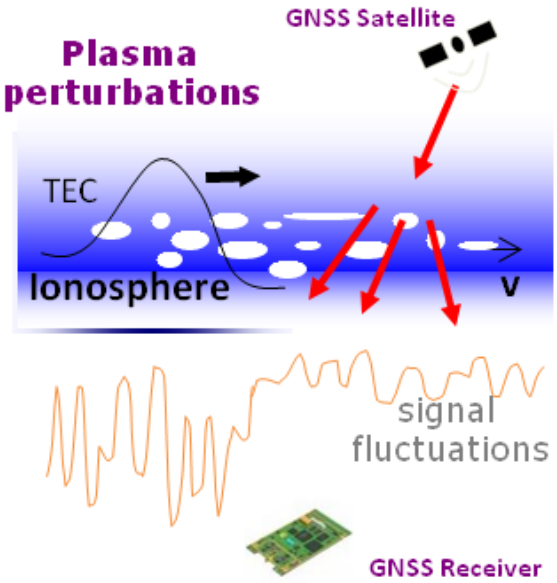

Figure 3.2: Illustration of scattering mechanism originating ionospheric scintillation.

3.2.1 Equatorial and Polar Scintillations

The geographic regions where the ionosphere shows to be highly irregular and hardly predictable are the equatorial bands extending from about 20°N to 20°S geomagnetic latitudes and the high latitude (auroral and polar cap) regions. However, scintillation that results from these irregularities has a global impact because for a receiver located at any place, the line-of-sight to some satellites may go through these portions of the sky. It is however rarely experienced at mid-latitude regions, occurring only in response to extreme levels of ionospheric storms or during solar maximum periods [24][25][26]. Figure 3.3 shows the global frequency of scintillations as in [24].

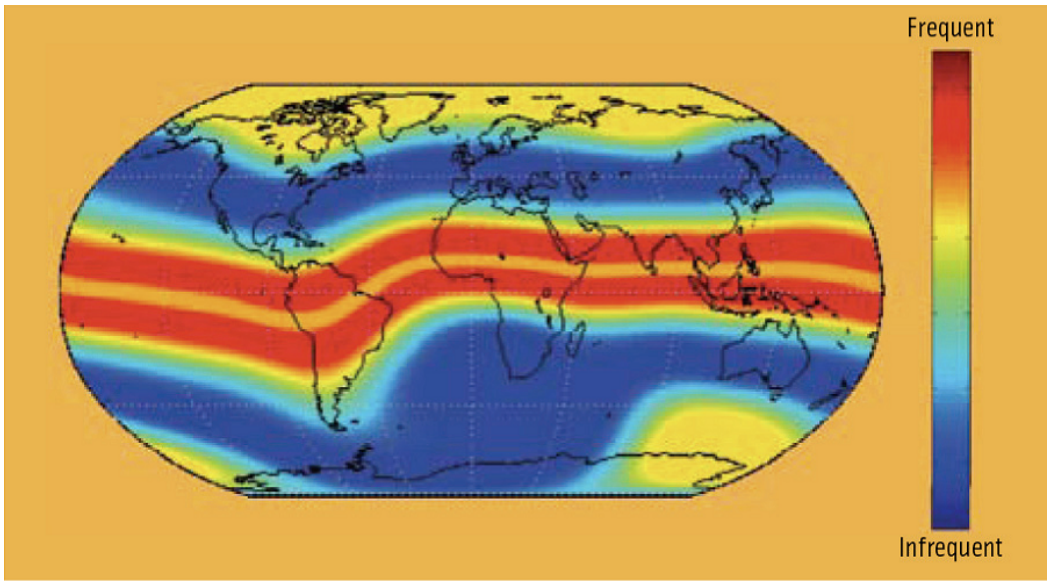

Figure 3.3: Global frequency of scintillation disturbances at solar maximum.

3.2.1.1 Equatorial Scintillation

Equatorial effects are mostly produced after the local sunset by the combined effects of the chemical recombination and the electrodynamic lifting of the ionospheric F-region by the Pre-Reversal Enhancement[27], a sharp upward spike in the vertical ion drifts velocity shortly after local sunset. Low

latitude ionosphere is characterized by the Equatorial Anomaly (EA): a region band extending from about 20°N to 20°S the magnetic equator that has high electron density concentration at F2 height. The Earth's magnetic field lines are horizontal at the magnetic equator. Solar heating and tidal oscillations in the lower ionosphere move plasma up and across the magnetic field lines. This sets up a sheet of electric current in the E region which, with the horizontal magnetic field, forces ionization up into the F layer, reducing ionization directly over the magnetic equator and increases the increasing it over the anomaly regions at $\pm 20°$ degrees from the magnetic equator. The word anomaly signifies that although the sun shines above the equator, the ionization attains its maximum density away from the equator [23]. This phenomenon is known as the equatorial fountain, as illustrated in Figure 3.4.

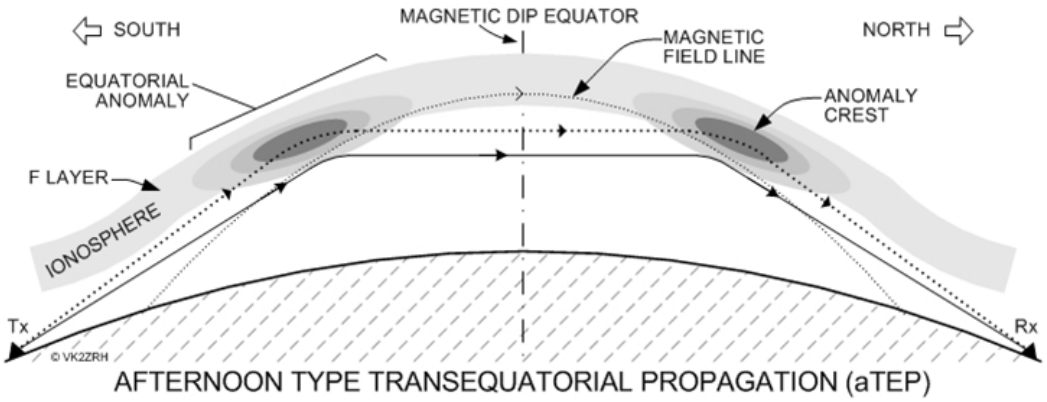

Figure 3.4: Equatorial fountain effect.

Plume-like structures or funnels contain rising bubbles with low electron density. If the size of the bubbles exceeds the Fresnel zone as observed from the ground station, the signal is affected by refraction. Diffraction comes into play when the size of the irregularities is equal to or smaller than the Fresnel zone. Bubbles when they are moving generate small irregularities, with size down to centimeters. These irregularities generate scintillation by diffraction [16]. Low latitude scintillation is seasonally dependent and it is limited to local nighttime hours.

3.2.1.2 Polar scintillation

The auroral and polar cap ionospheric phenomena, on the other hand, are mainly the result of geomagnetic storms which are associated with solar flares, coronal mass ejections and coronal holes. Here the main source of ionization is due to the collisions between the atmospheric components and the extra-terrestrial charged particles. The central polar region (greater than 75° magnetic latitude) is surrounded by a ring of increased ionospheric activity called the auroral oval. At night, energetic particles, trapped by magnetic field lines, are precipitated into the auroral oval and irregularities of electron density are formed that cause scintillation in the signals. A limited region in the dayside oval, centered closely around the direction of the sun, often receives irregular ionization from mid latitudes. As such, scintillation of satellite signals is also encountered in the dayside oval, near this region called the cups. Same phenomenon causes the aurora, the latter sometimes accompanying the scintillation occurrence. Figure 3.5 shows a concept of solar activity disturbing the Earth's atmosphere taken from [28].

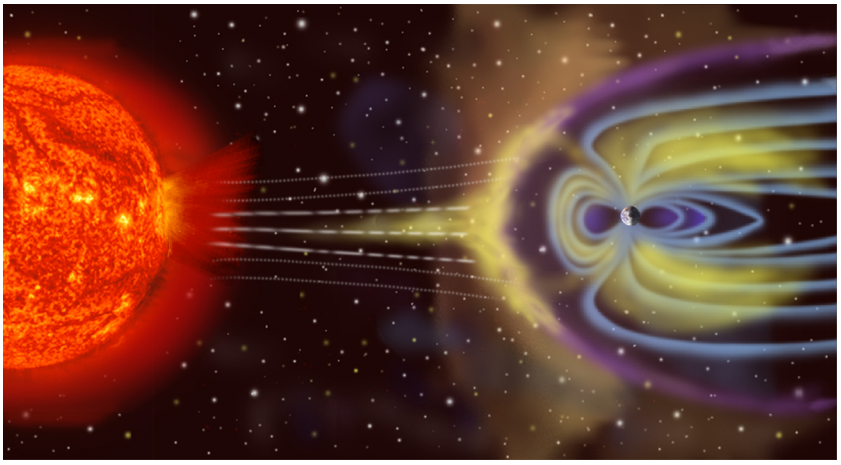

Figure 3.5: Illustration of solar activity effect on the Earth's Atmosphere.

In summary, scintillation affects signals depends on solar and geomagnetic

activity, season, local time and location. But being the ionosphere a dispersive medium, ionospheric scintillations are also a frequency dependent phenomenon: drops on signal power or large phase errors effects are greater on the L2 band when compared to L1, making signals transmitted in this frequency more susceptible to suffer outages during strong scintillation conditions. The impacts of scintillations are not mitigated by the same dual-frequency technique that is effective at mitigating the ionospheric delay. Such impacts are reviewed in the following section.

3.3 Scintillation Effects on GNSS Receivers

GNSS receivers performance itself can be greatly affected when tracking a scintillating signal. However, this fact, due to their global availability makes GNSS signals an excellent means to monitor and study ionospheric scintillations. The ever increasing reliance on GNSS systems have driven a marked research interest to improve the robustness of GNSS receivers to the threats posed by ionospheric disturbances, in particular during solar maximum periods when increases in the background TEC increase as well the periods of scintillations.

Most often scintillation will only affect one or two satellites and, if many well-distributed signals are available to the user, then the loss of one or two will not significantly affect the overall performance. But if the user has poor satellite coverage even modest scintillation levels can cause an interruption to user operations. When scintillation is very strong, many satellites could be affected significantly and even with excellent satellite coverage it can cause service interruption.

On user receivers, moderate to strong ionospheric scintillation activity can lead to:

- C/N_0 degradation.

- Increased noise in pseudorange and carrier phase measurements.
- Loss or corruption of the data bits.
- Cycle slips.
- Degradation of positioning accuracy.
- Loss of lock of satellite signals.
- Loss of positioning availability.

For these reasons, scintillations have become one of the most significant threats for GNSS operating in near equatorial and polar latitudes. However, the effects in amplitude and phase in these two regions may differ:

- **Amplitude Scintillation related effects**: Amplitude scintillations cause signals to fade. In equatorial regions the dominant effect of scintillation is in the amplitude. It can occur abruptly after sunset with rapid and deep fades that may persist until just after local midnight. In the equatorial anomaly regions fade can be as large as 20-30 dB during the most active ionospheric periods. Area coverage of equatorial scintillation ranges from tens to hundreds of kilometers, causing all users in such area to experience similar performance effects, since the geometry of their satellites will be essentially the same and they will experience similar levels of scintillation. If the combination is such that it causes a user to experience interruptions in service, then other nearby users will also likely be experiencing similar problems.

  Polar scintillation is less likely to create amplitude fades sufficient to cause signal loss, due to lower ionization levels with respect to equatorial areas. However,the effects may be correlated over hundreds of kilometers as well, with amplitude fades reaching up to 10dB.

- **Phase Scintillation related effects**: Phase scintillation describes rapid fluctuation in the observed carrier phase obtained from the receiver's phase lock loop. These irregularities can cause increased phase noise, cycle slips, and even loss of lock if the phase fluctuations are too rapid for the receiver to track. The most rapid phase changes are typically associated with the deepest signal fades (as the signal descends into the noise).

3.4 Measuring Ionospheric Scintillations with GNSS Receivers

Neglecting frequency Doppler and ionosphere delay for sake of simplicity, the mathematical expression for the current GPS L1 C/A civil signal affected by scintillation can be written as:

$$S(t) = A\delta A(t) D_{L1}(t) C_{L1}(t) sin(2\pi f_{L1} t + \varphi + \delta\varphi(t)) \tag{3.2}$$

where A is the signal amplitude, $\delta A(t)$ is the amplitude fluctuation due to scintillation, $D_{L1}(t)$ is the navigation data with a rate of 50Hz, $C_{L1}(t)$ is the PRN spreading code with period of $T = 1ms$, f_{L1} is the radiofrequency carrier, φ is the initial carrier phase and $\delta\varphi(t)$ is the phase fluctuation due to scintillation. Given the complexity of ionospheric electron concentration spatial distributions, measurements of scintillations resort to statistical estimations of the medium properties every certain amount of time.

Ionospheric Scintillation Monitoring Receivers (ISMR) are specialized GNSS receivers able to track and monitor scintillations in order to collect data that can be used to model the phenomenon, study its affects at receiver level and collect information to possibly predict its occurrence in the future. They are able to measure the amount of scintillation affecting a satellite signal in both amplitude and phase by making use of correlation data from the tracking

processing blocks. Two indices are employed for this end, usually computed over an observation interval $T_{obs} = 60s$: $S4$ for amplitude scintillation and $Phi60$ (σ_φ phase deviation) for phase scintillation. Details of the estimation of these indices is reviewed in the following Sections for GPS C/A signal, later on it is described for Galileo E1 civil signals in comparison with GPS calculations.

3.4.1 Amplitude Scintillation

$S4$ measures the amount of amplitude fluctuations due to scintillations in GNSS signals. As described in [5] and [29], it is the normalized standard deviation of the detrended Signal Intensity (SI) computed from the in-phase I_{Pk} and quadrature-phase Q_{Pk} prompt correlator samples over T_{obs}. Figure 3.6 gives an overview of the computations effectuated by the receiver in order to obtain the specified correlator samples.

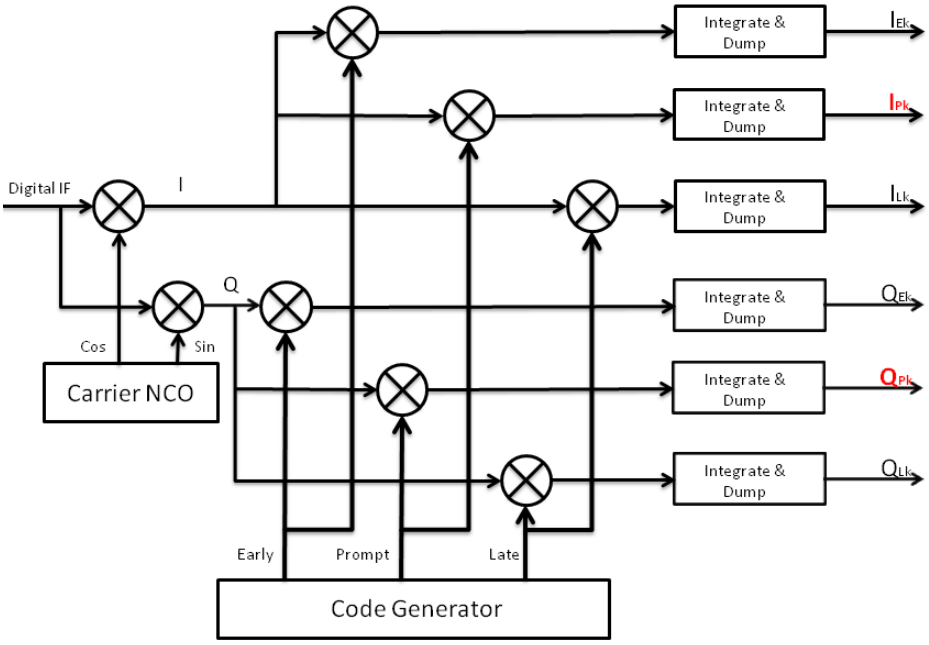

Figure 3.6: Receiver diagram for amplitude (power) measurements.

As a first step, the raw signal intensity samples SI_{raw} are calculated on the

basis of the power of the signal over two different bandwidths. This is accomplished through the *Narrow Band Power* (NBP) and *Wide Band Power* (WBP) estimators, expressed as:

$$NBP_k = (\sum_{k=1}^{M} I_{Pk})^2 + (\sum_{k=1}^{M} Q_{Pk})^2 \tag{3.3}$$

$$WBP_k = \sum_{k=1}^{M} I_{Pk}^2 + Q_{Pk}^2 \tag{3.4}$$

where I_{Pk} and Q_{Pk} are obtained every T_{int} milliseconds. In the GPS case, in order to avoid integration over a data transition, the product of M by T_{int} from (3.3) and (3.4) should be equal to 20ms. In this way NBP_k and WBP_k are obtained in synch with GPS navigation data. Thus for I_{Pk} and Q_{Pk} samples obtained every $T_{int} = 1ms$, M has a value of 20. If $T_{int} = 10ms$ then $M = 2$. The bandwidth of the WBP_k is $1/T_{int}$, whereas the bandwidth for NBP_k is $1/MT_{int}$. The raw signal intensity is obtained as the difference:

$$SI_{raw_k} = NBP_k - WBP_k \tag{3.5}$$

The rationale behind (3.3) through (3.5) is to obtain a quantity proportional to the received signal power while theoretically eliminating the noise contribution in the averaged value, as long as the gain of the receiver is constant. It can be assumed in (3.3) and (3.4) that $I_{Pk} = I + n_{I_{Pk}}$ and $Q_{Pk} = Q + n_{Q_{Pk}}$, where $n_{I_{Pk}}$ and $n_{Q_{Pk}}$ represent the in-phase and quadra-phase Gaussian white noise samples. Assuming the satellite signal is correctly tracked the noise samples can be averaged out [30]. In that case NBP_k, WBP_k and SI_{raw_k} can be approximated as:

$$NBP_k \approx (\sum_{k=1}^{M} I)^2 + (\sum_{k=1}^{M} Q)^2 = M^2(I^2 + Q^2) \tag{3.6}$$

$$WBP_k \approx \sum_{k=1}^{M} I^2 + Q^2 = M(I^2 + Q^2) \tag{3.7}$$

$$SI_{raw_k} \approx M(M-1)(I^2 + Q^2) \tag{3.8}$$

In practice, however, noise still remains and corrections to further eliminate its contribution are applied later. SI_{raw} samples must be detrended before calculating $S4$ in order to remove fluctuations due to satellite motion and possibly multipath. The signal intensity trend SI_{trend} is typically obtained by filtering the raw samples with a 6^{th} order Butterworth filter as described in [5], but can also be calculated as the mean value of the samples during T_{obs} as in [7]. The detrended samples are obtained dividing the raw samples by their trend:

$$SI = \frac{SI_{raw}}{SI_{trend}} \tag{3.9}$$

The total $S4$ is then calculated as obtained in [31]:

$$S4_T = \sqrt{\frac{\langle SI^2 \rangle - \langle SI \rangle^2}{\langle SI \rangle^2}} \tag{3.10}$$

where $\langle\rangle$ represents the average value over the interval of interest T_{obs}. If the carrier to noise density C/N_0 can be estimated during the interval, it is possible to have an estimate of the $S4$ due to noise:

$$S4_n = \sqrt{\frac{100}{C/N_0}(1 + \frac{500}{19 * C/N_0})} \tag{3.11}$$

The revised S4 without the noise contribution is then obtained as:

$$S4 = \sqrt{S4_T^2 - S4_n^2} \tag{3.12}$$

Amplitude fluctuations due to scintillations, δA in (3.2), follow a Nakagami-m probability density function given by:

$$p(\delta A) = \frac{m^m \delta A^{m-1}}{\Gamma(m)} e^{-m\delta A}, \delta A \geq 0 \tag{3.13}$$

Due to the properties of the Nakagami-m distribution, the S4 index cannot exceed $\sqrt{2}$. According to the S4 value, scintillation events can be roughly characterised as weak ($S4 \leq 0.3$), moderate ($0.3 < S4 \leq 0.6$), strong ($0.6 < S4 \leq 1$) and severe ($1 < S4 \leq \sqrt{2}$). The scaling of amplitude scintillations in

other GNSS frequencies with respect to L1 band is performed following the relationship given in [5]:

$$S4(f) = S4(L1)\frac{f_{L1}}{f}^{1.5} \tag{3.14}$$

3.4.2 Phase Scintillation

The phase fluctuations due to scintillations, $\delta\varphi$ in (3.2), follows a zero-mean Gaussian probability density function given by:

$$p(\delta\varphi) = \frac{1}{\sqrt{2\pi}\sigma_\varphi} e^{-\frac{\delta\varphi^2}{2\sigma_\varphi^2}} \tag{3.15}$$

Phase fluctuations due to scintillation are estimated as the standard deviation σ_φ of $\delta\varphi(t)$. Figure 3.7 presents an overview of the computations effectuated by the receiver in order to perform phase measurements, shown as $\phi_{estimate}$.

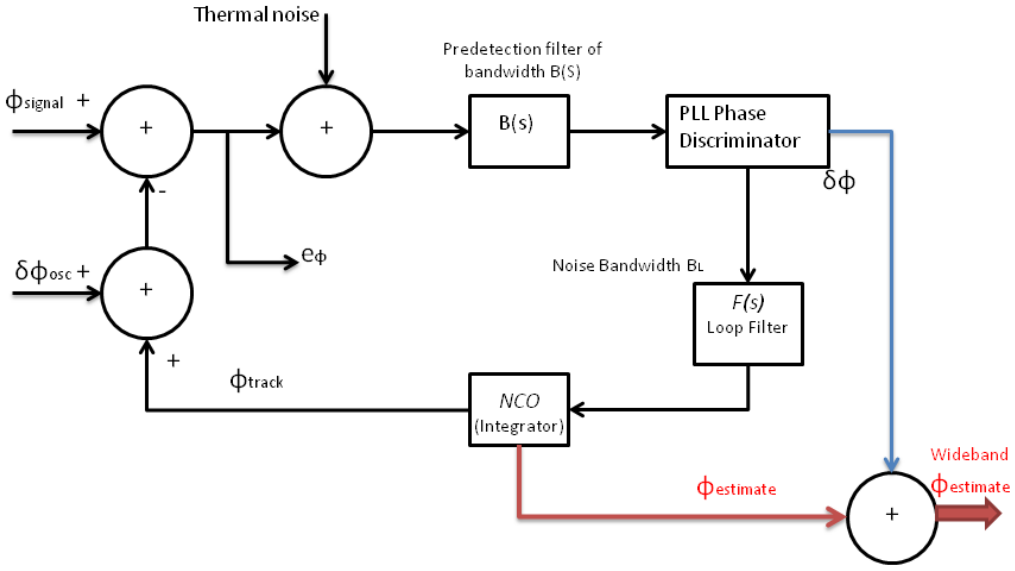

Figure 3.7: Receiver diagram for phase measurements.

Though it cannot be measured directly by the receiver, $\delta\varphi(t)$ can be estimated by detrending the carrier phase measurements $\phi_{estimate}$ from the satellite signals. The method widely used for detrending is to pass $50Hz$ phase measurements through a 6^{th} *order Butterworth high pass digital filter* with cutoff frequency of $f_c = 0.1$Hz as in [5], in order to isolate the high-frequency portions

of the carrier phase caused by the ionosphere from those slower variations due to satellite motion or multipath. Given that strong phase scintillations may contain power beyond the bandwidth of a typical PLL, measurements extracted from the carrier phase alone can be considered a filtered version of the true phase scintillations. To recover the high-frequency variations induced by scintillation up to the pre-detection bandwidth $B(s) = 1/T_{int}$, where T_{int} is the accumulation interval, the current PLL phase error from the phase discriminator must be added back onto the phase estimate. In this way the loop can be configured to have narrow loop bandwidth for robustness, but still provide wide bandwidth phase data [32].

The phase deviation σ_φ can be computed over 1, 3, 10, 30 and 60 seconds interval. These values are called *Phi1*, *Phi3*, *Phi10*, *Phi30* and *Phi60* respectively, being *Phi60* the most widely used. According to the σ_φ value, scintillation events can be roughly characterised as weak ($\sigma_\varphi \leq 0.25rad$), moderate ($0.25rad < \sigma_\varphi \leq 0.5rad$), strong ($\sigma_\varphi \leq 0.6rad$) and severe $\sigma_\varphi \geq 1rad$.

The scaling of phase scintillations to other GNSS frequencies with respect to L1 band is given by

$$\sigma_\varphi(f) = \sigma_\varphi(L1)\frac{f_{L1}}{f} \tag{3.16}$$

3.4.3 Galileo Measurements

There are differences of Galileo $E1$ Open Service signals with respect to GPS L1 C/A concerning the calculation of the ionospheric scintillation indices. The navigation data has a rate of $250Hz$ which makes it 5 times faster than that of the GPS satellites. The spreading codes with period of $T = 4ms$ have a duration 4 times longer than the GPS C/A [33].

To neglect the effect of the higher data rate, which would not allow us a coherent integration for the NBP computation in (3.3), the pilot signal e_{E1-C} can be used instead of the data modulated e_{E1-B} for scintillation measurements. In this case for I_k and Q_k samples obtained every integration time

$T_{int} = 4ms$, one would only need to change $M = 5$ in (3.3). By default, the rates at which I_k and Q_k are obtained in each system in order to calculate S4 would correspond to the periods of the spreading codes, that is, 1ms for GPS C/A and 4ms for Galileo e_{E1-c}. If $T_{int} = 20ms$ is set for both systems, a common output rate of correlator samples is obtained for comparison purposes. In this case, as observed in (3.8) the SI estimator is not suitable to calculate $S4$ given that $M = 1$. However, from (3.9) it is noticeable that SI_{raw} is normalized by its trend, so the scale factor $M(M-1)$ is cancelled out and have no incidence in the final SI value. Thus for the case of $T_{int} = 20ms$, SI can be replaced by the $50Hz$ raw signal power calculated as:

$$SP = I^2 + Q^2 \tag{3.17}$$

Phase scintillation measurements with Galileo signals follows the same procedure as in GPS, using as input the $50Hz$ carrier phase measurements.

3.5 Modeling Ionospheric Scintillation for GNSS Signal Simulation

Ionospheric scintillation simulation is necessary to assess the robustness of the phase tracking loops in GNSS receivers . Models are necessary to realistically reproduce the effects of scintillation on the signals. The first empirical model of scintillation was proposed by [34] in 1973 to estimate the S4 on VHF/UHF under weak scatter conditions. Some of the most widely known model nowadays for scintillation effects on GNSS bands are described in following Sections.

3.5.1 Global Ionospheric Scintillation Model (GISM)

GISM is a global climatological ionosphere model made of two parts. First, to describe the background electron density (irregularities) of the ionosphere,

it uses the *NeQuick* model developed by the University of Gratz and ICTP Trieste [20]. It requires as an input the geophysical data: solar flux number, the year, the day of the year and the local time, and returns as an output the electronic density average value for any point in the ionosphere (latitude, longitude, altitude). Second, the Multiple Phase Screen Algorithm (MPS) is the numerical model used to compute the irregularities effects (scintillation) on transionospheric radio signals. The inputs for the numerical model are the statistical information compiled from literature about the irregularities: spectral density, correlation length, altitude at which they develop and their velocity and direction of displacement. In the MPS algorithm the medium is divided into successive layers, each one being characterized by stationary statistical properties. It then iterates successively scattering and propagation calculations to output the scintillation index at the receiver. The total results of the model are presented in the form of maps of scintillation index $S4$ in geographic coordinates, but can also output statistical characteristics of the transmitted signals like the probability distribution functions of amplitude and phase fluctuations [35].

Fluctuations of the electronic density mostly develop at night-time at the ionosphere F layer altitude and at equatorial and polar latitudes. To account for these fluctuations in the model, a database has been constituted from results published in the literature. Still, these fluctuations or patchy character of the equatorial scintillation is not reflected in the model, as it predicts the same behavior for scintillation at different local times, changing only the scintillation intensity and not its morphology [36].

3.5.2 WideBand Model (WBMOD)

WBMOD is also a global climatological ionosphere model. As in GISM, it consists of an environmental model providing a worldwide climatology of the ionospheric plasma density irregularities: geometry, strength, orientation, and

motion of irregularities as a function of location (latitude, longitude), date, time of day, sunspot number and level of ionospheric disturbance k_p. It is based on extensive libraries of past scintillation data including equatorial and polar-cap data from Wideband, HiLat, and Polar Bear experiments and from the USA Air Force Phillips Laboratory equatorial scintillation monitoring network. The model can describe not only the signal fluctuations but also the plasma density irregularities that cause them [37].

A comparison between observations and WBMOD was also performed by [36]. It is shown that the model fails to reflect the patchy character of the equatorial scintillations. Rather than that, the model predicts the average behavior of scintillation as a function of time and position. For this reason, it fails to predict the scintillation on a given GPS link most of the time. Nevertheless, the authors claim that compared to GISM, WBMOD is more realistic as far as the reproduction of the diurnal scintillation variations is concerned.

3.5.3 Cornell Model

It is a statistical model that synthesizes ionospheric scintillation perturbations for testing carrier tracking loops of squaring type PLLs. Phase screen models and First-principles physics based models are computationally heavy and intense in term of parameterizations, but the Cornell model, in terms of parameters and computational expense, it is the simplest model that faithfully retains the scintillation properties that are relevant to carrier tracking. The model focuses in synthesizing realistic scintillation by properly shaping the spectrum of the entire complex scintillation signal, not the amplitude and phase data taken independently. If shaped independently, the obtained time scintillation history lacks canonical fades and becomes very easy for the receiver to track. In the Cornell model the scintillation time histories are drawn from a large library of empirical equatorial scintillation data from two

sources: Defense Nuclear Agency and WideBand Satellite Experiment, which comprises frequencies from VHF to S-band including and L-band signal very close to L2, and GPS L1 C/A code digital data, as summarized in [38] and [39].

3.5.3.1 Mechanization of Cornell Model

The output of the Cornell model is a complex signal represented by:

$$z(t) = \overline{z} + \xi(t) \tag{3.18}$$

where $\overline{z}$ represents the line of sight component, modeled as a complex constant and $\xi(t)$ represents the complex contribution from signals scattered in the ionosphere, also referred as the fading process. The latter is the dominant part under strong scintillation events. $\xi(t)$ has an autocorrelation function defined by:

$$R_\xi(\tau) = \frac{1}{2}E[\xi^*(t)\xi(t+\tau)] \tag{3.19}$$

The channel decorrelation time $\tau_0 > 0$ is defined as the value of τ for which $R_\xi(\tau)/R_\xi(0) = e^{-1}$. A narrow $R_\xi(\tau)$ (small τ_0) implies a scintillating channel that changes rapidly with time. Let $\alpha(t) \equiv |z(t)|$ and assume that $z(t)$ is normalized so that $\Omega \equiv [\alpha^2(t)] = 1$. Then, when no scintillation is present, $z(t) = 1$.

Focusing on the extensive library of strong equatorial scintillation at UHF and L-band frequencies, the best fits for the empirical amplitude distribution $p(\alpha)$ of $z(t)$ were found to be the Nakagami-m and the Nakagami-n (Rice) distributions. Rice distribution was chosen for the model due to its easier implementation. With that, $p(\alpha)$ is defined as follows:

$$p(\alpha) = \frac{2\alpha(1+K)}{\Omega} I_0(2\alpha\sqrt{K+K^2/\Omega}) e^{-k-\alpha^2(1+K)/\Omega} \tag{3.20}$$

where $\alpha > 0$ while $K > 0$ is the Rician parameter related to $S4$ by:

$$K = \frac{\sqrt{1-S4^2}}{1-\sqrt{1-S4^2}} \tag{3.21}$$

The definition of K in principle limits the values of $S4$ that can be modeled, but this limitation is not restrictive in practice since $S4$ takes on values near or below unity. To complete the scintillation model, the form of the auto-correlation function $R_\xi(\tau)$ must be specified. The model defines $S_\xi(\tau)$, the power spectrum of the fading process $\xi(\tau)$, as the frequency response of a low-pass filter with a second order roll-off. As $S_\xi(\tau)$ is related to $R_\xi(\tau)$ by the Fourier transform, $R_\xi(\tau)$ is obtained following:

$$R_\xi(\tau) = \sigma_\xi^2 e^(- \beta|\tau|/\tau_0)[\cos(\frac{\beta\tau}{\tau_0}) + \sin(\frac{\beta|\tau|}{\tau_0}] \tag{3.22}$$

where the factor $\beta = 1.2396464$ ensures that $R_\xi(\tau)/R_\xi(0) = e^{-1}$. The model can then be mechanized as shown in Figure 3.8 from [39].

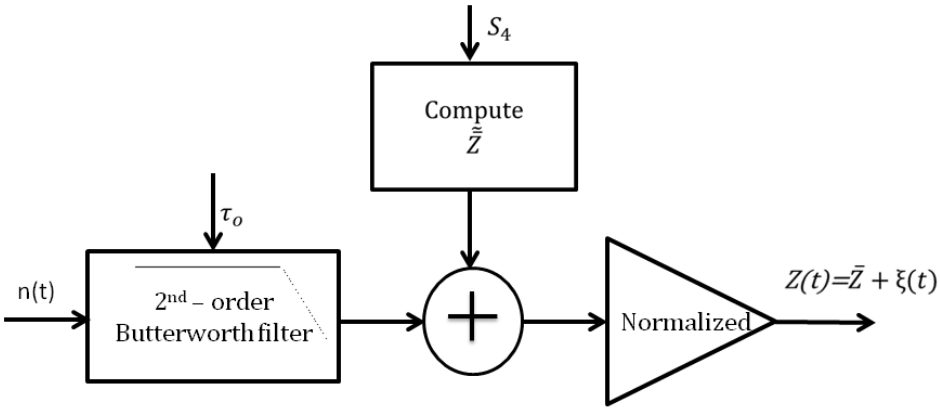

Figure 3.8: Mechanization of Cornell model.

The input parameters are the scintillation index $S4$ and the decorrelation time τ_0, which remain constant during the simulation. The simulator is driven by a stationary zero-mean complex white Gaussian noise process $n(t)$ with (two sided) power spectral density $N_0/2$. The process $n(t)$ passes through a second-order low-pass Butterworth filter with amplitude response function given by:

$$|H(f)| = \frac{1}{\sqrt{1 + (\frac{1}{f/f_n})^4}} \tag{3.23}$$

where $f_n = \beta/(\sqrt{2}\pi\tau_0)$ is the filter cutoff frequency, with β defined as in (3.22) and τ_0 being the desired correlation time. The resulting process $\tilde{\xi}(t)$ has

steady state variance $\sigma_\xi^2 \approx f_n N_0$. The constant value of the direct component $\tilde{\tilde{z}}$ is computed as:

$$\tilde{\tilde{z}} = \sqrt{2\sigma_\xi^2 K} \tag{3.24}$$

with K as defined in (3.21). The direct component is summed to $\tilde{\xi}(t)$ and the resulting process $\tilde{z}(t)$ is normalized by $\tilde{\alpha} = E[|\tilde{z}(t)|]$ to finally produce $z(t)$. The synthetic scintillation can then be used as in (3.25) and (3.26) to simulate the scintillation fluctuation in amplitude and phase of (3.2):

$$\delta A(t) = |Z(t)| \tag{3.25}$$

$$\delta\varphi(t) = \angle Z(t) \tag{3.26}$$

3.5.3.2 Simulation Results

The severity of the scintillation time history $z(t)$ is determined according to the combination of the input parameters S4 and τ_0. In general, higher $S4$ and lower τ_0 leads to more severe scintillations. $S4$ controls the range of the fluctuations in amplitude and phase, whereas τ_0 determines how fast such fluctuations occur. Figure 3.9 shows an example of four simulated scintillation profiles to illustrate this analysis.

To test the estimation algorithms of scintillation phenomena with the software GNSS receiver, several scenarios with different scintillation strength were simulated for both GPS and Galileo. Tables 3.1 and 3.2 present a summary of the input signal characteristics and the receiver configuration used during the tests.

The estimated C/N_0 for each one of the satellites can be seen in Figure 3.10. As observed, the stronger the scintillation the more fluctuations in signal power are present in the signals.

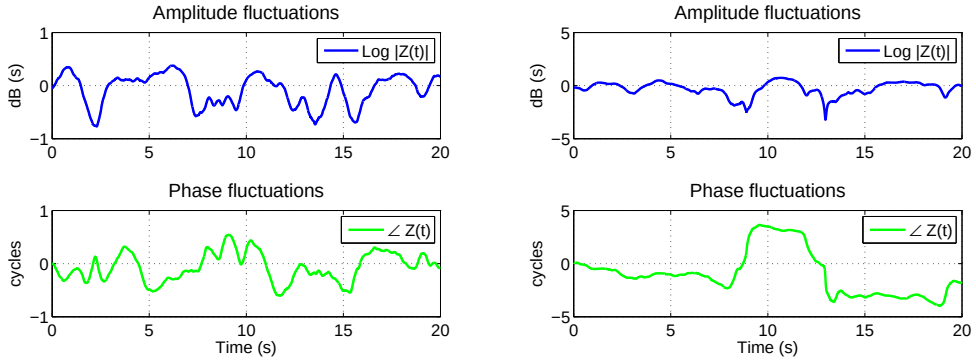

(a) $S4 = 0.5, \tau_0 = 1$ (b) $S4 = 0.8, \tau_0 = 1$

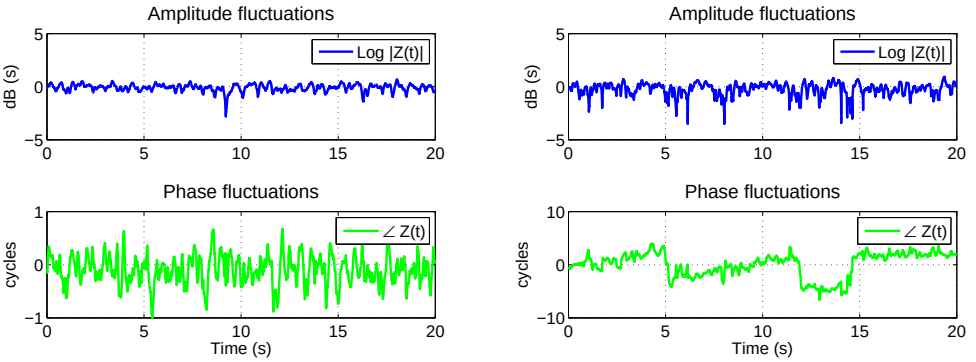

(c) $S4 = 0.5, \tau_0 = 0.1$ (d) $S4 = 0.8, \tau_0 = 0.1$

Figure 3.9: Scintillation histograms according to Cornell model inputs.

Table 3.1: Characteristics of simulated signals.

Parameter	**Value**
Signal	GPS L1 C/A - Galileo E1
Intermediate Frequency (IF)	3MHz
Sampling Frequency (F_S)	12MHZ
Front-end Bandwidth	4MHz
Number of Satellites	3
Nominal C/N_0	52 dB-Hz
Scintillation levels	Weak, S4=0.1 Moderate, S4=0.4 Strong, S4=0.7
Total simulation time	30 minutes
Scintillation start time	Minute 4

Following the procedures introduced in Section 3.4, both amplitude and phase must be detrended before calculating the ionospheric scintillation indices. The detrended signals can be seen in Figures 3.11 and 3.12.

Table 3.2: Receiver configuration.

Carrier Tracking Details	Value
Architecture	PLL
Filter Order	Third Order
Bandwidth	10MHZ
Time of integration (GPS)	1ms
Time of integration (Galileo)	4ms

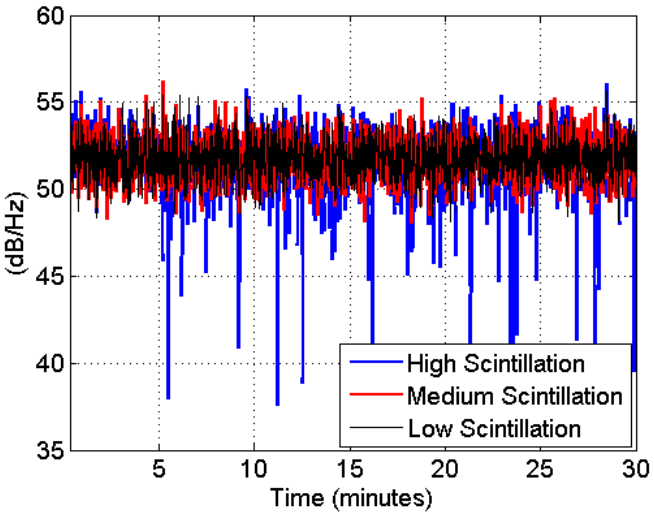

Figure 3.10: Comparison of estimated C/N_0.

To verify that the amplitude and phase variations actually follow the histograms generated through the Cornell model, Figure 3.13 compares one of

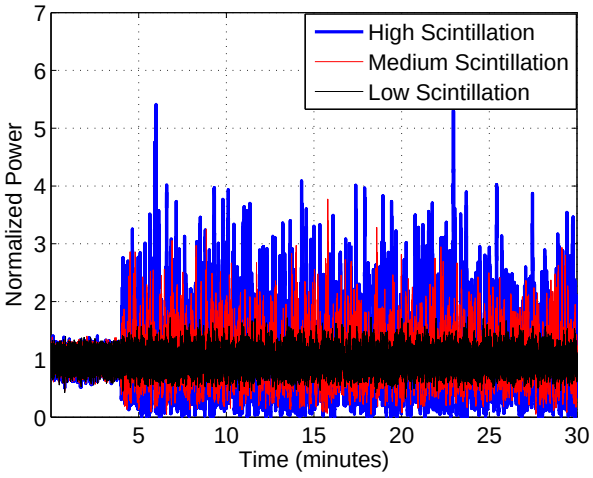

Figure 3.11: Detrended signals. Amplitude.

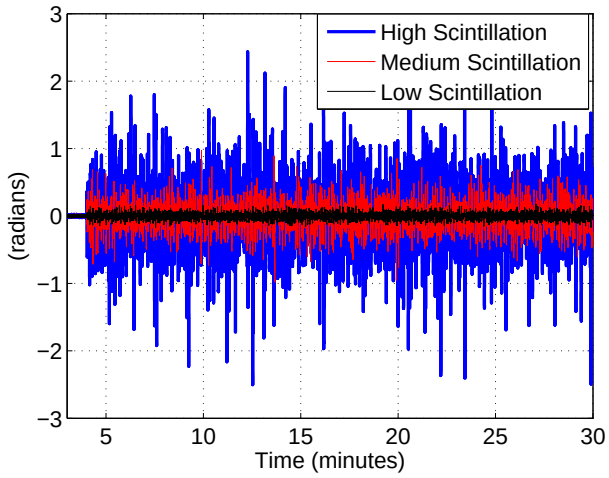

Figure 3.12: Detrended signals. Phase.

the measured C/N_0 with the corresponding amplitude histogram used for simulation of the amplitude fluctuations. As expected, the estimated signal power closely follows the input model, with slight variations due to the presence of the noise. For the phase case, Figure 3.14 shows the comparison of the detrended phase versus the corresponding phase histogram from the model.

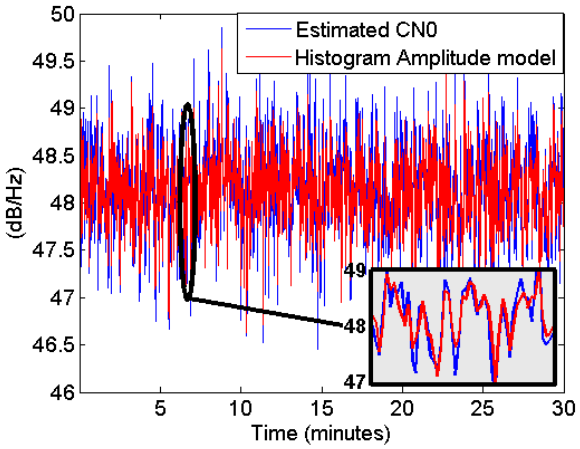

Figure 3.13: Estimated C/N_0 vs Amplitude Histogram.

Finally, after these operations, scintillation indices are calculated. Figures 3.15 and 3.16 show, respectively, the estimated $S4$ and $Phi60$ for each one of the three simulated scenarios.

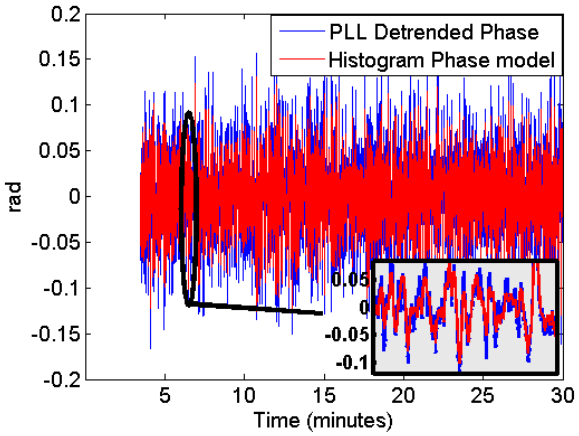

Figure 3.14: Detrended Phase vs Phase Histogram.

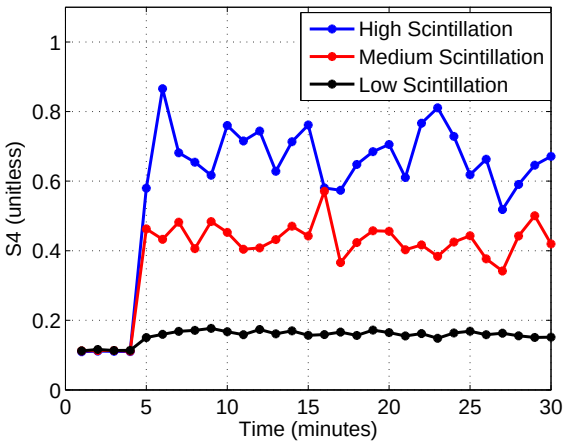

Figure 3.15: Scintillation Indices: $S4$.

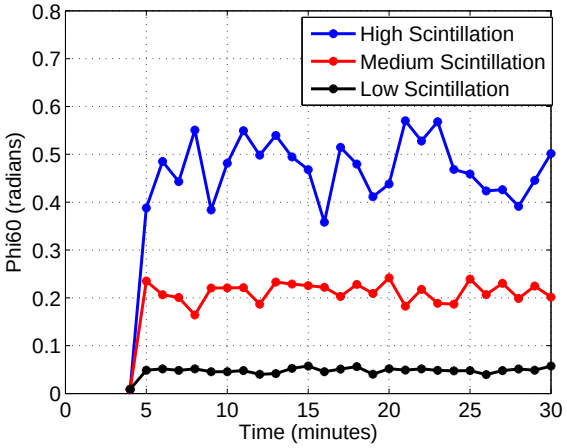

Figure 3.16: Scintillation Indices: $Phi60$.

3.6 Summary

This chapter gave an overview of key aspects of ionosphere concerning satellite systems. The ionosphere, if not accounted for, can be the largest error contributor in GNSS based navigation systems. Scintillations, random fluctuations in the signal amplitude and phase, were introduced as well and the particular geophysical aspects that lead to its formation in the ionosphere. Scintillations, as seen through the chapter, can greatly decrease the performance of GNSS receivers and related services. But given the continuous and global availability of satellite signals around the Earth, GNSS signals themselves are an excellent probe to get information of ionosphere activity. GNSS receivers can measure the amount of scintillation activity by the computation of two indices: S4 for amplitude scintillations and Phi60 for phase scintillations.

Several climatological models aiming to wrap and correlate different geophysical variables to describe the behaviour of scintillations in a global basis were introduced. Others, such as the statistical Cornell model that was also introduced, are effective for simulation of scintillation induces effect in GNSS signals for testing carrier tracking loops. The latter is an important for simulation of controlled scintillation scenarios to be tested in GNSS receivers.

Chapter 4

Monitoring of Ionospheric Scintillations over Equatorial Regions

Scintillation can serve as valuable source of geophysical information, in particular about atmosphere internal structure and its dynamics. Its particular effects may also be related to some as yet unexplored mechanisms in the atmosphere.In particular, by closely monitoring the fine structure and dynamics of the ionosphere we may be able to enhance weather forecasting, predict climate changes, get early warnings about hurricanes and typhoons, and even predict earthquakes.

In recent years, Ionospheric Scintillation Monitoring Receivers (ISMR) as in [8] and [5] have been deployed in different regions of the world to measure scintillation parameters and collect signal statistics on real time. Other lower cost GPS scintillation monitors as in [6] are also used to make detailed recording of all signal data to study the mechanics of the phenomenon, with statistics available after postprocessing.

There are important issues to take into account from the software and hardware point of view of GNSS receivers in order to properly output the measurements of ionospheric scintillation events in real-time or near real-time. In this chapter we will go into more details of the analog part of the receiver, the front-end, and the processing aspects to take into account in the digital part in order to properly estimate scintillation activity. Last section wraps up our analysis with the description of a scintillation monitoring system deployed in equatorial areas.

4.1 The Receiver Front End

The general block diagram of a single stage down conversion GNSS front end can be seen in Figure 4.2.

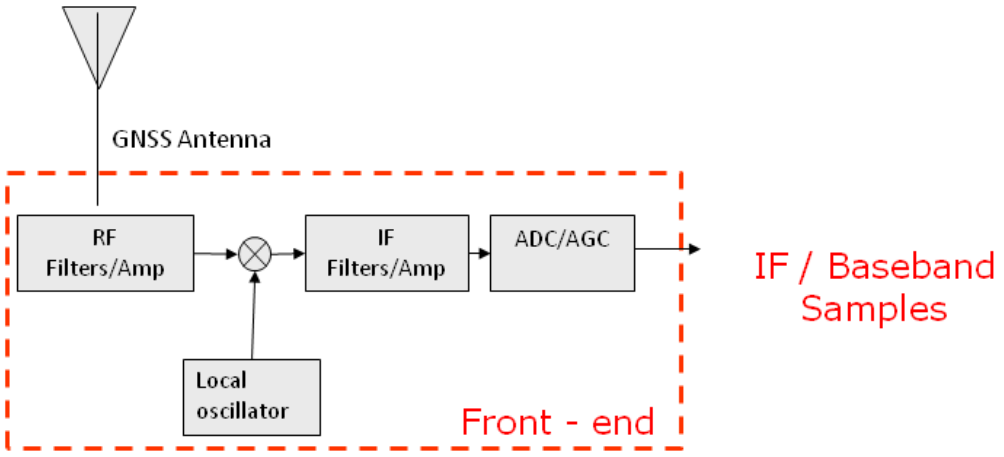

Figure 4.1: Simplified diagram of GNSS Receiver front end.

Receiving Antenna

The antenna is the first element of the receiving chain. Though not strictly a front end component, it is important to underline its main features. It connects the front end hardware to the physical world, inducing a voltage from the incident radio waves.

Antennas are characterised by its central frequency and bandwidth thus can also be modeled as a pass band filter. As an example, a GPS antenna usually has a bandwidth of about 2% of the signal center frequency. Therefore bandwidths for L1, L2 and L5 antennas are about 31.5 MHz, 24.6 MHz and 23.5 MHz respectively [1].

GNSS antennas are usually Right Hand Circularly Polarized (RHCP), because this is the orientation of the electric field propagating from the satellites. Another important parameter is the antenna pattern, that is related to the antenna gain (directivity). GNSS antennas are designed to receive the signal transmitted by the satellites, which for a terrestrial user, are all in view with a positive elevation angle. Therefore they usually have an hemispherical pattern. Other two parameters are the impedance and the Voltage Standing Wave Ratio (VSWR), which indicates how much of the incident power the antenna is able to absorb.

Filters

Filters are frequency selectors which only allows some frequencies to pass, attenuating the others. The band pass filter at the RF stage, often called preselector, has the main function to attenuate the power of out-of-band signals, which can saturate the following amplification stages. The preselector is also useful to reject the signals transmitted on the image frequency [40].

Despite the fact the antenna already filters the signal, the preselector is still needed due to poor filtering capabilities of some antennas. A second filter is also used at Rf stage in order to attenuate harmonics originated in the RF amplifier and suppress Local Oscillator (LO) energy that might propagate back to the antenna.After the frequency downconversion at an Intermediate Frequency (IF), filters at IF stage have the function to reject the terms out of the intended bandwidth, in particular the term centered on RF+IF at the mixer output. Similarly to the second filter at RF, a second filter at IF is then used to attenuate harmonics generated within the IF amplifiers and set

the front end overall bandwidth.

Amplifiers

The signal at the antenna output is extremely weak and needs to be amplified to match the analog input range of the ADC. The overall amplification is actually based on the specific ADC used in the front end, but generally is on the order of 100dB. Due to the low level of received GNSS signal power, the overall gain is computed considering only the noise power as there were no signals at the antenna. An ideal amplifier would simply increase the signal power at its input but in reality amplifiers are not linear components and introduce noise, which has to be taken into account in the front end design.

Mixer

The mixer is used to bring the signal down to IF. It simply multiplies the signal arriving from the antenna with a sinusoidal tone generated by the local oscillator. The result of this operation gives two different signals at the mixer output. Considering only one satellite and the in-phase component of (2.5), the signal at the mixer output can be written as:

$$\begin{aligned} s(t)|_{mix_out} &= D(t)C(t)\cos(2\pi f_{L1}t + \phi) \cdot 2\cos(2\pi f_{LO}t) \\ &= D(t)C(t)\cos(2\pi(f_{L1} - f_{LO})t + \phi) \\ &\quad + D(t)C(t)\cos(2\pi(f_{L1} + f_{LO})t + \phi) \end{aligned} \tag{4.1}$$

where

- f_{LO} is the frequency of the LO and depends on the overall frequency plan and on the desired IF. In general $f_{LO} = f_{L1} - f_{IF}$
- ϕ is the unknown phase offset between the incoming carrier and the LO.

Only the first term of (4.1) is of interest. It represents the code and the navigation data modulated on a carrier with a frequency equal to IF. This term passes through the first filter of the IF section, which instead rejects the second term at $f_{L1} + f_{LO}$.

Local Oscillator

The LO can be the most expensive item within the GNSS receiver [10]. In most of GPS receivers the oscillator is combined with a PLL for two reasons. The first is to generate frequencies other than the one generated by the oscillator such as the sampling and the signal processing clocks. The other is to clean up noise from the frequency by removing short term phase variation.

Through the quality of the digitized IF signal the clock parameters affect the baseband processor. The carrier and spread code of the incoming signal are affected by the clock drift, which may result in decreased signal acquisition capabilities and lower accuracy of the tracking loops.

Most commonly used clocks in GNSS receivers are Temperature Compensated Crystal Oscillators (TCXO). In high performance applications, the front end can be slaved to a more precise frequency reference such as the Oven Compensated Cristal Oscillator (OCXO) or even external Rubidium (Rb) standard. These references have superior stability when compared to the TCXO but are cost prohibitive for most applications and consume considerable more power. Figure 4.2 shows the relationship between accuracy and power requirement of several commercially available oscillators: a simple crystal oscillator (XO), the TCXO, OCXO and Rb frequency standard mentioned before, and a Cesium (Cs) frequency standard.

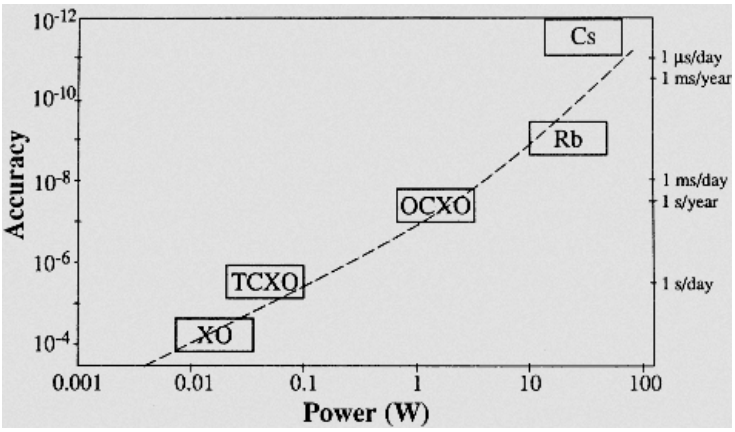

Figure 4.2: Accuracy vs. Power requirements for commercial oscillators.

Scintillation monitoring, as many geophysical applications, is based on analysis of the GNSS RF signal. For these cases, the observed effects should be significantly larger than background noise coming from the receiver implementation. In particular for scintillation measurements the receiver should have low phase noise, which is limited by the front end clock quality. Normally an OCXO is used, but through some signal processing tweaks it is possible to also use a TCXO, as will be explained in Section 4.3.

Analog to Digital Converter

The ADC is the last component of the front end and is needed to convert the analog signal to a digital form. Digitization includes two processes: signal sampling and quantization. Sampling of the band-limited analog signal can be viewed as a multiplication of the incoming IF signal by a periodic train of unit impulses. Quantization is the representation of each samples value by an N-bit word. The word can be in one of 2^N states. Therefore an analog IF signal can be represented by 2^N levels of the digitized IF signal. Most commercial receivers have 1 or 2 bit quantization [16]. Recently, the number of bits tends to increase since the good representation of the signal amplitude allows for the implementation of signal processing algorithms cleaning the signal from disturbances. Among all the parameters that characterize the ADC, it is worth to recall [41]:

- The analog input range, which represents the maximum signal dynamic allowed at the ADC input without causing damage to the device.
- Maximum sampling frequency.
- The analog input bandwidth.
- Number of bits to represent each sample

When the front end implements multi-bit quantization, an **Automatic Gain Control (AGC)** is required to adjust the signal at the ADC input. It can be

seen as an adaptive variable gain, whose main role is to amplify or attenuate the input signal in order to exploit the whole ADC analog input range and minimize quantization loses.

Digitized IF signal samples go then into the baseband processing where the acquisition and tracking take place. Next sections review aspects that must be taken into account when estimating the scintillation indices with GNSS receivers.

4.2 Detrending Issues when Monitoring Amplitude Scintillations via $S4$

Since the S4 index measures the fluctuations in amplitude due to any cause, the objective of the detrending process is to eliminate as best as one can other sources of amplitude fluctuations. A 6^{th} order low-pass Butterworth filter is employed to obtain the slow varying fluctuations due to satellite motion and possibly multipath (commonly avoided by use of elevation masks starting from 15° to 20°).

However, for receivers working on estimating the $S4$ index on real time the filter may pose a challenge due to its delay. As seen in (3.9) of Section 3.4, the signal intensity is detrended by dividing its samples by the trend obtained from the Butterworth filter. If the filtered signal SI_{trend} does not line up correctly with the raw samples SI_{raw} due to the filter delay, the detrending operation will increase the variance of the SI samples and as a consequence the $S4$ value is overestimated. One solution is the use of data buffering in order to calculate and correct for this delay. Figures 4.3 and 4.4 illustrate these situations, comparing the estimated signal intensity against the uncorrected and corrected outputs of the detrending filter.

Yet a simpler solution is the use of the mean value of the SI_{raw} as replacement of the output of the filter. Though faster, the latter provides a rougher trend

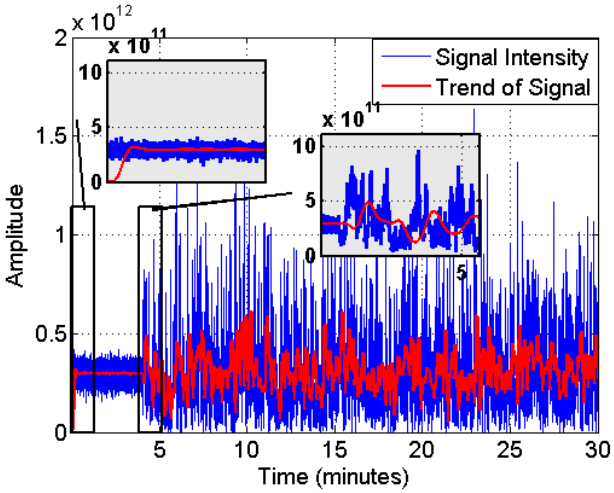

Figure 4.3: Signal Intensity detrending. Butterworth filter with delay.

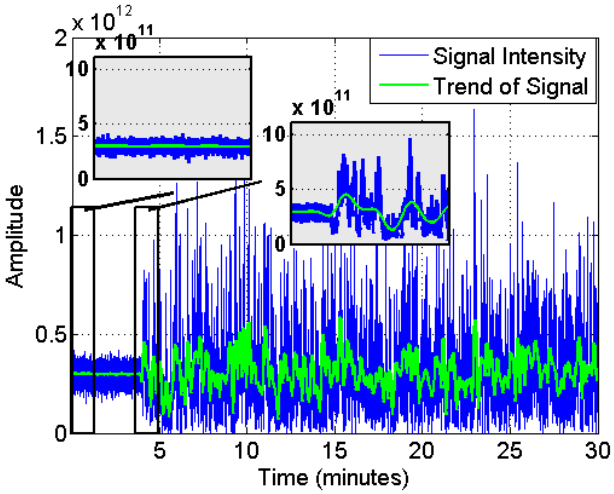

Figure 4.4: Signal Intensity detrending. Butterworth filter with delay corrected.

estimation in comparison with the filter due to the rather long time of observation to compute the index (60 seconds). Figure 4.5 compares the estimated signal intensity versus its trend obtained with the mean value method.

Once the trends are calculated, they are removed from the SI_{raw} samples and the operations continue to calculate the $S4$ as described in Section 3.4. The estimated amplitude indices can be seen in Figure 4.6 for the three cases of detrending signal treatment described above. It is clear that not accounting for the filter delay will be reflected in erroneous $S4$ values, while the

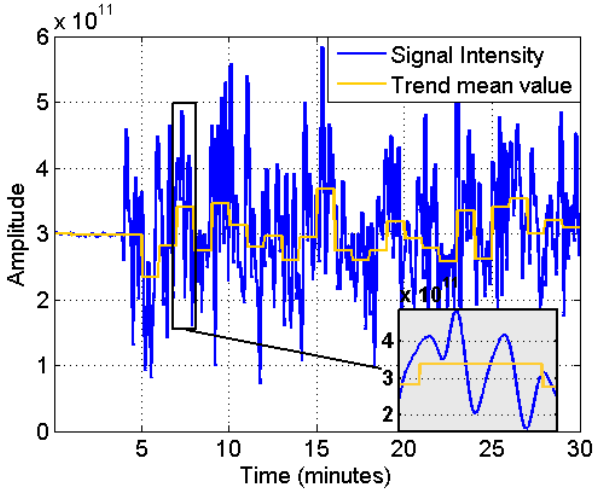

Figure 4.5: Signal Intensity detrending. Mean value.

mean value detrending trades-off easiness of implementation with a somewhat overestimated value of the index.

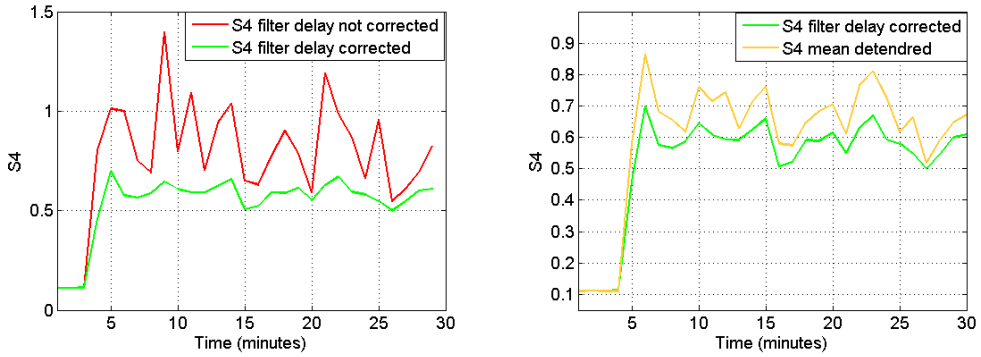

(a) Corrected vs not corrected delay of filter (b) Corrected delay vs mean value

Figure 4.6: $S4$ for different Detrending Methods

4.3 Detrending Issues when Monitoring Phase Scintillations via *Phi60*

While issues for the estimation of amplitude scintillation derived from a signal processing point of view, for phase scintillations the situation is different.

A specific hardware issue derived from the quality of the oscillator may impair completely the measurements. As seen in Section 4.1, TCXOs are the traditional oscillators used in GNSS receivers. While the phase noise level of the TCXO is sufficient for most of the GNSS range of services, in the case of phase scintillation monitoring it poses a problem due to being at the level or superior than the strongest phase disturbances scintillations can induce [42]. Replacing the TCXO with a more stable OCXO can solve this issue. However, the cost of an OCXO makes it prohibitive for mass deployment, as high quality oscillator such as the OCXO can easily be the most significant cost item of a modern receiver. The phase noise of a TCXO can effectively bury weak to moderate phase scintillations under the noise negating the possibility of detecting the phenomenon. In practice not only the oscillator, but any defective equipment increasing the phase noise in the system may potentially impair phase scintillation measurements. Figures 4.7 and 4.8 offer an example of how such a situation may look like when estimating scintillation indices from an equatorial scintillation data collection case.

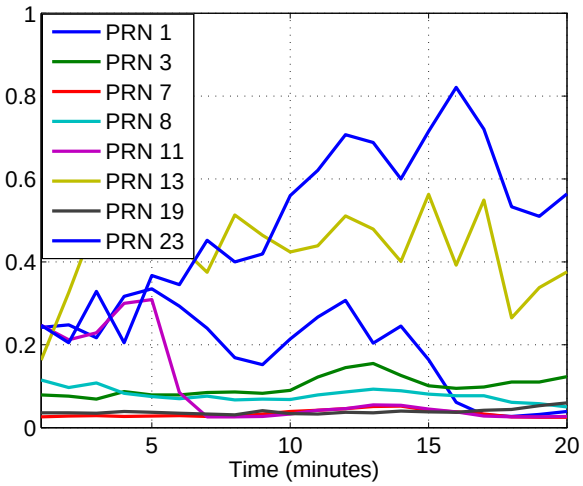

Figure 4.7: Scintillation indices. $S4$

As observed in Figure 4.7, the $S4$ was estimated correctly. However, it is seen in Figure 4.8 that $Phi60$ shows the same behaviour for all satellites in view. Moreover, the extremely high values reported are beyond any expected value

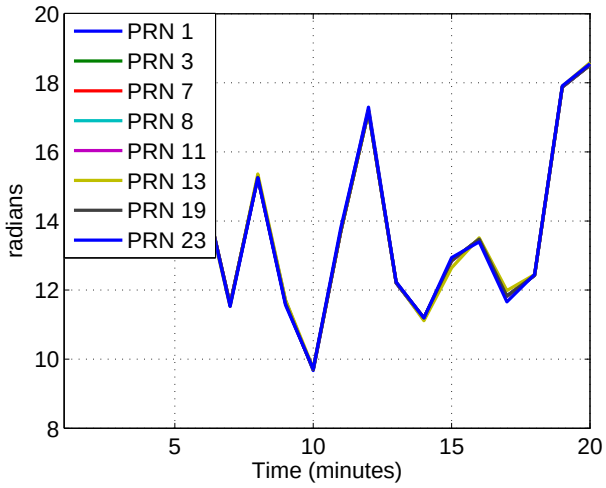

Figure 4.8: Scintillation indices. *Phi60*

of the phase index, even for strong scintillation cases. It is to be considered that for severe phase scintillation scenarios, σ_φ assumes values around 1 radian [43].

Scintillation indices being equal for all satellites in case of detected events is not likely since their value depends on the particular portion of the ionosphere crossed by each signal. This situation is an indication of very strong phase noise above the level of phase scintillations affecting the receiver. As a consequence, all satellite phase measurements are contaminated and show the same value of phase index regardless of the level of amplitude scintillation.

A possible approach to overcome the TCXO error and here applied is proposed in [5] and [42]. The latter is a method based on the selection of a non-scintillating link (assumed known) as reference. Phase measurements from the reference signal are subtracted from the phase measurements of the remaining satellites in order to remove the oscillator noise, that is the same for all the considered links. The carrier phase of the satellite of interest can be expressed as:

$$\tilde{\varphi_k} = \varphi_k - \varphi_{ref} \tag{4.2}$$

where φ_k is the carrier phase from the k^{th} target satellite and can be modeled

as:

$$\varphi_k = \varphi_{k-geom} + \varphi_{clock} + \varphi_{k-scint} + n_n \tag{4.3}$$

with

- φ_{k-geom}: as the phase contribution due to the satellite geometry.
- φ_{clock}: as the phase contribution due to the clock.
- $\varphi_{k-scint}$: as the phase contribution due to ionospheric scintillation.
- n_n: as other noise sources (e.g. thermal noise and satellite oscillator noise).

φ_{ref} is the phase of the reference satellite, modeled as:

$$\varphi_{ref} = \varphi_{ref-geom} + \varphi_{clock} + n_{ref} \tag{4.4}$$

where the phase contributes are the same as in (4.3) but related to the reference satellite. The difference of these phase carriers is taken, creating a combined carrier phase measurement given by:

$$\tilde{\varphi_k} = (\varphi_{k-geom} - \varphi_{ref-geom}) + \varphi_{k-scint} + (n_n - n_{ref}) \tag{4.5}$$

This new phase measurement now contains the combination of the geometric effect for the two satellites, the combination of the noise on the two satellites, and the phase fluctuations due to scintillation on the *k-th* satellite of interest. The differential phase contribution due to the geometric effect can be removed by modeling it as a third order polynomial, effectively isolating scintillation for satellite k from local clock and satellite motion effects.

To demonstrate the latter approach, the experimental set-up shown in Figure 4.9 was deployed. The signal from the antenna is split into two branches: The upper branch samples the data with a high quality and stable oscillator and will be used as the reference scenario. The lower branch, on the other hand, samples the data with a low quality oscillator that introduces phase

noise into the measurements and will be used as the test scenario for the differential phase approach. Analysis is performed by comparing the outputs of the two branches.

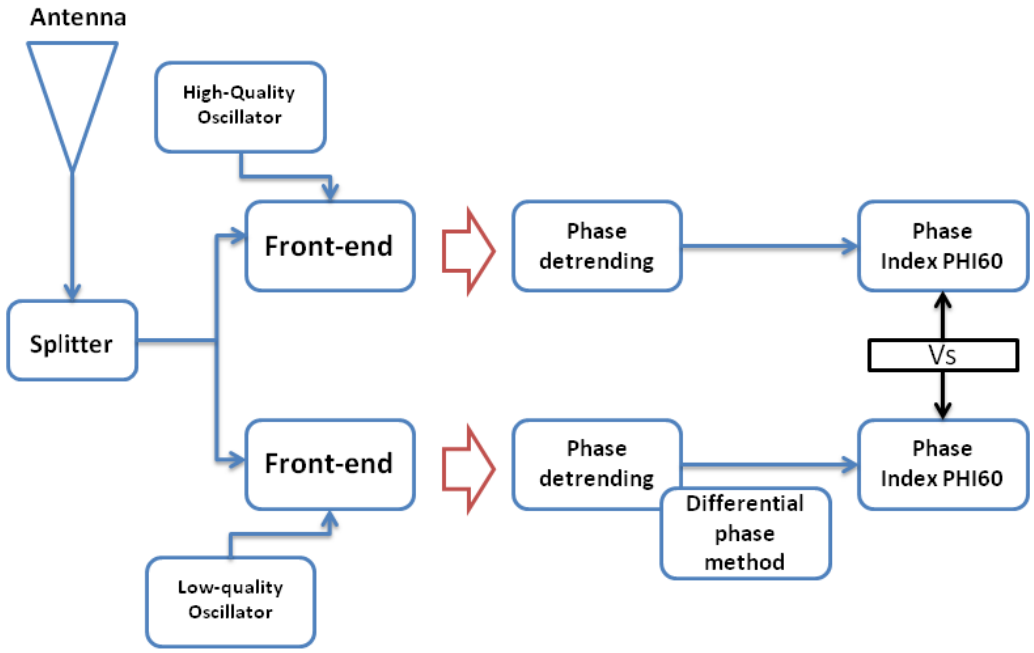

Figure 4.9: Differential phase experiment set-up

Figure 4.10 presents the amplitude scintillation levels of the two chosen satellites for the demonstration. *PRN19*, a non scintillating satellite link as evidenced by a value of $S4$ at the noise level, was chosen as the reference satellite. Consequently, a low σ_φ can be assumed for such satellite given that for equatorial scintillation as the one here considered, amplitude and phase scintillation occurrence are highly correlated [8]. *PRN23* is the satellite chosen as the target. It is expected to have a significant amount of phase variations due to scintillations as consequence of its high $S4$ value.

From the lower branch of the set-up, detrended phase measurements for both satellites together with their phase difference can be seen in Figure 4.11. As observed, the level of the phase fluctuations is nearly identical for both satellites due to the phase noise introduced by the low-quality oscillator. However, after applying the differential method the common phase error is eliminated,

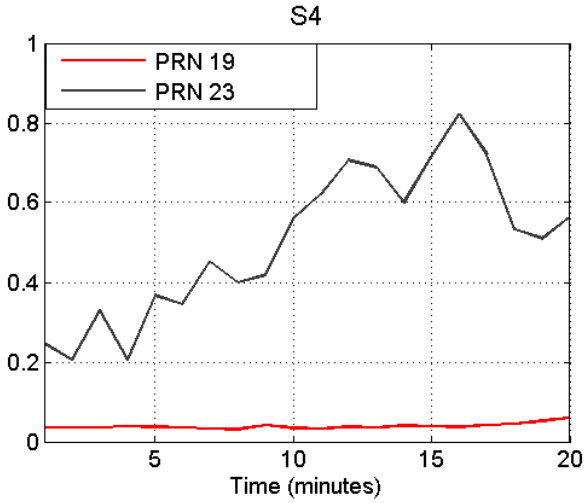

Figure 4.10: Amplitude scintillation indices for reference and target satellites

putting in evidence how dominant the common phase noise was over what could be expected as phase variations due to scintillations.

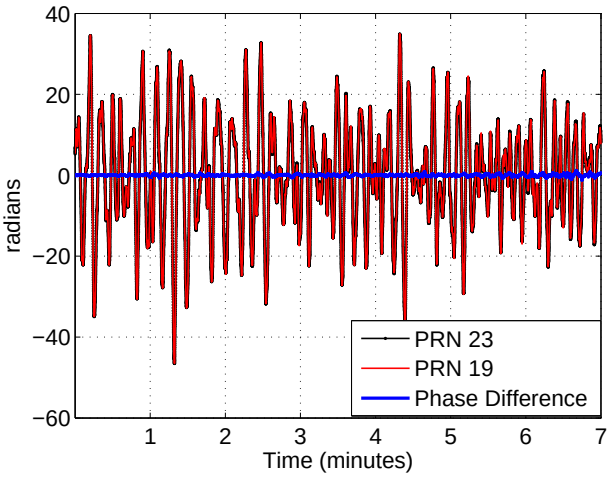

Figure 4.11: Corrupted phase vs Differenced phase

On the other hand, Figure 4.12 compares the differenced phase with the uncorrupted detrended phase measurement of the target satellite, the latter estimated this time with the high quality oscillator from the upper branch of the experiment set-up. It is noticeable that the phase differenced curve is in good agreement with the reference phase scintillation profile after the removal of the common phase error. As expected, slight differences still remain due to

the combined noise term from the two satellites, as it was presented in (4.5).

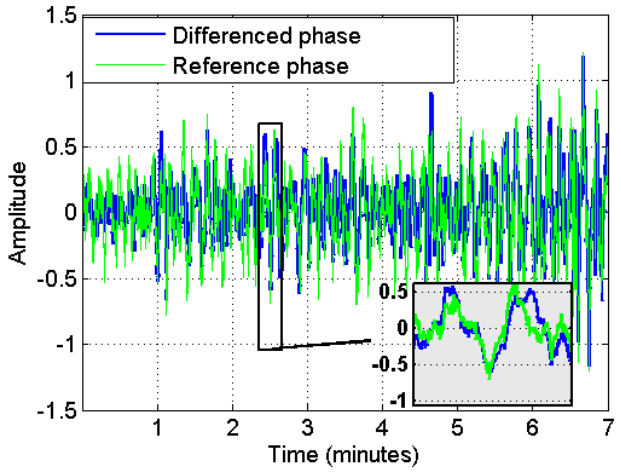

Figure 4.12: Differenced detrended phase vs Reference detrended profile

To put in perspective how much power the phase disturbances can have over the scintillations, Figure 4.13 compares the spectral characteristics of the contaminated phase samples with those of the differentiated and true scintillation phase profiles for the target satellite.

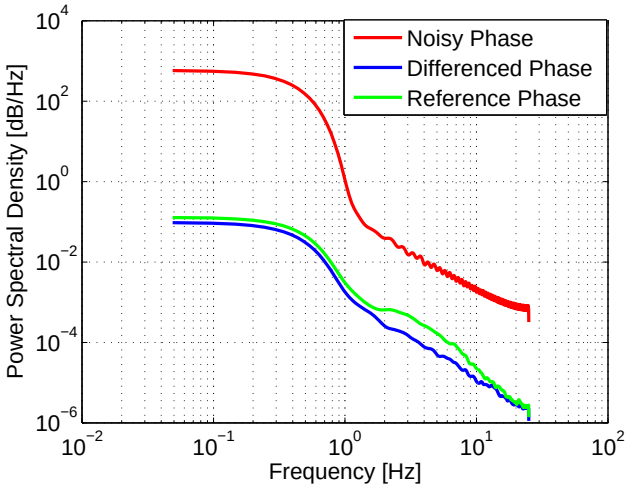

Figure 4.13: Power Spectral Densities of detrended phases samples

Finally, Figure 4.14 compares the phase indices computed from both branches of the set-up. As it can be seen, the differential method can successfully

eliminate common phase distortions affecting the satellite measurements in the receiver and provide measurements in good agreement with the output of set-ups using higher quality components.

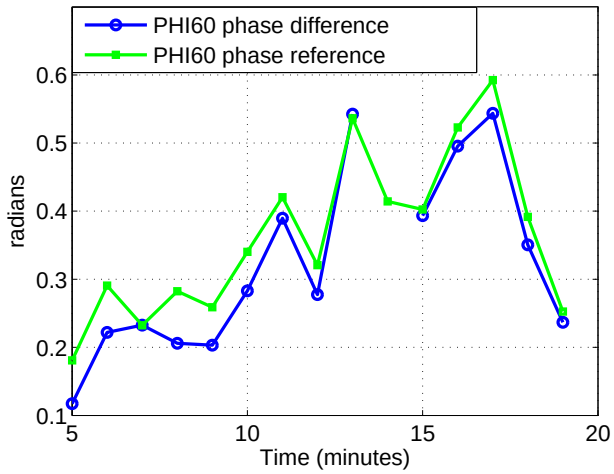

Figure 4.14: PHI60 comparison: Differential method vs. High quality oscillator

4.4 Ionospheric Scintillations over Vietnam: Campaign overview

Having solved the initial signal processing/hardware issues presented in Sections 4.2 and 4.3, a GNSS front end to collect unprocessed data samples was installed in Hanoi, Vietnam for ionospheric scintillation data collection. The campaign lasted for several months, from February to September 2013, in which interesting scintillation events where recorded. The set up took place at the NAVIS Centre, Hanoi University of Science and Technology in collaboration with the European Joint Research Center based in Ispra, Italy and the NavSaS group of Politecnico di Torino/Istituto Superiore Mario Boella based in Turin, Italy. The installation consisted of antenna, front-end, pc and hard drives. Figure 4.15 presents a simplified diagram of the equipment installation at Hanoi.

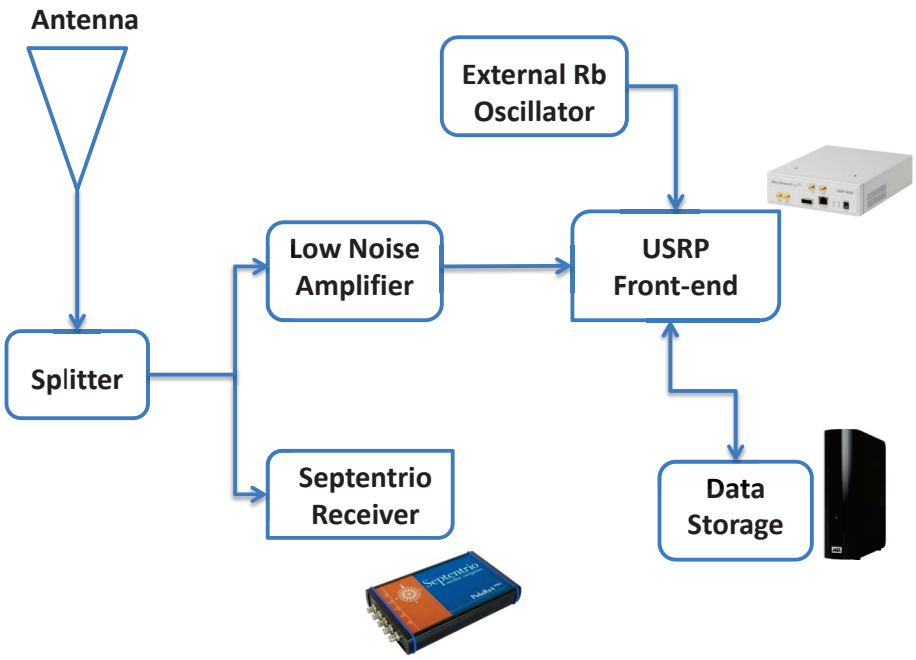

Figure 4.15: Installation Set-Up Hanoi

The front-end setup is based on:

- A general purpose Universal Software Radio Peripheral (*USRP*). *USRP* is a low-IF architecture radio designed to allow general purpose computers or digital signal processors (*DSP*) to function as high bandwidth communication devices. With a maximum sampling frequency of $50MHz$ and operating frequencies ranging from DC to $5.9GHz$, it is capable of capturing all L band GNSS signals [44].

- A high quality external Rubidium Oscillator, coupled to the *USRP* to ensure that the phase noise remains at its lowest when performing phase scintillation measurements.

- A Septentrio PolaRx4 receiver. This receiver was set in parallel to the front-end data collections, sharing the same antenna input of the USRP. It was used to continuously log regular observables such as C/N_0, azimuth and elevation of available satellites from both GPS and Galileo.

Data were collected from February to September 2013 on a 20 minutes basis each day after sunset local time for a few hours. This time window was deemed suitable since the experiment was carried out in the equatorial area. Through a replay process at JRC headquarters of the *USRP* logged data, scintillation indices are obtained from a Septentrio PolaRxS [45] for comparison purposes. Table 4.1 summarizes the configuration of the equipment installed.

Table 4.1: Hanoi Data Collection Set-Up

Parameter	**Value**
Antenna	AT1675-120W SEPCHOKE-MC
Geographical Coordinates	$21°2'0''N/105°51'0''E$
Front-end	Ettus Research USRP Model N200
External Oscillator	10MHz Rubidium reference
Frequency band	GPS L1 / Galileo E1
Signal	GPS L1 C/A - Galileo E1
Intermediate Frequency IF	0
Sample type	Short Complex
Sampling Frequency F_S	5MHZ
Front-end Bandwidth	5MHz

A fully software receiver as presented in [41] and updated to process scintillated GPS and Galileo signals was used to post-process the data coming from the *USRP* and calculate the scintillation indices. By following the procedure presented in Section 3.4, it is possible to estimate the amount of amplitude and phase scintillation affecting the signal. Following Sections present a few cases that highlight scintillation activity in the region and further tests that were performed with the data samples.

4.4.1 Scintillation Monitoring with GPS

Figure 4.16 shows the tracking processing outputs of *GPS PRN23* acquired at 1440UTC during the 14 of March 2013. For the software receiver, the tracking architecture consisted of a third order PLL with bandwidth $B_L = 12Hz$ and varying integration time T_{int} of 1,10,and 20 milliseconds. The top plot shows

the correlation outputs for the prompt, early and late correlators, the bottom plot shows the estimated C/N_0 . As seen from the top plot, the so called focusing-defocusing effect of scintillation in the signal amplitude causes the power in the prompt correlator to fluctuate. The effect is also noticeable in the estimated C/N_0.

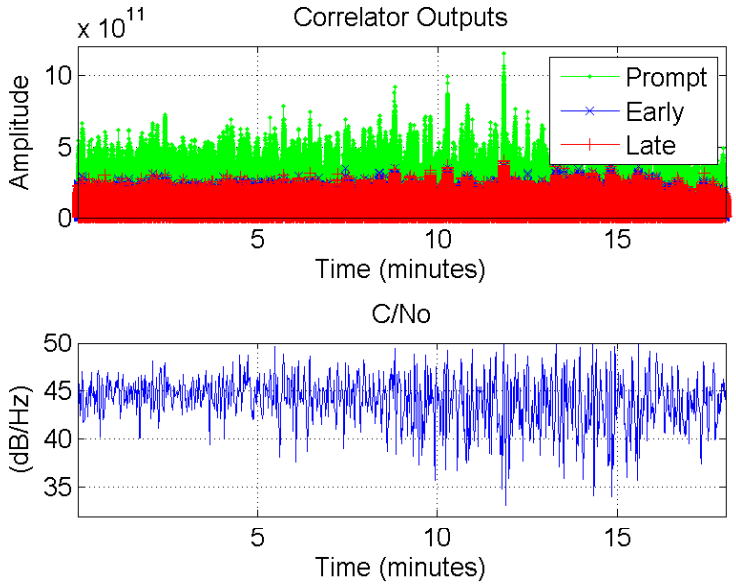

Figure 4.16: Processing scintillating signals with the software receiver.

Figure 4.17 shows a minute of the detrended SI from correlator samples obtained at 1 and 10ms, compared with the signal power SP from samples at 20ms. As analysed in the previous chapter, scale factors are eliminated during the detrending normalization and no significant difference between these estimations is observed, thus the $S4$ in Figure 4.18 is the same for all three cases. There is a good agreement between the software receiver calculated indices with the output from the Septentrio PolaRxS, the latter used as a benchmark for the results. It is also noticeable that the satellite was quite affected by scintillation, going from medium to very strong amplitude scintillation levels in the 18 minutes of processed data. To recall, $S4$ greater than 0.6 is considered strong in the literature.

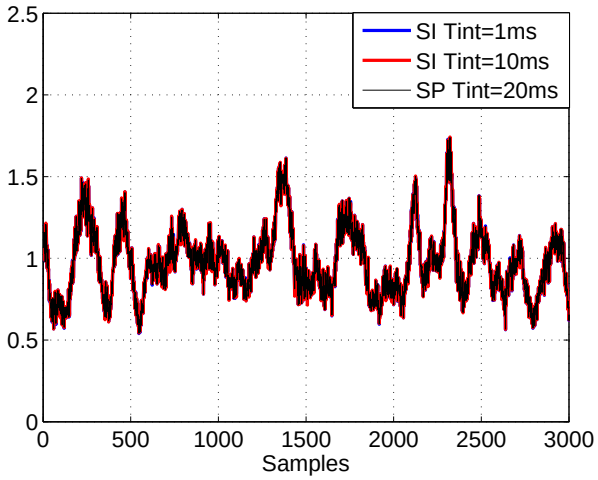

Figure 4.17: Detrended amplitudes for different PLL integration times.

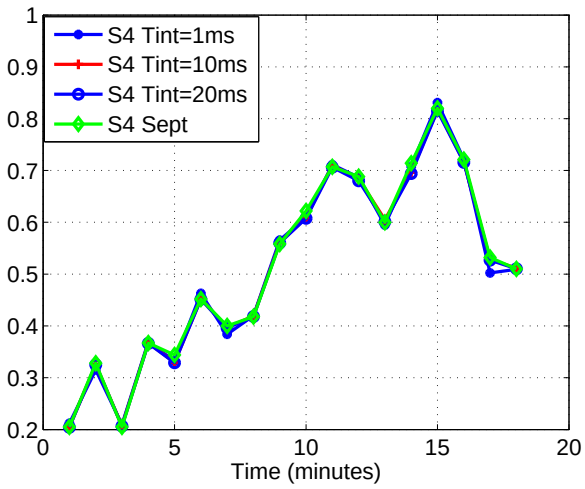

Figure 4.18: $S4$ for different PLL integration times.

Likewise, Figure 4.19 corresponds to the detrended carrier phases. Phase measurements are obtained directly at 50Hz rate regardless of the integration time. No major difference is observed between the detrended phases at different integration time, provided the receiver was able to correctly track phase changes in all of the three tracking configurations. Figure 4.20 gives the corresponding phase scintillation indices from the detrended signals and the Septentrio reference. There is no value shown for the index during the first four minutes of data processing due to the transient time of the detrending filter of the phase measurements. Severe scintillation activity may lead

Phi60 in particular to not being calculated at all if the satellite losses lock continuously due to this necessary transient time.

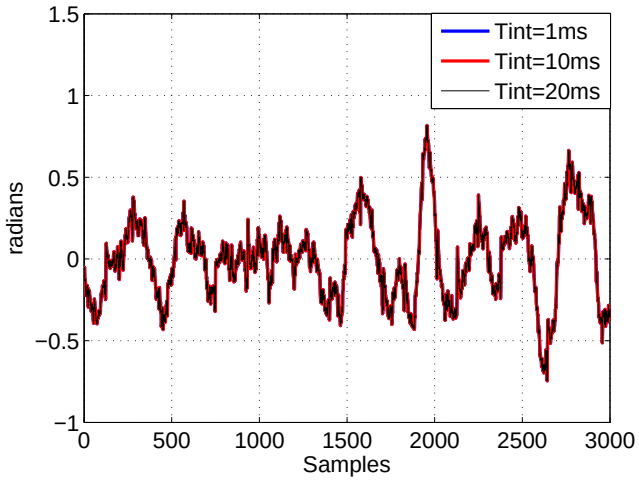

Figure 4.19: Detrended phases for different PLL integration times.

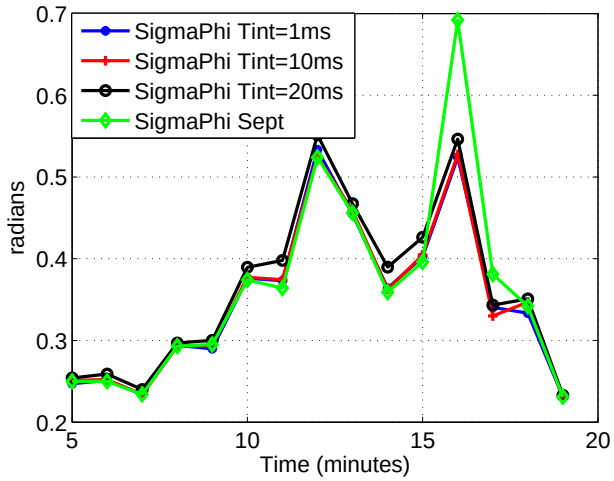

Figure 4.20: *Phi*60 for different PLL integration times.

4.4.2 Scintillation Monitoring with Galileo

The same tests were performed on a Galileo satellite. Figures 4.21 and 4.22 show the estimated scintillation indices for Galileo *PRN12* acquired at 1440UTC

during the 10th of April 2013. A good agreement between the software receiver and the PolaRxS computation is also observed in this case. The tracking architecture consisted once more of a third order PLL with bandwidth $B_L = 12Hz$ and varying integration time T_{int} of 4 and 20 milliseconds. As in the case with GPS, no significant differences in using the signal intensity estimator or a power estimator for the $S4$ computation were found.

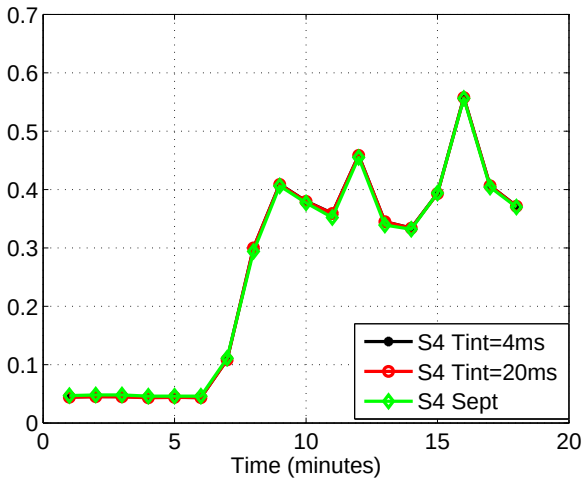

Figure 4.21: Scintillation indices from GALILEO signals. $S4$.

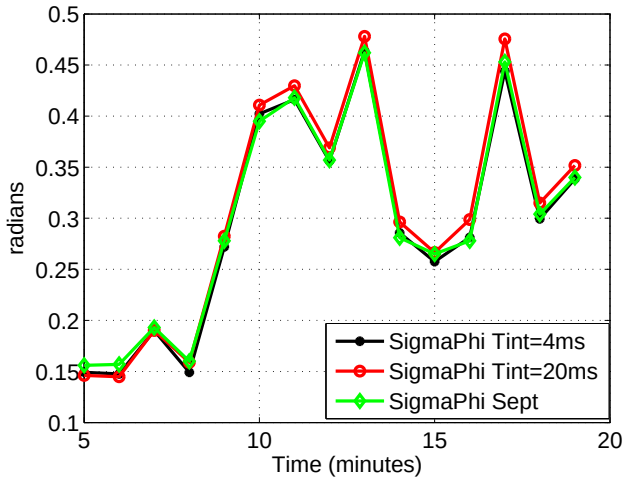

Figure 4.22: Scintillation indices from GALILEO signals. $Phi60$.

4.4.3 Strong Scintillation Activity over Hanoi

The skyplot for satellites acquired and tracked over Hanoi during the 10th of April 2013 can be seen in Figure 4.23. Four datasets of 20 minutes were acquired and stored between 1320UTC and 1600UTC and processed later using the software receiver. Galileo *PRN11* and *PRN12* were present during this time, making a good complement of the coverage attained by GPS satellites and providing two extra ionosphere probe signals. *PRN19* was also present, albeit with low elevation and was not suitable for scintillation analysis. The three Galileo satellites can be identified in the figure by red tracks. This particular day presented strong ionospheric activity, where almost all the

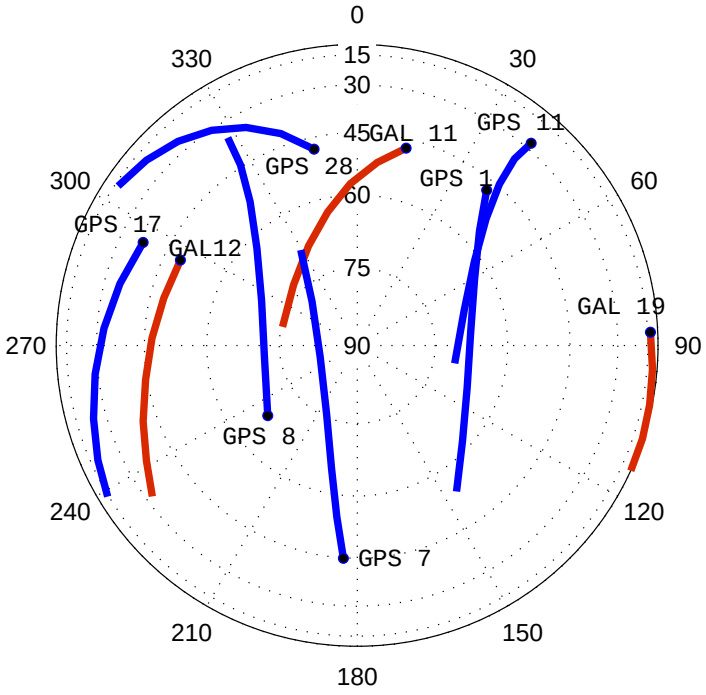

Figure 4.23: Skyplot over Hanoi on 10/04/2013.

satellites shown experienced scintillations. Figures 4.24 and 4.25 present the $S4$ and $Phi60$ index for all the satellites. $S4$ levels around 1 can be observed in satellites from both systems. Some satellites also experienced strong phase

scintillation, with phase deviations due to scintillation reaching up to and above 1 radian.

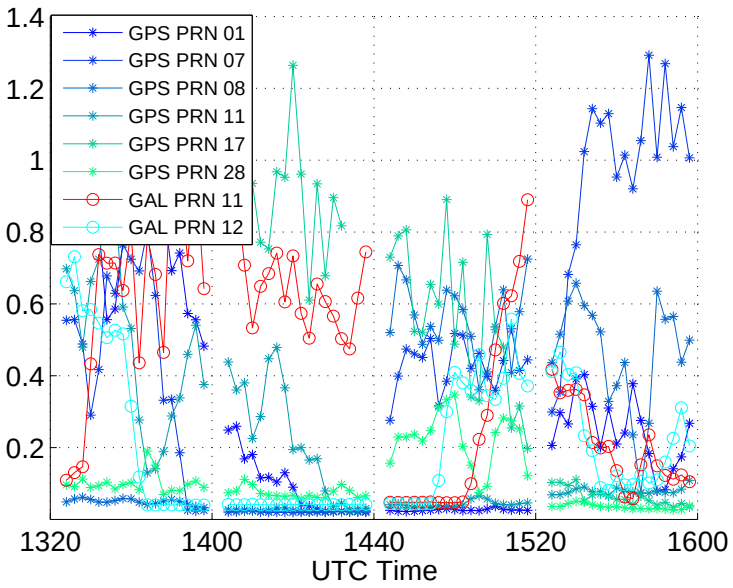

Figure 4.24: Recorded scintillation activity over Hanoi on 10/04/2013. $S4$.

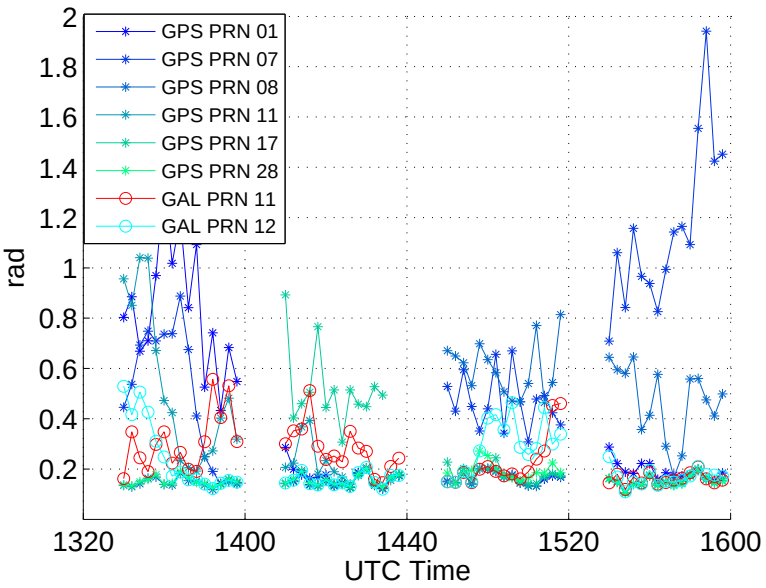

Figure 4.25: Recorded scintillation activity over Hanoi on 10/04/2013. $Phi60$.

4.5 Summary

This chapter reviewed key aspects to take into account when monitoring ionospheric scintillations with GNSS, as it is necessary to take into account hardware and software aspects of the receiver in order to correctly estimate the behaviour of scintillations. It was seen that detrending operations can enhance the output of the S4 index if the delay of the filter is not accounted for. The mean value detrending appears as a viable alternative since it is faster and easier to implement, but it has shown to enhance measurements of amplitude scintillation in particular cases.

A summary of the components and functions of the receiver front end was given, as elements that compose it, the oscillator in particular, can have an influence over phase scintillation measurements given that its noise can obscure the phase variations due to scintillations. Though the problem is avoided by the use of high quality oscillators such as the OCXO or Rubidium standards, it is a costly solution that might not not always be convenient. However, through the differential phase measurement method this obstacle can be overcome, making possible lower cost implementations of scintillation monitoring.

Chapter 5

Radio Frequency Interference in GNSS

Telecommunication systems transmitting at carrier frequencies close to GNSS bands may interfere with satellite signals. Radio Frequency (RF) Interference is an unpredictable and potentially devastating error for many GNSS applications. Given the extremely low received power of the GNSS signals, typically -160 dBW for all GNSS system, unintentional interference from other telecommunication systems is not an unlikely threat.

The presence of interfering power can be due to several reasons, the main ones being harmonics and intermodulation products. The former are integer multiples of the carrier frequency caused by non-linearities, as for example, saturation of amplifiers. The latter occurs when two or more signals at different frequencies are mixed by passing through some non-linearities.

This has lead to extensive research to assess and improve the reliability of GNSS receivers against interference effects as more of these systems will start working in frequency bands close to GNSS in the near future. Consequently, it is also of interest to understand the effects that interference may have on the estimation of scintillation indices and in particular those that can fall within the GNSS L1/E1 band, the most widely used to monitor scintillations. When

subject to interference, GNSS receivers experience an increased variance in the signal amplitude and phase that could potentially impair the effectiveness of scintillation monitoring.

This chapter will review the classification of interference signals in the literature, which systems could potentially generate such signals and in particular the effects interference can induce in a GNSS receiver. A few of the most common interferences nowadays will be analysed in detail as well.

5.1 Classification of Interference

Interference from other systems can be classified taking into account different aspects of the signals [46][47].

1. **Source**: According to the source, they can be either intentional (jamming) or unintentional. The first are common for military scenarios while the second are due to unintentional leakages of power out of the interference emitter allocated bandwidth.

2. **Bandwidth**: Depending on the bandwidth of the interfering signal B_{int} with respect to the bandwidth of the GNSS signals B_{GNSS}, they may be categorized as:

    - *Narrow-band Interference (NBI)* when the spectral occupation is smaller with respect to the GNSS signal bandwidth ($B_{int} << B_{GNSS}$)
    - *Wide-band Interference (WBI)* when the spectral occupation is comparable with respect to the GNSS signal bandwidth ($B_{int} \approx B_{GNSS}$)
    - *Continuous Wave Interference (CWI)* which represents the ultimate limit in NBI and appears as a single tone in the frequency domain ($B_{int} \to 0$)

3. **Time domain behaviour**: According to its characteristics in the time domain, an interfering signal may be either non-pulsed (continuous) or pulsed. Pulsed interfering signals are characterized by on-off status of short duration in the order of μs, which alternate in the time domain. Such kind of interference signal is typical of the aviation scenarios, where several Aeronautical Radio-navigation Services (ARNS) broadcast strong pulsed signals in a bandwidth that is shared with some of the satellite navigation systems.

4. **Frequency spectrum**: Depending on where the interference appears in the frequency domain with respect to the radiofrequency spectrum occupied by GNSS signals, they may be categorized as:

   - *Out of band*: When the carrier frequency of the interference signal f_{int} is located near to the targeted GNSS frequency band f_{GNSS}. In this case $f_{int} < f_{GNSS} - B_{GNSS}/2$ or $f_{int} > f_{GNSS} + B_{GNSS}/2$
   - *In band*: When the carrier frequency of the interference signal falls within the GNSS frequency band. In this case $f_{GNSS} - B_{GNSS}/2 < f_{int} < f_{GNSS} + B_{GNSS}/2$

5.2 Interference Effect on GNSS Receiver Outputs

Strong interference can cause GNSS receivers to lose lock on satellite signals and stop working. Nevertheless, in many cases the presence of interference power is only strong enough to decrease the receiver performance but not to blind it completely. Such intermediate power values turn out to be the most dangerous since sometimes they cannot be detected. They lead to an increased error in pseudoranges and phase measurements, thus decreasing the accuracy of the position solution. The impact of interference can be summarized depending on the stage of the receiver [47][1]:

Impact on the front-end: The Adjustable Gain Control(AGC) adjusts the power of the incoming signal to optimize the signal dynamics for the Analog to Digital Coverter (ADC) stage in order to minimize quantization losses. When interference is present the AGC will squeeze the incoming signal in order to match the maximum dynamics of the ADC, thus causing a reduction of the amplitude of the useful signal, which may be lost.

Impact on the acquisition stage: Effects on the search space may depend on the type of interference. Overall, an increase of the noise floor may be observed.

Impact on the tracking stage: The impact of the interferer on the tracking stage has a direct consequence on the quality of the measured pseudorange. Presence of harmful interfering signals not only produce an increase of the variance of Time of Arrival estimate provided by the discriminator but also cause a modification of the shape of the S-Curve of the code discriminator, thus creating in some cases a bias in the measurements. The noise on the phase measurements of the GNSS receiver is increased as well, with an overall increase in the variance of the carrier phase discriminator output.

Impact on the estimated signal to noise ratio: The C/N_0 provided by the receiver is by definition the ratio between the received signal power and the power spectral density due to thermal noise at the input of the receiver. The presence of the interference should not change the value, since the thermal noise is not increasing. However, since the C/N_0 is estimated on the basis of the correlator outputs at the tracking stage, it is affected by the presence of the additional (non-thermal) noise generated by the interference. In some cases, the variation of C/N_0 may be used as an observable for interference detection.

5.3 Potential Interference sources

Interference mainly comes from spurious emissions of out-of-band system which generate harmonics colliding with the GNSS bandwidths. Some of the main unintentional interference sources in GNSS bands can be seen in Figure 5.1 and are detailed next.

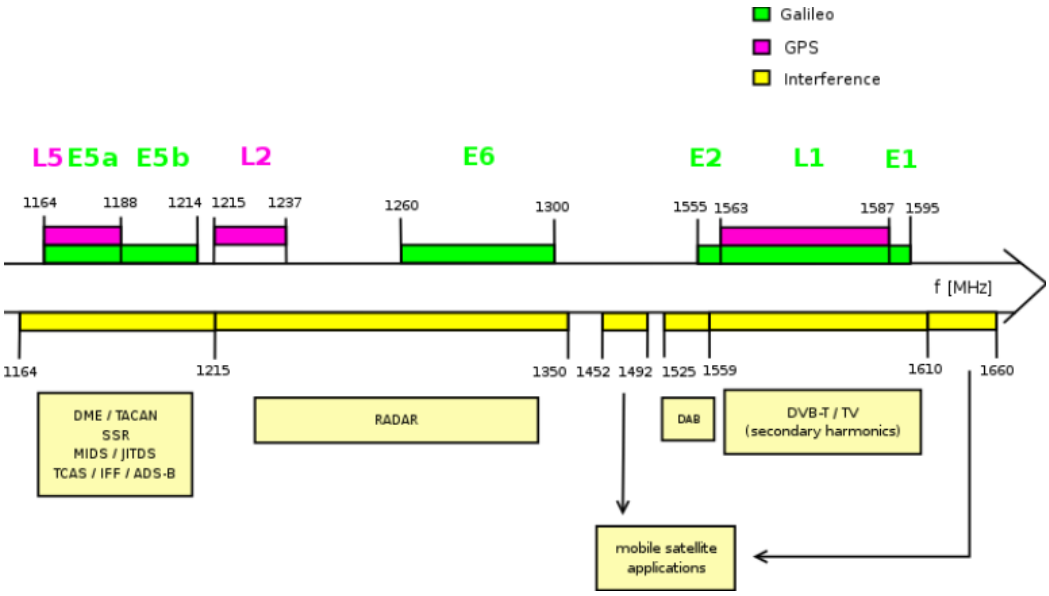

Figure 5.1: Potential interference sources in GNSS bands.

- *Analog and Digital TV Channels*: In the broadcast analog TV signal, Very High Frequency (VHF) and Ultra High Frequency (UHF) bands are used. Harmonics of such bands generated by TV ground station transmitters can generate potentially dangerous interference for GNSS receivers. They can be both wide and narrow band interference: the video carriers are considered as medium/wide band signals whereas the sound carriers are considered as CWI. In [48], an interference case is reported from TV signals where harmonic distortions from a low noise amplifier (LNA) resulted in average 5dB decreases in C/N_0. Malfunction of power amplifiers may also cause digital television signals (DVB-T) to generate harmonics that fall into GNSS bands [9].

- *VHFCOM*: VHF systems, such as the Air Traffic Control (ATC) communications can generate armonics that fall into GPS bands. These are considered as NBI with a bandwidth of about 25KHz.

- *FM Signals*: The harmonics generated by FM sources are considered as WBI with respect to GNSS signals. They are allocated in the L1/E1 bands.

- *VOR and ILS*: The VHF Omni-directional Range (VOR) is a radio navigation systems for aircrafts. The Instrument Landing System (ILS) consists of two radio transmitters providing lateral and vertical guidance to aircraft for approaching landing.Their harmonics, the 14th from VOR and 2nd from ILS corresponding to 111.9 and 111.95 MHz, enter on the L1/E1 band. They are considered CWI signals.

AS stated before, some interference sources broadcast signals whose carrier frequency is allocated in the GNSS bands. As of now, the frequency bands of new signals such as the GPS L5 and Galileo E5 is shared with positioning Aero Radio Navigation Systems (ARNS), the Distance Measuring Equipment (DME) and military Tactical Air Navigation (TACAN), all of which can have an impact on GNSS receiver performance [49].

Unlike the shared L1/E1 frequency band, the GPS L5/L2 and Galileo E5/E6 bands have not been allocated exclusively for navigation systems, consequently increasing the probabilities of interference. In-band interference may also be generated by *jammers*, devices transmitting signals with the intention to jam (or block) GNSS signals.

5.4 Interference signal description

Next are described in more detail some of the most common interference signals mentioned before.

5.4.1 Continuous Wave Interference

CWI can severely impact GNSS receiver either on the acquisition or tracking stages. This is due to the interference power being dispersed on the whole search space by the correlation with the local code, compromising the acquisition accuracy and impacting on the other functional blocks. CWI can be generated from harmonics of various sources like FM/TV transmitters and mobile phone networks. Such interference signal can be represented by a pure sinusoid:

$$i_{cw}(t) = A_{CW} sin(2\pi f_{CW} t + \theta) \tag{5.1}$$

where A_{CW}, f_{CW}, and θ are respectively, the amplitude, frequency and phase of the CW.

The impact of CWI strongly depends on the value of the central frequency of the interference within the GNSS frequency band, due to the particular spectral characteristics of the code. The spectrum of a GNSS signal like GPS C/A and Galileo E1 have spectral components spaced at multiples of the inverse of the code period, e.g. 1 kHz for GPS C/A code.

Such spectral components are more sensitive to interference and the CWI can generate false lock in the correlators when aligned with one of them [1] [50]. As it was seen in Figure 2.4, they have approximately but not exactly, a $\sin(x/x)^2$ power spectral envelope .

The power level of the individual spectral components depends upon the individual code and varies from a worst case of from -18.3 to $-21.5dB$ to more typical values on the order of $-30dB$ below the code power for small frequency offsets. The actual line component at zero offset is almost completely suppressed ($-60.2dB$) because the balanced Gold codes have an average of only $-1/1023$. Thus, if a narrow bandwidth interfering signal such as the CWI in (5.1) is received, and its frequency matches that of one of the C/A reference signal spectral components, the interference signal generates a comb of such components in the correlator output.

One of these components, corresponding to the frequency offset of the interference relative to the receiver reference local oscillator, can fall directly on the correlated output signal. Thus, the worst case interference signal would be attenuated relative to the total code power by only 18.3 to 21.5 dB depending on the satellite C/A code. However, the more typical numbers are in the vicinity of $-30dB$ as the frequency offset becomes greater than $600KHz$. Even if one of the tones from a CW interference should fall directly in the receiver tracking band, it is likely that only one satellite will be affected, because all satellites have somewhat different Doppler profiles [10].

An example of a continuous wave interference in GNSS is now presented. Details of the scenario are reported in Table 5.1. In the example the signal has a duration of 26 minutes and CWI is injected for half of that time, from minutes 8 to 21.

Table 5.1: CWI scenario set-up.

Parameter	**Value**
Signal	GPS L1 C/A
Intermediate Frequency IF	3MHz
Sampling Frequency F_S	12MHZ
Front-end Bandwidth	5MHz
Interference Type	CWI
Interference Power	-130dB
Interf. Freq. Offset w.r.t. L1 carrier	25KHz

Figures 5.2 shows the spectrum of the GNSS signal at IF and the estimated C/N_0. Figure 5.3 shows outputs from the tracking such as the phase error and power in the correlators of a GPS signal affected by CWI. As seen in Figure 5.2(a), CWI can be seen as a single tone above the GNSS signal level in the frequency domain.

When the interference is present the effect is noticeable in the correlator outputs with the power of the signal fluctuating as depicted in Figure 5.2(b) and consequently affecting the estimation of the C/N_0 as evidenced in Figure 5.3(a). Moreover, Figure 5.3(b) shows there is a particular effect on the

phase error as the CWI moves closer to one of the code spectral lines around minute 17, with a huge increase in the error that might affect greatly phase measurements.

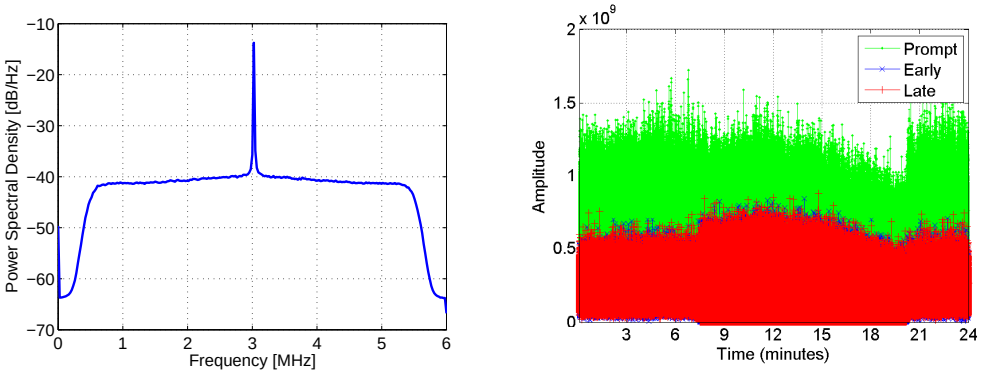

(a) Signal Spectrum (b) Correlator Outputs

Figure 5.2: GPS Signal under CWI (1).

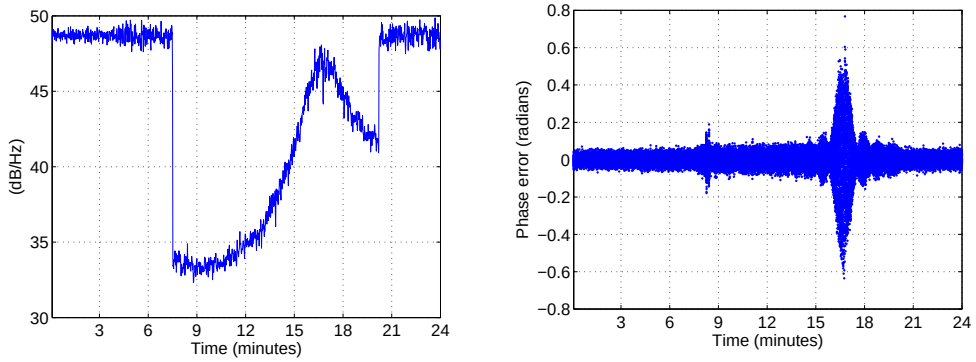

(a) C/N_0 (b) Phase Error

Figure 5.3: GPS Signal under CWI (2).

5.4.2 Wideband Interference

Interferences with bandwidth comparable to that of the GNSS signals are considered WBI. As example, the harmonics generated by FM sources are considered as WBI with respect to GNSS signals allocated in the L1/E1 bands. It can be represented as an Additive White Gaussian Noise signal [51].

Similarly to the CWI case, a simulated scenario is presented next to showcase some of the characteristics of the WBI. Details of an example scenario are summarized in Table 5.2.

Table 5.2: WBI scenario set-up.

Parameter	Value
Signal	GPS L1 C/A
Intermediate Frequency IF	3MHz
Sampling Frequency F_S	12MHZ
Front-end Bandwidth	5MHz
Interference Type	WBI
Interference Power	-130dB
Interf. Freq. Offset w.r.t. L1 carrier	25KHz
Interference Bandwidth	1MHz

The spectrum of the signal affected by the WBI is observed in Figure 5.4. The effects of the WBI differs from the one presented earlier in the CWI case. When WBI is present it can be taken as a steady increase in the noise floor independently of the code spectral lines. As explained before, the AGC in its function to accommodate to the increased signal dynamics squeezes down the useful GNSS signal. This explains the constant drop in power noticed in Figure 5.4(b) in the correlators output. The estimated C/N_0 is affected accordingly, as seen in Figure 5.5. A steady increase in the phase errors due to the presence of the WBI is also observed in Figure 5.5(b).

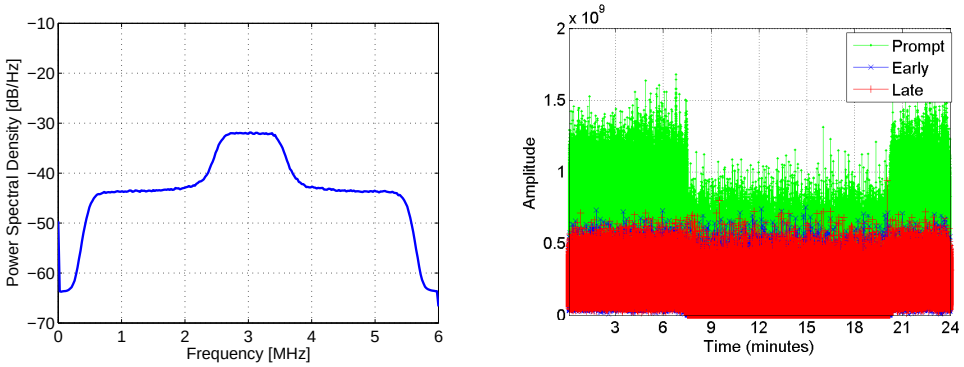

(a) Signal Spectrum (b) Correlator Outputs

Figure 5.4: GPS Signal under WBI (1).

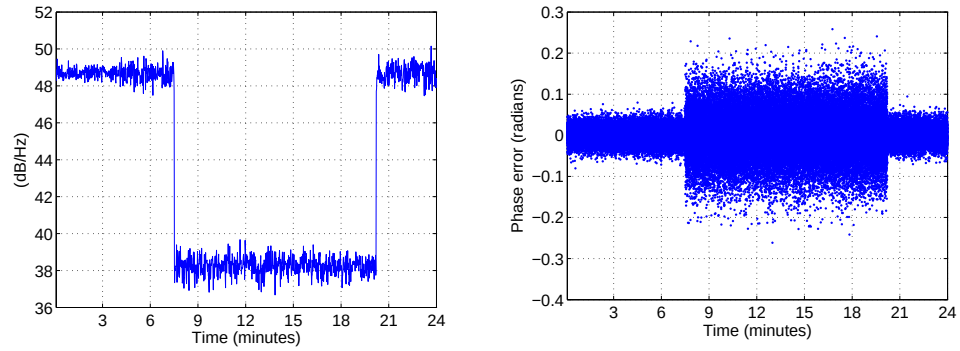

(a) C/N_0 (b) Phase Error

Figure 5.5: GPS Signal under WBI (2).

5.4.3 Chirp Interference

Chirp signals are characterized by a linear variation in time of their instantaneous frequency. This kind of interfering signal appear as WBI in the frequency domain and is typically generated by the *jammers*. Such devices are capable of transmitting strong power chirp signals sweeping several MHz in few μs, obscuring the correct reception of GNSS signals. These devices are able to transmit over different GNSS frequency bands [52]. A simulated example scenario is described in Table 5.3.

Table 5.3: Jamming scenario set-up.

Parameter	**Value**
Signal	GPS L1 C/A
Intermediate Frequency IF	3MHz
Sampling Frequency F_S	12MHZ
Front-end Bandwidth	5MHz
Interference Type	Chirp Signal
Interference Power	-130dB
Sweep Period	$9\mu s$
Sweep Range(L1+/-)	11.6MHz / 7.4MHz

Effects can be observed in Figures 5.6 and 5.7. In this case, effects are similar to the WBI presented before, but less pronounced due to the fact that the same interference power of both cases, $-130dB$, is in the present example spread in a bigger bandwidth than what the front-end can actually let in.

For this reason the actual power of the jamming signal into the receiver is lower. Consequently, the effects in C/N_0 and phase error are less pronounced.

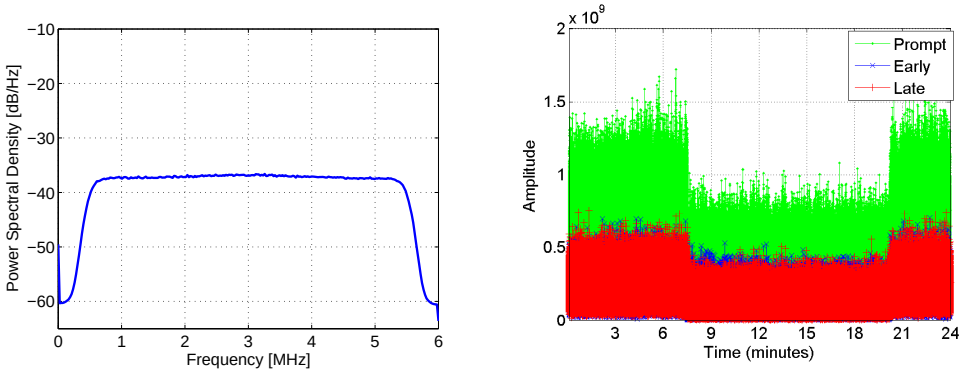

(a) Signal Spectrum (b) Correlator Outputs

Figure 5.6: GPS signal under jamming interference (1).

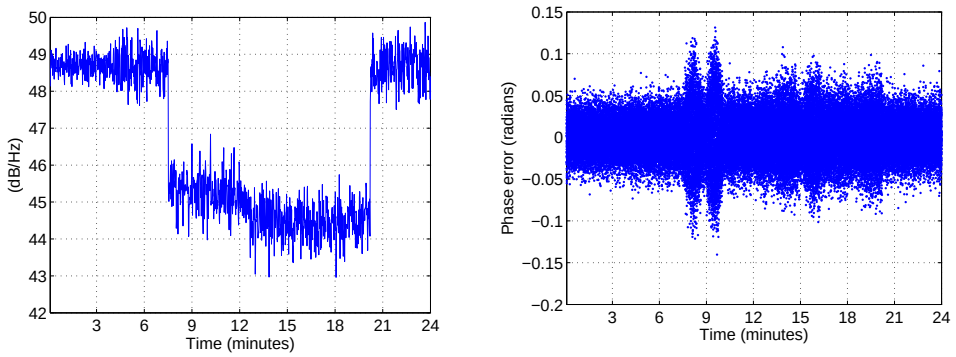

(a) C/N_0 (b) Phase Error

Figure 5.7: GPS signal under jamming interference (2).

5.5 Summary

An introduction to interference in GNSS was presented in this chapter. Interference signals can be classified in general according to its emitter source type and/or its time and frequency domain behaviour. The impact on GNSS receiver stages varies according to the type of interference, affecting the performance from the acquisition stage up to the positioning estimation. Despite

all the harmful effects interference can induce in GNSS receivers and related services, it is to be considered that RFI is typically generated only in case of bad design of the communication systems or malfunctioning events. The most typical form of unintentional interference were presented, Continuous Wave and Wideband interference signals, along with the more special case of intentional interference or so called jamming.

Chapter 6

Interference Effect in GNSS-based Estimation of Ionospheric Scintillation Activity

The previous chapters reviewed the effects that both ionospheric scintillation and interference have separately on GNSS systems. We now introduce in this chapter the effect of interference in the context of scintillation monitoring. The chapter will take a look at how the scintillation indices output is affected by the presence of several interference signals based on their power, time and frequency characteristics.

Interference tests and analysis have been performed extensively to analyze its effects in GNSS architecture and positioning solutions, as in [51], [53] and [54], where the reader is referred for a comprehensive analysis. Our focus here is to observe the effects on the scintillation indices, something the authors consider is necessary as scintillation monitoring becomes a more important activity. As presented in Chapter 5, under interference a GNSS receiver may experience fluctuations in both power and phase measurements. These are indeed problems that may trigger a false detection of ionospheric activities when tracked by GNSS signals.

The fact that interference can potentially affect the estimation of scintillation activity is mentioned in the literature, as in [6] and [55]. However, a look into the effects of interference on scintillation monitoring is lacking and it is proposed here.

6.1 Scintillation - Interference Scenario

The scenario where a scintillating signal arrives to the GNSS antenna along with an interference signal is described in Figure 6.1. In this scenario of interest, the scintillating signal can be affected by one of several types of interference.

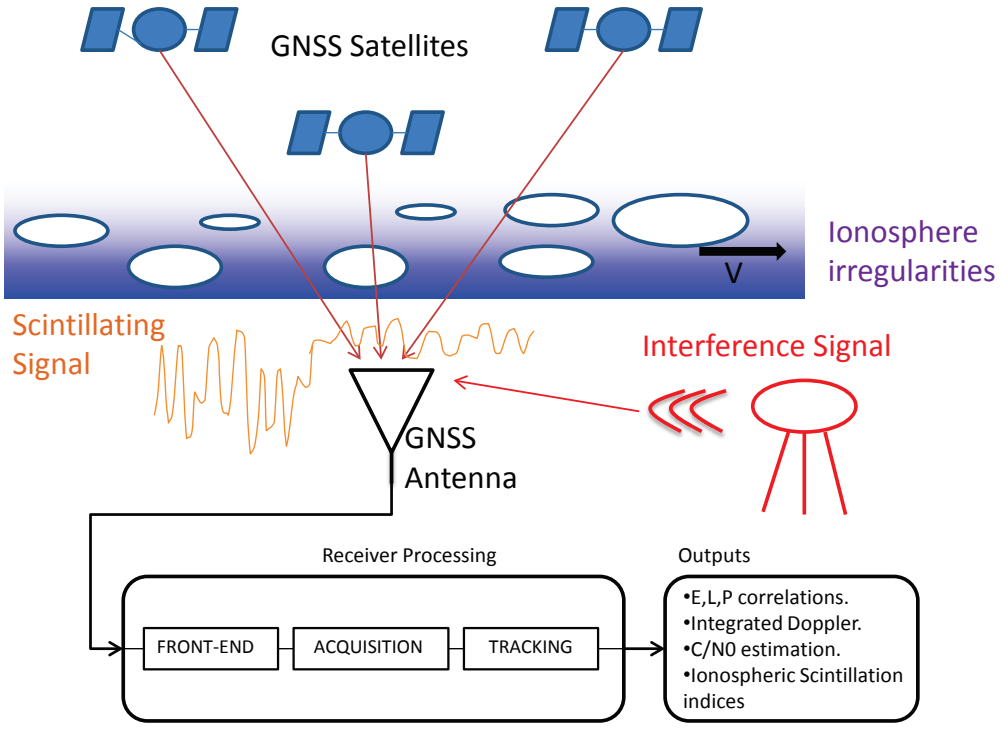

Figure 6.1: Illustration of a scenario where both scintillation and interference affect the GNSS signal.

For a single GPS satellite, in order to simplify the notation,the signal at the input of the antenna can be written as:

$$S_{sf} = S(t) + i(t) \tag{6.1}$$

where $S(t)$ is the GNSS scintillating signal as defined in Section 3.4, and $i(t)$ is an interference signal that can assume different forms depending on the system that generated it. To observe the effects of interference in the calculation of the $S4$ we will first introduce examples of reference scenarios in which only scintillations are affecting the $L1$ signal, to then proceed to regenerate/reprocess the same scintillating scenarios with the presence of an interference. As there are many possible signals that could interfere with GNSS, we will reduce our analysis to two of the most commonly found interferers: the continuous wave and wideband type interference signals, the latter in the form of wideband noise and chirp signals. An analysis on how the scintillation indices may be affected by interference is presented in following Sections by comparing with reference scenarios for both amplitude and phase scintillation .

6.1.1 Effects on S4

The fact that amplitude scintillation index S4 is calculated over the fluctuations of the signal intensity samples may make it vulnerable to additional error sources such as interference that also cause the signal power to fluctuate. Taking what was presented in Section 5.4 as foundation, Table 6.1 summarizes the scenario set-up to analyze the effects on the S4 when calculated from a GPS signal in the presence of interference. The three different interference signals described before, namely: Continuous wave, Wideband noise and Chirp Signal will be included in the analysis.

6.1.1.1 CWI Case

Before calculating S4, signal intensity (SI) must be calculated as first step. Figure 6.2 shows the SI samples versus the trend computed by using both the filter and mean value detrending methods. As observed in the figure, due to the effects of the interference there is a compression on the GPS signal

Table 6.1: Scintillation-Interference scenario set-up.

Parameter	**Value**
Signal	GPS L1 C/A
Simulation total time	24 minutes
Intermediate Frequency IF	3MHz
Sampling Frequency F_S	12MHZ
Front-end Bandwidth	5MHz
Nominal C/N0	49dBHz
Initial Doppler	2000 Hz
Doppler Rate	$1Hz/s$
Scintillation Level	Weak
Scintillation Time Interval	From minute 4 to end
Interference Type	CWI, WBI, Chirp
Interference Time Interval	From minute 8 to 21
Interference Power	-130dB
Interf. Freq. Offset w.r.t. L1 carrier	25KHz
PLL Bandwidth	5Hz
PLL Integration Time	1ms

amplitude that can be interpreted as a change of the gain in the receiver, effectively limiting the power of the signal that can be extracted. This is one of the effects interferences can cause to GNSS receivers, as analysed in Chapter 5. Such effect points to the AGC, which adjust its gain depending on the signal amplitude. In the presence of interference and its increased signal amplitude dynamics, this means that the gain of the useful part of the signal is not constant anymore and it is in fact reduced.

When extracting the trends of such signal the different detrending methods have different behaviors on how fast they can react to these sudden changes introduced by the AGC. The filter method can swiftly follow the drastic changes both when the interference starts and ends, as seen in Figure 6.2. On the other hand, the mean value detrending method has the downside of a slow reaction due to being computed every 60 seconds, as seen in Figure 6.3.

Since the filter detrending method managed to accommodate to the distortions in the SI, the corresponding detrended signal does not show any

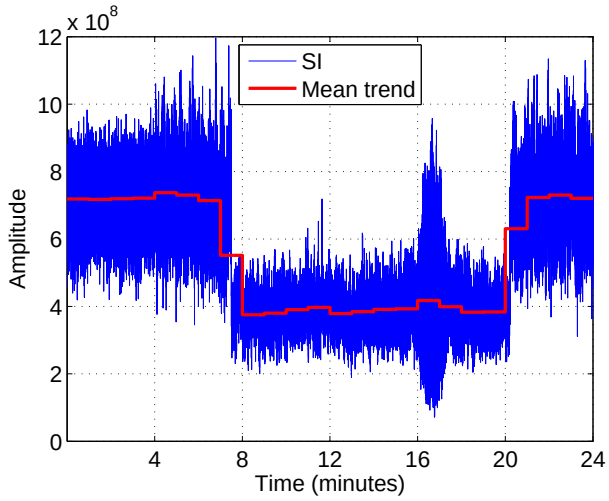

Figure 6.2: SI vs. SI_{trend} in interference scenarios. Filter Detrending.

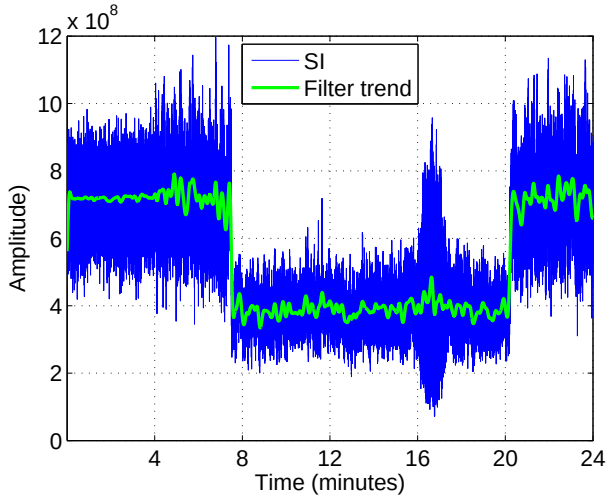

Figure 6.3: SI vs. SI_{trend} in interference scenarios. Mean value Detrending.

anomaly due to detrending operation, as it can be seen in Figure 6.4. On the other hand, given the rather long time window of the mean method every 60 seconds, the slow reaction of the mean detrending in following the SI creates distortions in the detrended signal when the change of gain due to the interference occurred, as observed in Figure 6.5.

Figure 6.6 shows the computed $S4$. Distortions can be seen with respect to the non interfered scenario, though these differ at some points from one detrending method to the other. For both methods, the lower C/N_0 estimated when interference is active caused the estimated S4 at some points to be set

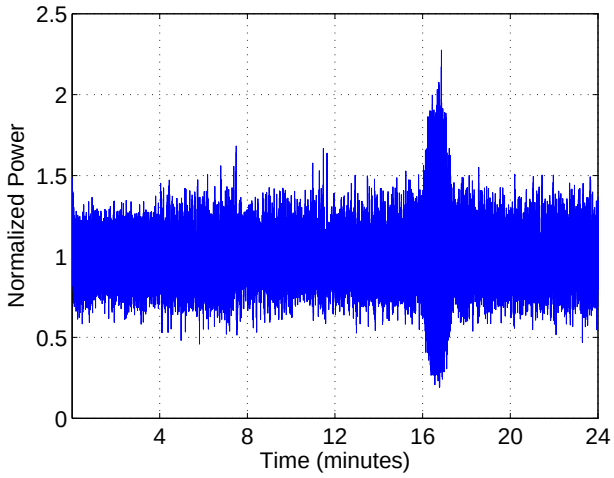

Figure 6.4: Detrended SI in interference Scenario. Filter Detrending.

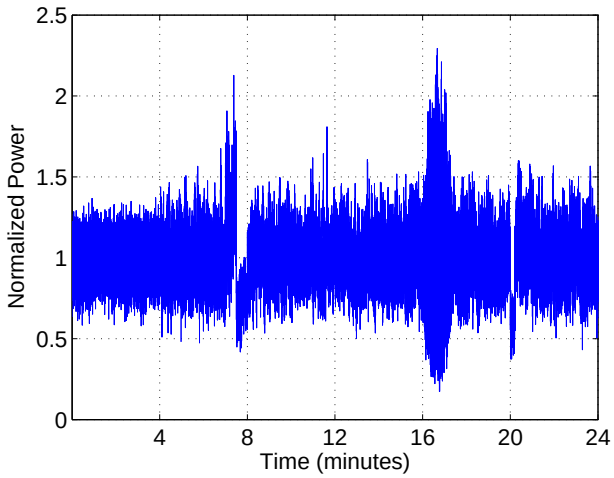

Figure 6.5: Detrended SI in interference Scenario. Mean value Detrending.

to zero, since it was deemed to be originated by only noise according to the S4 corrections performed as in (3.11) and (3.12). Both methods also show a big distortion around minutes 17 and 18, which correspond to the particular time when the frequency of the interference is in the vicinity or aligned with one of the code spectral components appearing every 1Khz for a C/A signal. As explained in Section 5.4, CWI has more degrading effects for the receiver at those frequency intersection points.

However, further distortions can be observed in the $S4$ calculated using the mean value detrending. Two extra peaks, one at minute 8 and the other at

minute 21, are in correspondence to the distortions detected earlier in the detrended signal. Once again, though the mean value detrending method is simpler and faster than the filter, its slow reaction in following the sudden variation levels of the SI makes $S4$ measurements performed with this method more susceptible to interference effects.

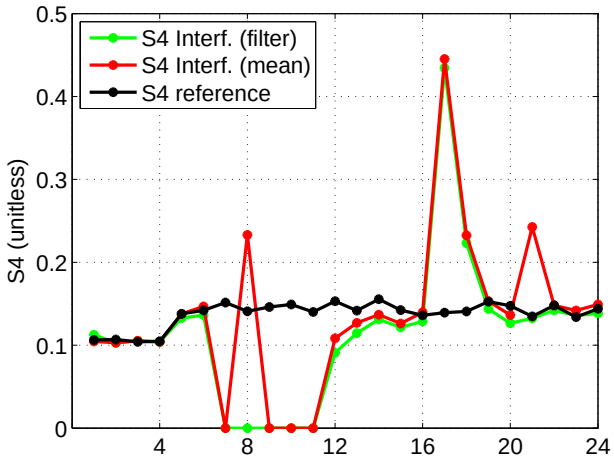

Figure 6.6: Measured S4 under CWI.

6.1.1.2 WBI Case

The calculated S4 for the two other cases of interference described in Section 5.4, Additive White Gaussian Noise and Chirp Signal, are shown in Figures 6.7 and 6.8 respectively. Similar to what was observed in the CWI case, distortions in the $S4$ are noticeable in particular when the mean value detrending method is employed. Both of these interference signals are considered as wideband with respect to the GPS L1 C/A signal, but in the case of the AWGN all of the interference power is within the considered band of the L1 C/A signal in our example scenario, whereas only a fractional part of the chirp signal power is actually in-band. The more interference power is present, the more the AGC compresses the useful signal and the bigger the peak distortions observed in the amplitude index, as noticed when comparing Figure 6.7 and Figure 6.8 for the two cases of wideband interferers. WBI

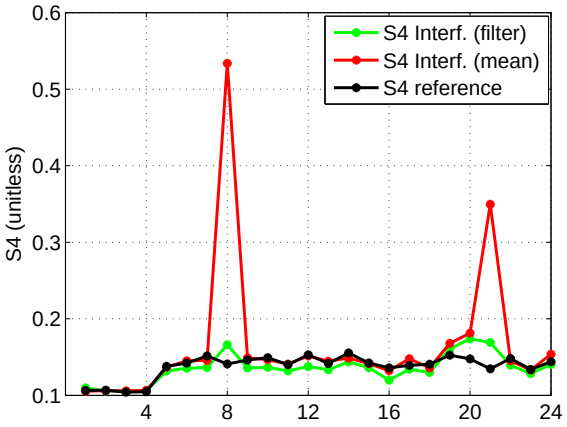

Figure 6.7: Measured $S4$ under WBI. AWGN case.

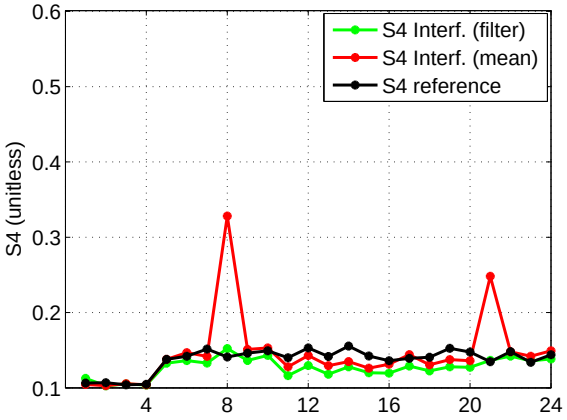

Figure 6.8: Measured $S4$ under WBI. Chirp signal case.

have no particular effects with respect to the spectral properties of the GNSS signals as was the case with the CWI and the spectral lines, therefore the biggest S4 distortion appearing at minute 16 in the CWI is not present in any of the WBI cases.

Results concerning the distortion due to the AGC are summarized in Table 6.2 for different interference power of both CWI and WBI types. For cases in which the interference power is high with respect to the signal and in particular for WBI, $S4$ values that went beyond the theoretical maximum value ($S4 = 1.4$) were found in the calculations and were readily discarded. The term Not valid identifies such cases in the table [56].

Table 6.2: Summarizing results of S4 peaks due to interference.

Type	Power (dB)	S4 variations	
		Filter Detrending	Mean Detrending
WBI	-120	Not valid	0.4 - Not valid
	-125	Not valid	0.4 - Not valid
	-130	0.2	0.4 - 1.1
	-135	0.1	0.3 - 0.6
CWI	-120	0.4	0.4 - 1.1
	-125	0.15	0.3 - 1
	-130	0.08	0.25 - 0.5
	-135	0.06	0.25

6.1.1.3 Turning off the AGC

To avoid the issues the AGC may introduce when monitoring ionospheric scintillations, some receivers give the optional choice to turn this particular feature off. The analysis of the scintillation-interference environment with this particular receiver configuration selected is then presented.

Figure 6.9 shows a comparison, in a CWI scenario, of the signal intensity estimated when the AGC is active versus the case when it is disabled. As it can be seen, when the AGC is disabled the compression effect previously present disappears. Now the signal has a constant gain even when the interference is affecting the signal. This translates into the actual detrending signals, as seen in Figure 6.10 and in particular for the mean value method, not presenting the distortions detected before at minutes 8 and 17.

Figures 6.11 and 6.12 show the newly calculated $S4$ for CWI and WBI cases. As a consequence of the absence of AGC effect, the peaks detected earlier when using the mean detrending method are no longer present and only the disturbances caused by the interference themselves remain. It is seen that due to its particular effects, the CWI is much more disruptive than the WBI when performing amplitude scintillation measurements.

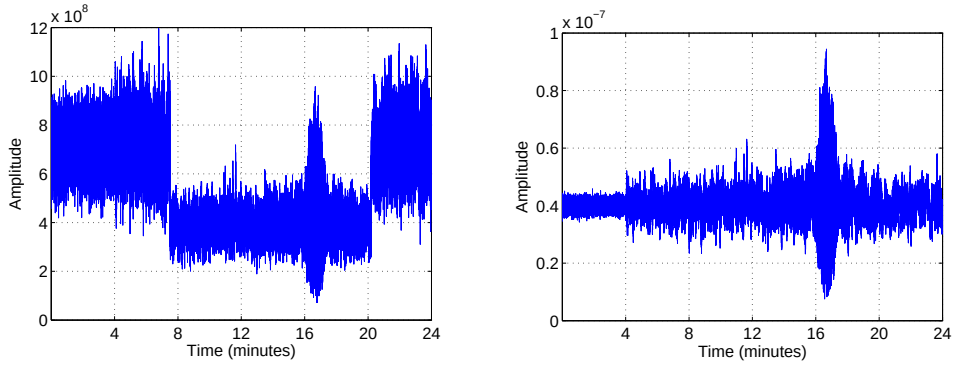

(a) AGC enabled (b) AGC disabled

Figure 6.9: Signal intensity under CWI.

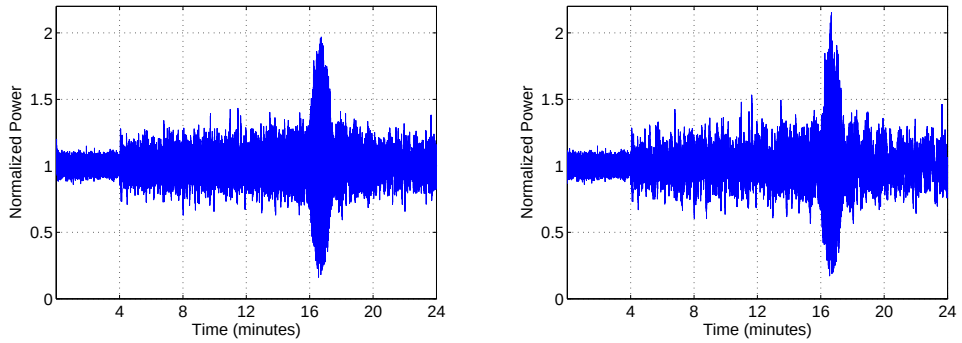

(a) Filter detrending (b) Mean value detrending

Figure 6.10: Detrended signal intensity under CWI: AGC disabled.

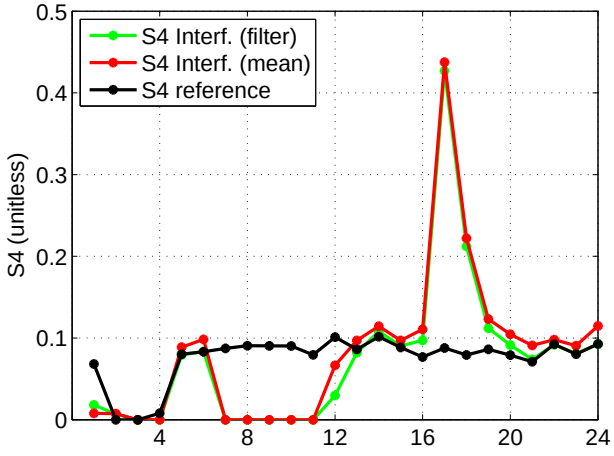

Figure 6.11: Measured S4 under Interference: AGC disabled, CWI case.

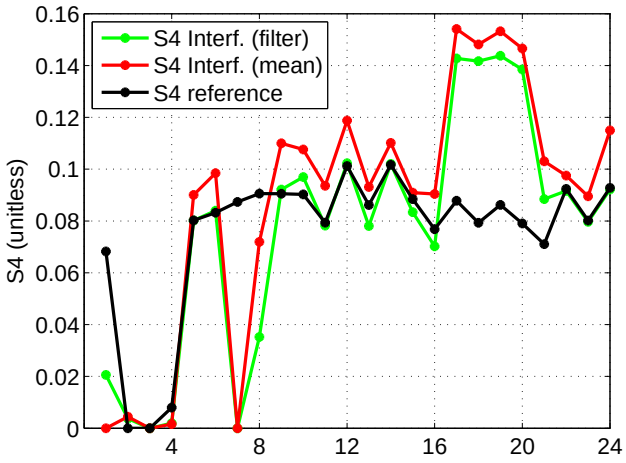

Figure 6.12: Measured S4 under Interference: AGC disabled, WBI case.

6.1.2 Effects on Phi60

Interferences also introduce additional phase disturbances that may fall in the frequency range of phase scintillations, thus disrupting the phase index measurements as well. How the *Phi*60 index could be affected is presented in the following for the CWI and WBI cases using the interference scenarios summarized in Table 6.1. As done for the $S4$, analysis will be performed by comparison with the non-interfered scenarios.

6.1.2.1 CWI Case

The phase error of the interfered signal versus the phase errors in the absence of interference are shown in Figure 6.13. An increase in the error variance is noticeable when the interference is present and, in the CWI in particular, the effect is more harmful when the interference frequency is in the vicinity or aligned with one of the code spectral lines, as it happens in this case around minute 17. Such errors in the phase estimate will ultimately impact the detrended phase measurements as well, as observed in Figure 6.14.

The estimated phase index can be seen in Figure 6.15, where it is noticeable that CWI mostly affects the phase measurements at the intersection point

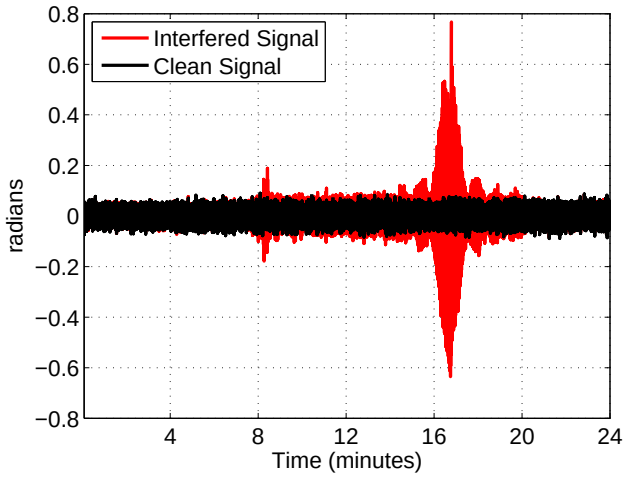

Figure 6.13: Phase observables under CWI. Phase Error.

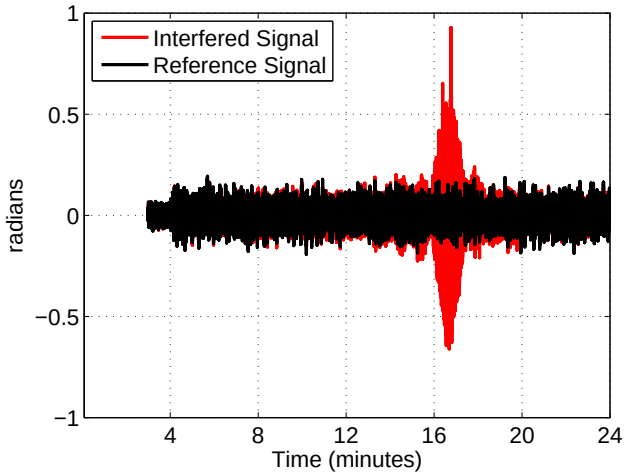

Figure 6.14: Phase observables under CWI. Detrended Phase.

with the code spectral lines. Beyond that particular moment, the index remains largely unaffected and maintain approximately the same value as when only scintillation is present.

The former can also be corroborated from the spectral point of view as in Figures 6.16 and 6.17, where a comparison of the power spectral density is shown for two different time frames while the interference is active: one at minute 7 when it is not aligned with a spectral component of the GNSS signal, the other at minute 17 when the CWI is more harmful (aligned). As seen in Figure 6.16, despite CWI being present it does not introduce particular

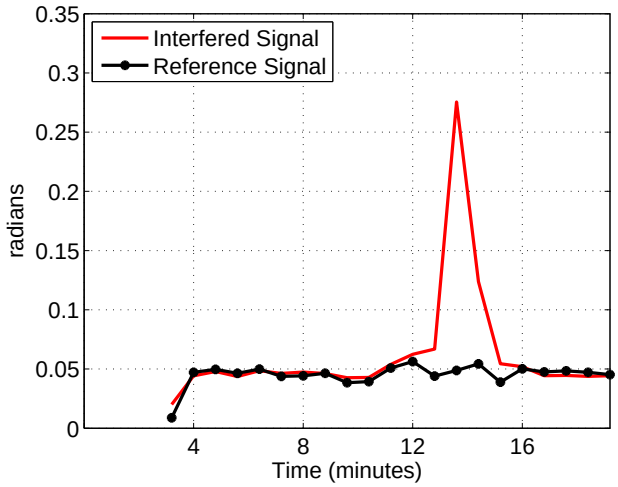

Figure 6.15: Phi60 under CWI.

phase distortions in the range of the phase scintillations. On the other hand, in Figure 6.17, it is evident that when CWI is at its worse, the distortions it induce in the receiver tracking have more power in the range of the phase scintillation, consequently affecting the output of the index.

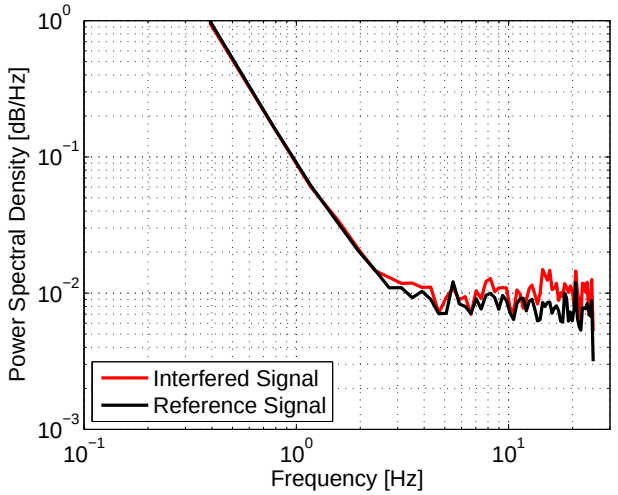

Figure 6.16: PSD of detrended phases samples under CWI when not aligned with a spectral component

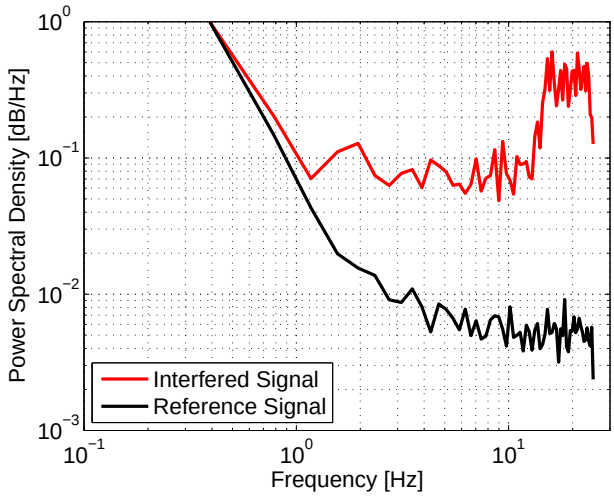

Figure 6.17: PSD of detrended phases samples under CWI when aligned with a spectral component

6.1.2.2 WBI Case

Once more, WBI effects differs from the CWI case. When WBI is present it can be taken as a steady increase in the noise floor [51]. In the case of AWGN, as shown in Figures 6.18 and 6.19, a uniform increase in the phase error variance and detrended phase measurements is observed that also translates into enhanced *Phi*60 measurements while the interference is affecting the system.

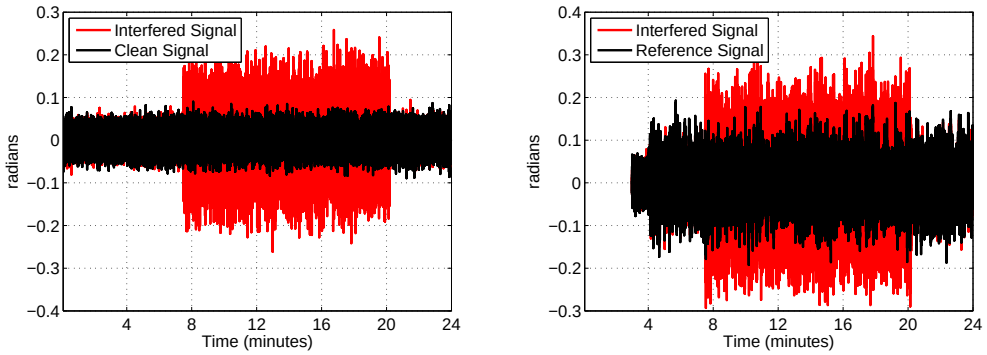

(a) Phase error (b) Detrended phase

Figure 6.18: Phase scintillation measurements under WBI: AWGN case. (1)

Similar effects are observed when the WBI has the form of a chirp signal, as

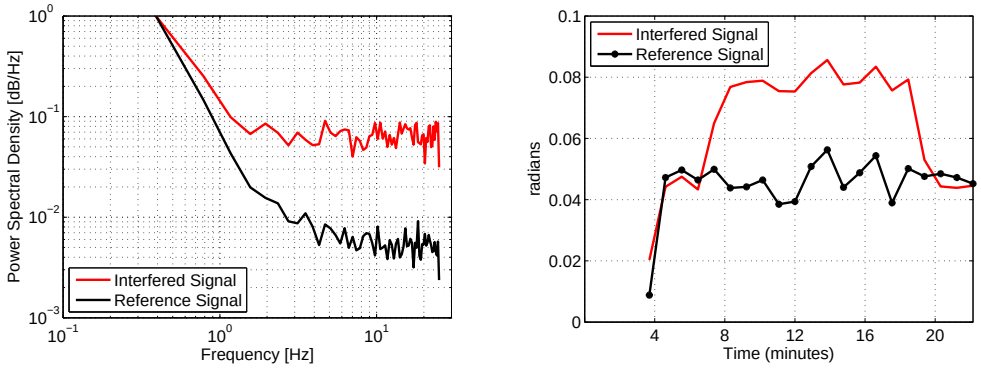

(a) PSD under WBI (b) Phi60

Figure 6.19: Phase scintillation measurements under WBI: AWGN case. (2)

shown in Figure 6.20. In this case, however, since the actual power of the interference affecting the system is lower the effects are less pronounced as well.

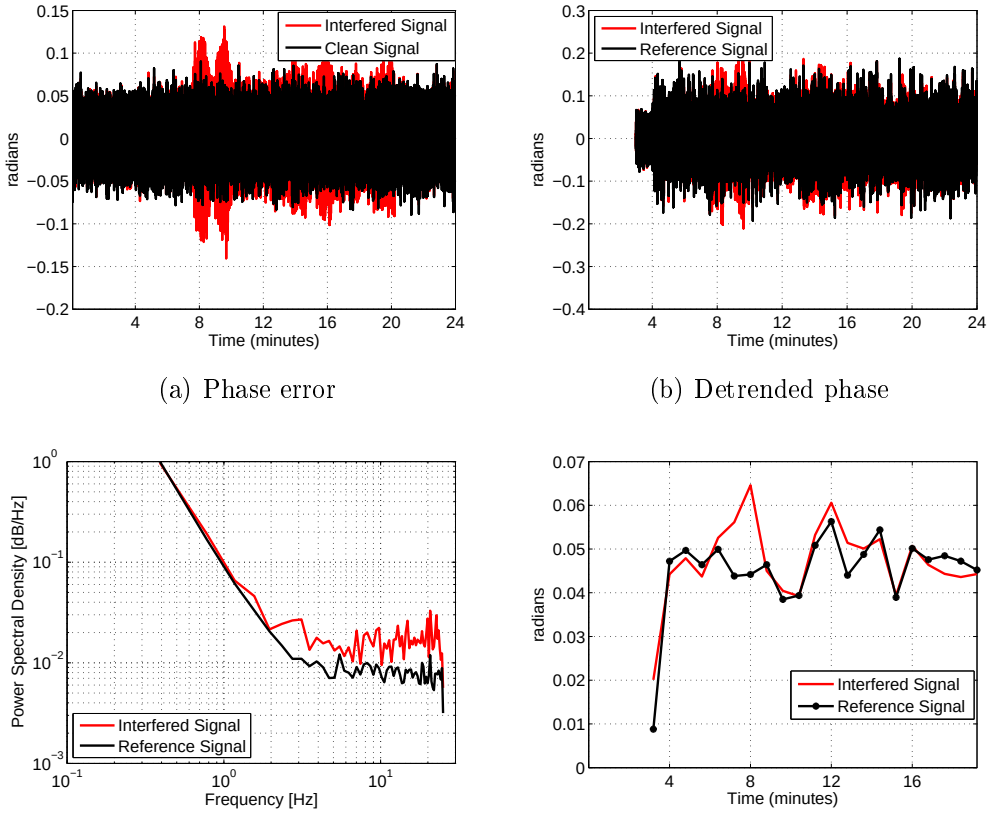

(a) Phase error (b) Detrended phase

(c) Detrended phase PSD (d) Phi60

Figure 6.20: Phase scintillation measurements under WBI: Chirp Signal case.

As part of the analysis, tests were also performed when the AGC in the receiver front-end is turned off. However, the AGC was not expected to change the behaviour of the Phi60 index whether it is disabled or not, as it has no incidence in the phase measurements. As observed in Figures 6.21 and 6.22, beyond the interference effect the phase index shows no difference regardless of the status of the AGC.

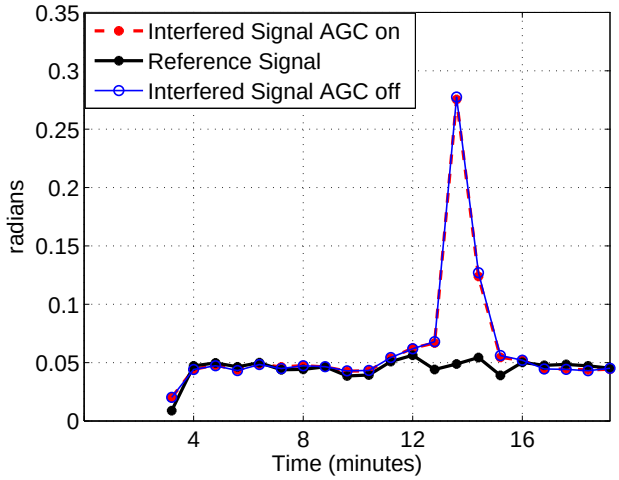

Figure 6.21: Phi60 under interference: Case AGC turned off: CWI

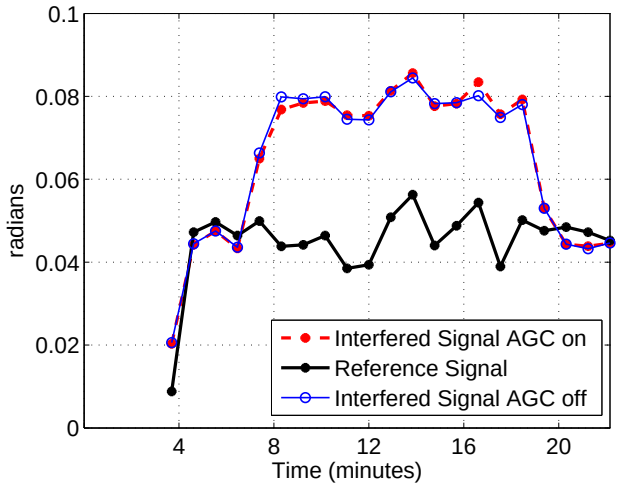

Figure 6.22: Phi60 under interference: Case AGC turned off: WBI

6.2 Characterization of Continuous Wave Interference on GPS Scintillation Measurements

From our previous analysis presented in Section 6, how much the scintillation indices are affected by interference may largely depend on the type of interference signal. Given the particular effects of the Continuous Wave interference, it has shown more potential to affect the estimation of ionospheric scintillation activity when compared to the Wideband interference cases studied. In this section we will review the effects of CWI in more detail. The analysis will focus solely on the composite input signal characteristics, mainly its scintillation level and the power and offset of the continuous wave interference with respect to the GNSS scintillating signal. Receiver dependant effects such as the one introduced by the AGC will be neglected by considering this particular feature disable, thus the gain on the signal is to be considered constant during the full length of the tests and the CWI is always actively affecting the signal.

6.2.1 CWI Effect According to Scintillation Level

Fluctuations in amplitude and phase introduced by the CWI mislead the measurements of both $S4$ and $Phi60$ indices. However, the impact of the CWI over the scintillation indices may also be dependent on the actual level of scintillation fluctuation affecting the GNSS signal. For a signal strongly fluctuating due to scintillations, the range of perturbations induced by the CWI can in fact fall below such fluctuations, thus not being noticed. Test cases examining such scenarios are presented next. Table 6.3 shows a summary of the most relevant signal characteristics of our simulations. Specifically, three different scintillation scenarios are considered for the GNSS signal: absent/low, moderate and strong scintillations. The power of the continuous

wave interference is fixed and its offset with respect to the carrier frequency is in the range of few kilohertz , which is when the CWI is more harmful for the acquisition and tracking stages of the receiver[10]. Considering the initial doppler and doppler rate of the signal, the continuous wave is aligned with a code spectral line around minute 17, and it is around that moment when most of the effects will be noticeable in all the following tests.

Table 6.3: CWI effect according to scintillation level.

Parameter	**Value**
Frequency band	GPS L1
Nominal C/N_0	49dB/Hz
Doppler frequency	2KHz
Doppler rate	1Hz/s
Scintillation levels	Weak/Moderate/Strong
Intermediate Frequency IF	3MHz
CWI f_{offset} w.r.t. IF	25KHz
CWI Power	-130dB

6.2.1.1 No Scintillation / Low Scintillation Cases

As analyzed in Section 6.1.1.1, the lower C/N_0 measured while the interference is active will cause the $S4$ index to be set to zero. The most noticeable effect will largely show when the CWI effect is at its worse near the code spectral lines, for both amplitude and phase indices. The latter effect however, depends on the amount of power allocated to the particular spectral line according to its coefficient in the code spectrum, which differ from satellite to satellite [57] [58]. As a consequence, even though the most noticeable effects coincide for all satellites every 1KHz of doppler frequency (for GPS L1 C/A signals), the impact on the indices varies according to the code spectrum of each particular satellite and its doppler frequency. Figure 6.23 shows an example of this scenario for three different satellite signals affected by low scintillation.

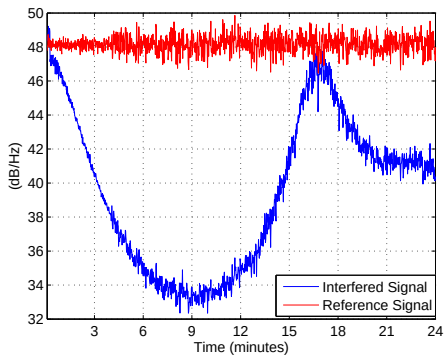

(a) C/N_0 PRN1

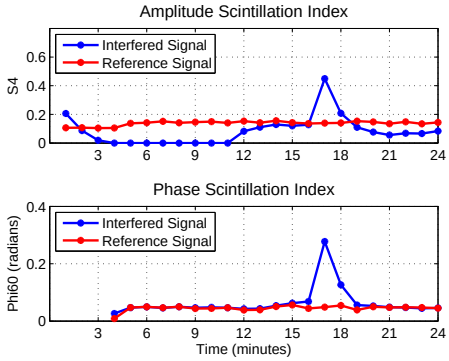

(b) Scint. indices PRN1

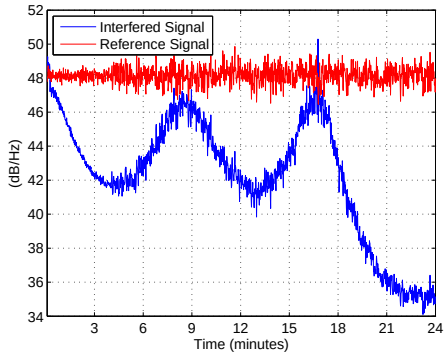

(c) C/N_0 PRN2

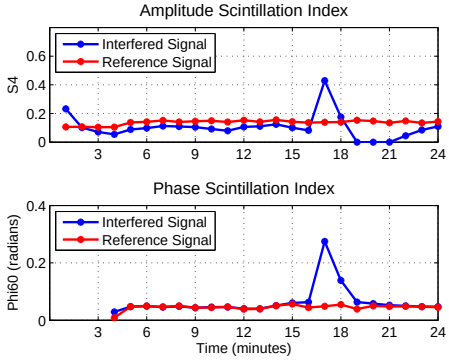

(d) Scint. indices PRN2

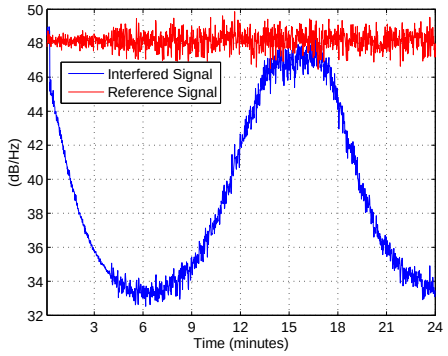

(e) C/N_0 PRN3

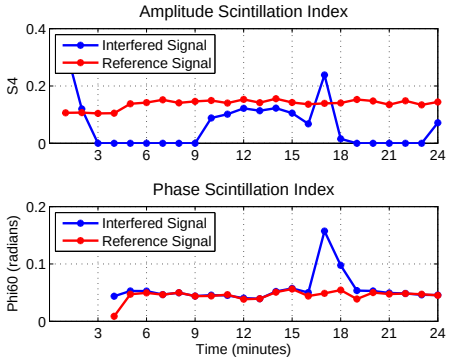

(f) Scint. indices PRN3

Figure 6.23: CWI effect in a weak scintillation scenario.

As seen in the Figure 6.23, despite being affected by the same interference not all satellites reflect the effects at the same level. Differences in the estimated C/N_0 and scintillation indices are noticeable from one satellite to the other due to the particular way in which CWI affects the GNSS signals, that is dependent to the particular line spectrum of each satellite code. In the

example scenario, as it is a case with low scintillation both $S4$ and $Phi60$ indices show a significant response mainly when the CWI is at its critical effect around minute 17. At that moment, as the interference gets in the vicinity of a code line frequency the phase errors at the PLL tracking stage increase, as compared in Figure 6.24 for the clean and interfered signals of PRN1. This affects both the correlations and phase measurements observables on which the computation of the scintillation indices are based.

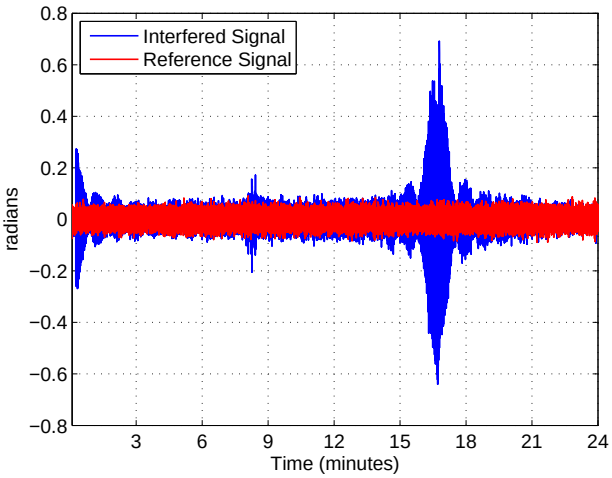

Figure 6.24: Phase errors PRN1.

In this particular scenario all of the satellites initial doppler frequency was set at the same value, in order to showcase how the effect of the continuous wave interference over the scintillation indices varies from satellite to satellite under the same conditions. Indeed, the CWI triggered a response of the ionospheric indices estimation of the satellite signals and may consequently raise a false alarm of detected scintillation events in the receiver channels. It is, however, not a likely case to present simultaneously in several channels as each satellite signal will have a different doppler frequency value.

Nevertheless, the behaviour of the index suggest that in a scenario where the continuous wave interference is actively present for a long time, upon observation in the long period, it could be possible to discard the measurements as being originated from scintillations. Scintillations are dependent on the

portion of the ionosphere traversed by each satellite signal, it is not an effect that would appear deterministically as a repetitive pattern. The fact that they are random is the reason why scintillations are so difficult to anticipate.

However, if the satellite signal is already affected by a significant amount of scintillation when the interference takes effect it might not be possible anymore to notice the presence of interference just by observation of the scintillation indices. Following two cases take a look to such scenarios.

6.2.1.2 Moderate Scintillation Cases

The same CWI acting on a moderate scintillation scenario can be observed in Figures 6.25 and 6.34.

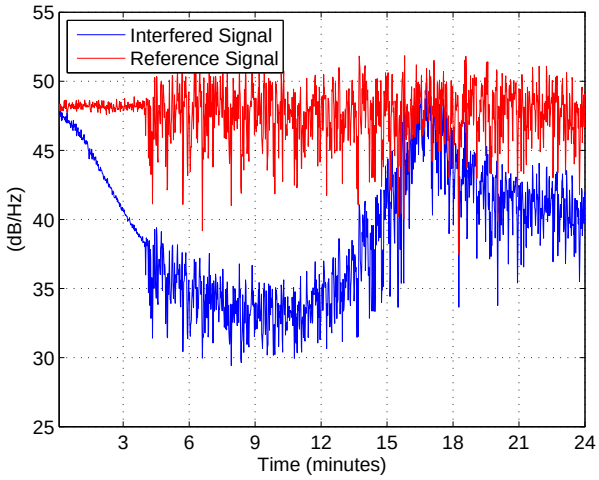

Figure 6.25: CWI effect in a moderate scintillation scenario. C/N_0.

Comparing with the no scintillation scenario presented before, the effects are not immediately noticeable in the scintillation measurements in this case. Now the fluctuations in amplitude and phase induced by the interference are, for the most part, below those induced by scintillations except when the continuous wave frequency is on alignment with a code spectral lines. Looking at the $S4$ index in Figure 6.25, the presence of the interference signal goes unnoticed. The effect on the Phi60, as shown in Figure 6.34, is only noticeable

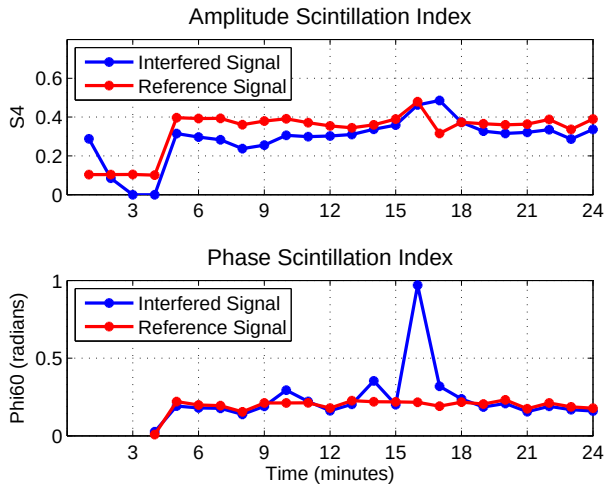

Figure 6.26: CWI effect in a moderate scintillation scenario. Scintillation indices.

when the CWI effect is at its worse during minute 17 due to the increase in phase distortions but could readily be mistaken as scintillation activity.

However, the combined effect of scintillation and interference makes phase scintillation measurements more susceptible to errors as well, potentially neglecting the phase estimation of the events if losses of lock occurs. Figure 6.27 shows the overall increase in tracking phase errors as compared to the reference case without interference.

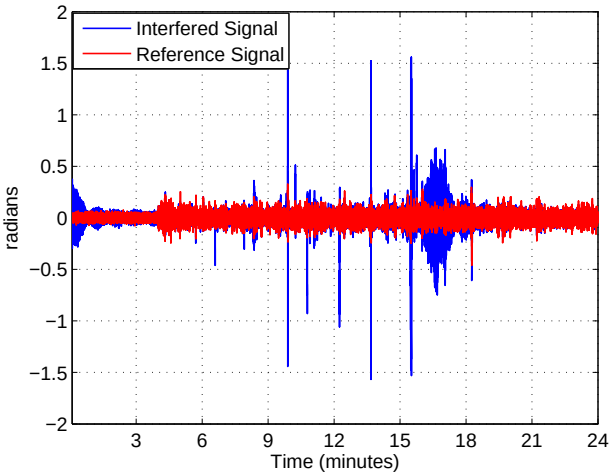

Figure 6.27: Phase errors.

6.2.1.3 Strong Scintillation Cases

An example of the CWI acting on a strong scintillation scenario is presented in Figures 6.28 and 6.29.

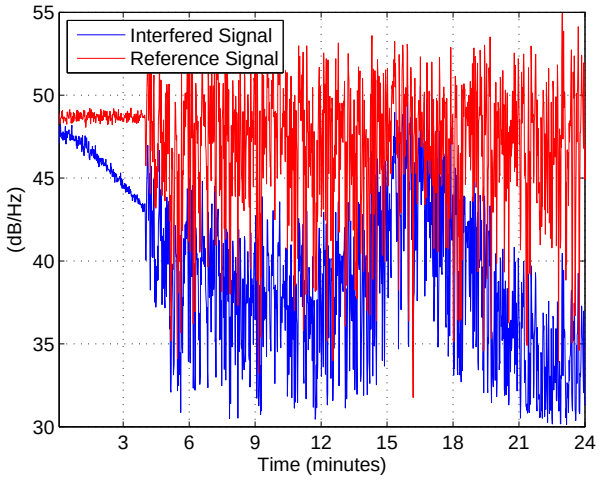

Figure 6.28: CWI effect in a strong scintillation scenario. C/N_0.

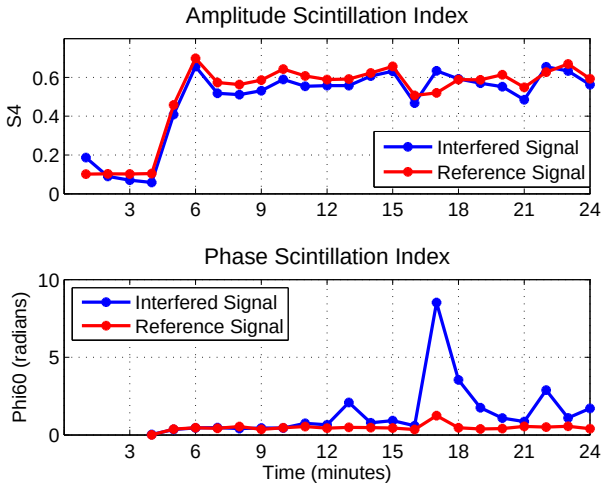

Figure 6.29: CWI effect in a strong scintillation scenario. Scintillation indices.

The estimated $C/N0$ for the present scenario can be observed in Figure 6.28. Figure 6.29 shows the estimated ionospheric indices. It can be observed that $S4$ remains quite unaffected by the presence of the interference. This suggests that signal power fluctuations due to the continuous wave are not greater

than those induced by the scintillation activity. On the other hand, due to the increased phase errors the phase index presents large deviations to the point of becoming unusable. This is because on top of the phase errors due to scintillations, now the receiver has to cope with the phase disturbances due to the CWI as well, as seen in Figure 6.30. Strong scintillation activity

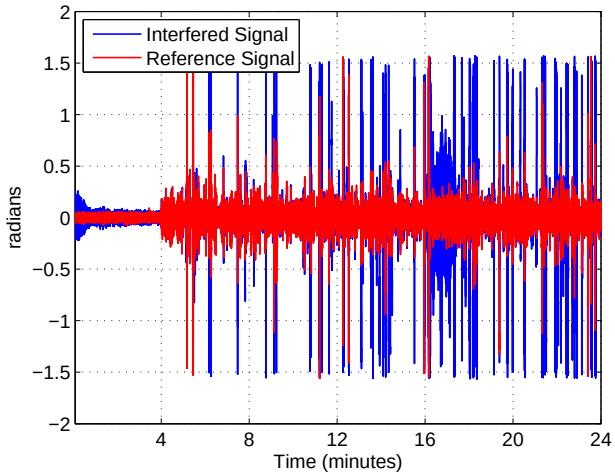

Figure 6.30: Phase errors.

already stresses the tracking architecture of the receivers to the point where losses of lock of the signal occurrence increases. This affects at the same time any measure of phase scintillations, a problem that is only made worse by the presence of interference that complicates any estimation of phase scintillation activity.

6.2.2 CWI Effect According to Frequency Offset

Continuous wave interference attenuates greatly the performance of the GNSS receiver when its frequency coincides or is near the code spectral lines as seen from the previous section, but such effect is also in general more disrupting when the interference frequency is at or close to the maximum of the signal spectrum. Having this in mind, the following scenarios show how the CWI effect can change according to the frequency offset between its frequency and

that of the carrier of the GNSS signal. Table 6.4 shows a summary of the most important signal characteristics relevant to the tests.

Table 6.4: CWI effect according to frequency offset.

Parameter	**Value**
Frequency band	GPS L1
Nominal C/N_0	49dB/Hz
Scintillation level	Moderate
Intermediate Frequency IF	3MHz
CWI f_{offset} w.r.t. IF	25/525/1025 KHz
CWI Power	-130dB

As seen from the table, the scintillation activity will be kept to a moderate level and the power of the interference is also fixed to a moderate value of -130dB. The CWI effect will be reviewed by solely changing its frequency offset with respect to the intermediate frequency of the GPS L1 C/A signal. To recall, the main lobe of that signal concentrates most of the power of the signal and has a bandwidth of 2MHz. Scenarios are based on the continuous wave being in the vicinity of the carrier frequency or center of the main lobe, and halfway and outside the main lobe.

6.2.2.1 CWI in the vicinity of GNSS Carrier Frequency

The spectrum of the GNSS signal affected by the interference can be seen in Figure 6.34(a), where it is visible that the continuous wave is right at the center frequency of the spectrum. Figure 6.34(b) shows the estimated $C/N0$ under the current scenario.

Figure 6.32 shows the estimated scintillation indices, where it is seen that the CWI close to the carrier frequency causes disruptions to both $S4$ and $Phi60$ indices. For the latter in particular, the effects are more disruptive when the continuous wave is in the vicinity of one of the spectral components of the code due to the increased phase errors in the receiver tracking.

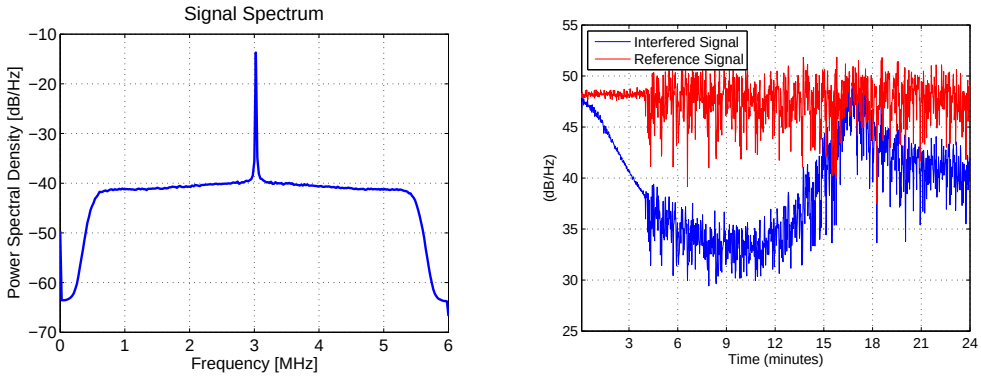

(a) Spectrum (b) C/N_0

Figure 6.31: CWI effect in a moderate scintillation scenario. $f_{offset} = 25KHz$ (1)

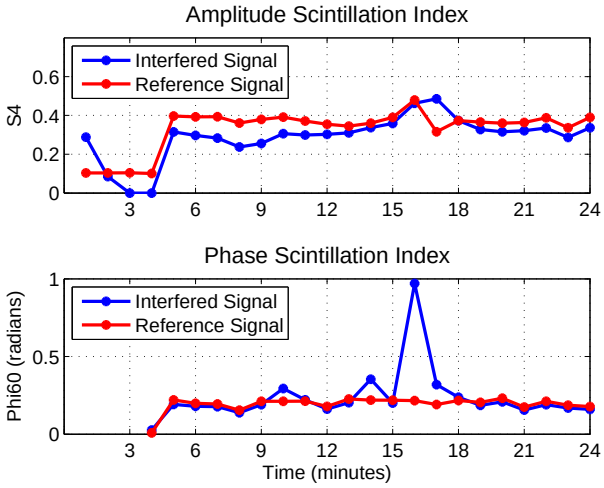

Figure 6.32: CWI effect in a moderate scintillation scenario. $f_{offset} = 25KHz$ (2).

6.2.2.2 CWI half-way the Main Lobe

Figure 6.33 and 6.34 show the scenario where the continuous wave is at the middle of the main lobe of the code spectrum, or roughly 500KHz apart from the GNSS carrier frequency. The spectrum of the signal at intermediate frequency can be seen in Figure 6.33(a). The estimated $C/N0$ for the current scenario can be seen in Figure 6.33(b). Figure 6.34 shows the estimated scintillation indices, where a decrease in the effects of the continuous wave over the indices is observed with respect to the previous case of the interference

signal being at the center frequency. Due to the lower $C/N0$ that is used for corrections, the measured amplitude index S4 appears slightly underestimated but follows in any case all the trends from the reference case without interference. Effects on the phase index Phi60 are greatly reduced as well as the continuous wave incidence over the tracking is less disruptive.

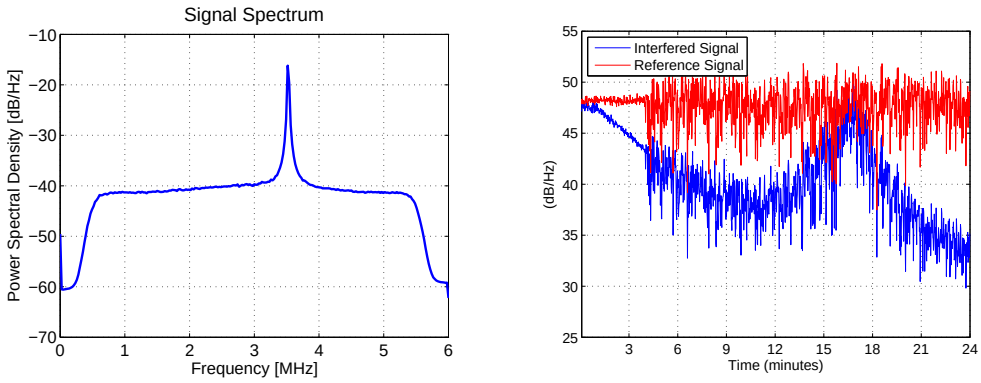

(a) Spectrum (b) C/N_0

Figure 6.33: CWI effect in a moderate scintillation scenario $f_{offset} = 525KHz$ (1).

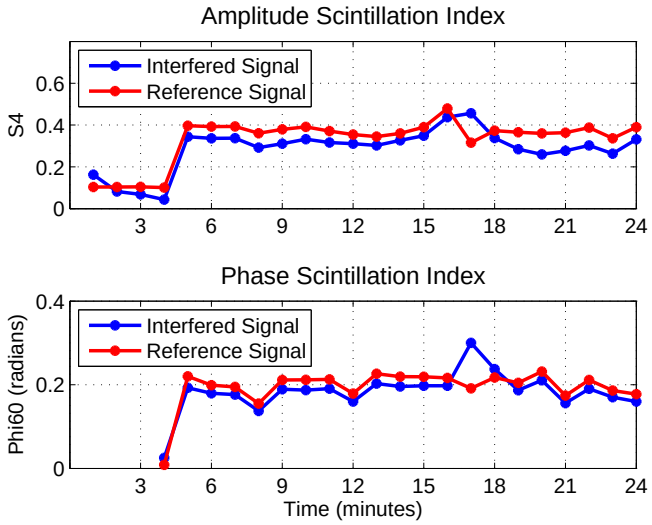

Figure 6.34: CWI effect in a moderate scintillation scenario. $f_{offset} = 525KHz$ (2).

6.2.2.3 CWI outside the Main Lobe

Finally, Figure 6.35 shows the scenario when the CWI falls outside the main lobe of the C/A signal or correspondingly, it is more that 1MHz apart from the carrier frequency. Figure 6.35(a) shows the spectrum of the scenario, where it is to be considered that the interference is outside the main lobe as $f_{offset} = 1025KHz$). Figure 6.35(b) shows the phase errors from the PLL tracking, where it is observed that the interfered scenario phase errors are at the same level of those of the reference scenario without interference.

Because in this scenario the effect of the interference in the receiver is quite negligible, no effect is observed for both the C/N_0 in Figure 6.36(a) and scintillation indices estimations in Figure 6.36(b).

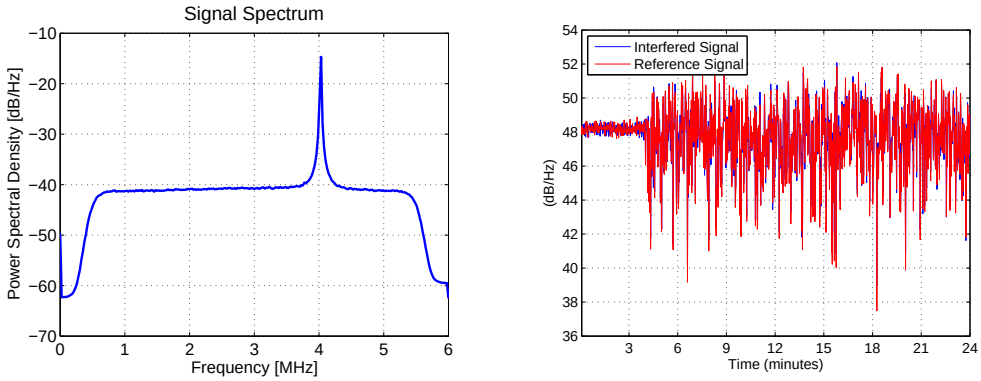

(a) Spectrum (b) C/N_0

Figure 6.35: CWI effect in a moderate scintillation scenario $f_{offset} = 1025KHz$ (1).

6.2.3 CWI Effect According to Power

Not only is the frequency offset of the continuous wave interference important but also how much power the it has with respect to the GNSS signal. The more power the interference has, the more disruptive will be its effects on the receiver. Table 6.5 shows a summary of the most important signal characteristics relevant to the tests.

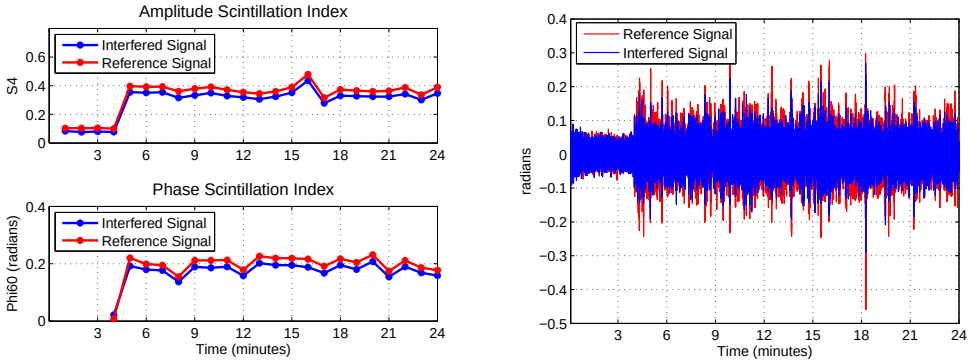

(a) Scintillation Indices

(b) Phase errors

Figure 6.36: CWI effect in a moderate scintillation scenario $f_{offset} = 1025KHz$ (2).

Table 6.5: CWI Effect According to Power

Parameter	**Value**
Frequency band	GPS L1
Nominal C/N_0	49dB/Hz
Scintillation level	Moderate
Intermediate Frequency IF	3MHz
CWI f_{offset} w.r.t. IF	25KHz
CWI Power	-125/-130/-135 dB

It is seen in the table that for the following scenarios the scintillation activity will be kept to a moderate level. The frequency offset of the interference is also set to just a few kilohertz apart from the carrier frequency. From previous analysis in Section 6.2.2, it is clear that such frequency offset will allow to observe the full effects of the interference in the signal. The CWI effect will be reviewed next solely by changing the interference signal power with respect to the GNSS signal

6.2.3.1 CWI Effect: High Power Case

A continuous wave interference with high power, $P_{cwi} = -125dB$, with respect to the GNSS signal that also happens to be very close to the GNSS signal carrier in the frequency domain is the worst case scenario of the ones analysed here. Even if the receiver is able to track trough both scintillations

and interference perturbations at some points, as the CWI effects get to their worse the receiver immediately loses lock of the satellite signal. This is corroborated in Figure 6.37(a) for the correlator outputs and Figure 6.37(b) for the phase errors, where it is observed track of the signal is kept until around minute 15 after which the signal is completely lost, i.e., when the interference frequency is in the proximity to one of the code spectral lines. Tough in the current example reacquisition was not implemented in the receiver, in general, immediate reacquisition of the satellite signal under such conditions may also prove to be problematic for receivers because of the presence of both scintillations and the strong effects of the CWI at such point.

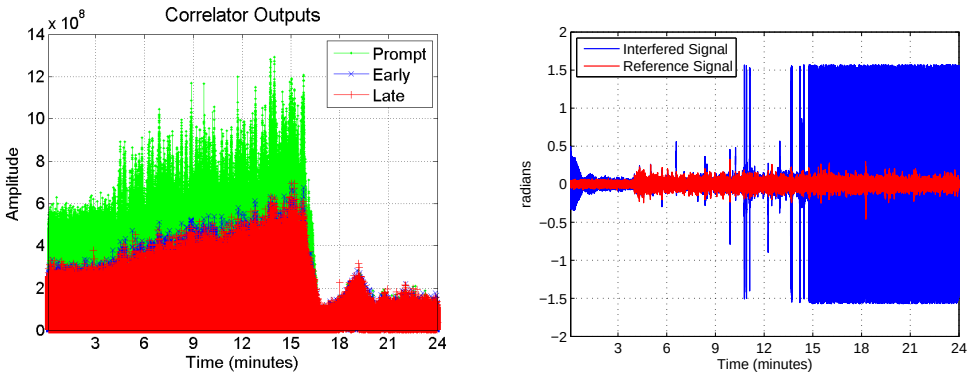

(a) Correlators (b) Phase error

Figure 6.37: CWI effect in a moderate scintillation scenario. High Power Case (1).

As a consequence the estimation of scintillation activity is totally disrupted. The estimated $C/N0$ for the current scenario is shown in Figure 6.38(a). Figure 6.38(b) shows the estimated ionospheric scintillation indices. As the receiver manages to track over the effects, the lower estimation of $C/N0$ causes the noise corrected $S4$ to be undervalued until the interference comes into full effect and the receiver losses track of the satellite signal. $Phi60$ on the other is a more unstable measurement as the increase in phase errors affects the quality of the phase measurements, directly impacting the estimations of the index as seen between minutes 9 and 12.

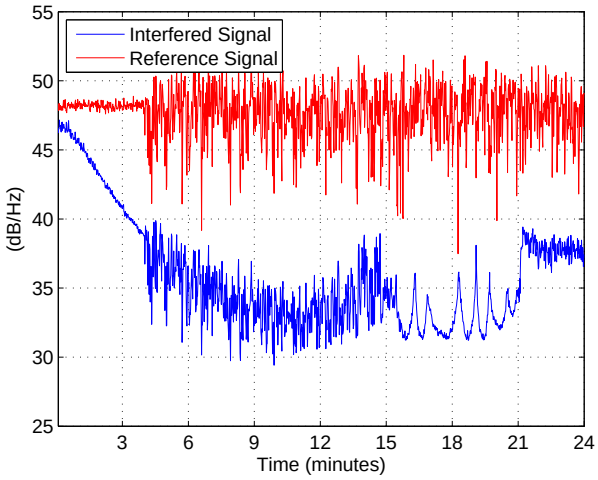

(a) C/N_0

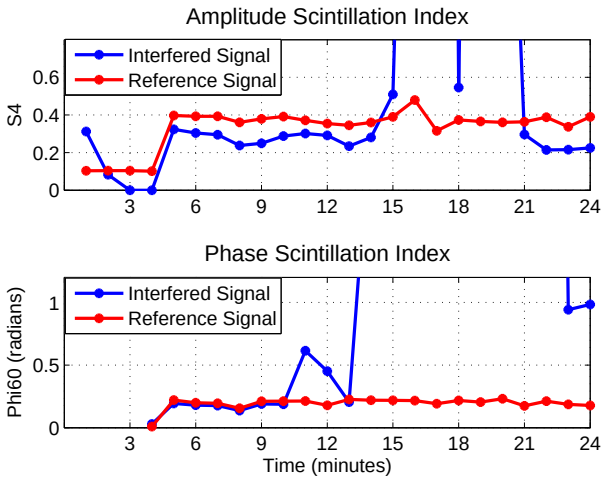

(b) Scintillation Indices

Figure 6.38: CWI effect in a moderate scintillation scenario. High power Case (2).

The definite worse case scenario would be if the satellite signal is already affected by strong scintillation. An example of such scenario can be seen in Figure 6.39. The combined effect of strong scintillation and high power interference induces the receiver to tracking errors that greatly reduce the monitoring capability of the receiver, as observed from the increase of phase errors in Figure 6.39(a). Figure 6.39(b) shows the estimated scintillation indices. The S4 seems resilient to the interference effects provided the receiver is able to keep track of the signal while the interference is not at its worst

effect, which will cause complete loss of lock. That may be because even though the high power of the interference signal induces fluctuations in the signal amplitude, these are not greater than those caused by scintillation. Phi60 on the other hand becomes a totally unreliable measurement as phase errors from the tracking loop are frequent. As the quality of the measurements is not accurate enough to guarantee a precise estimation of the phase, the receiver can't perform any monitoring of phase scintillations.

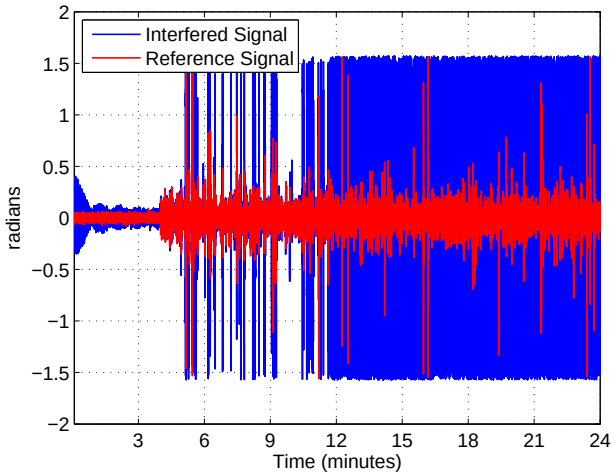

(a) Phase Error

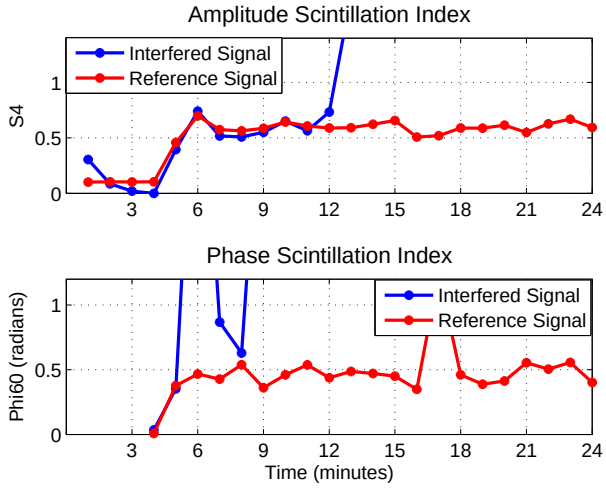

(b) Scintillation Indices

Figure 6.39: CWI effect in a strong scintillation scenario. High power Case (1).

6.2.3.2 CWI: Moderate Power Case

This case, as presented in previous tests in Figure 6.25 and replicated in Figure 6.40 for another satellite, disrupts mainly the Phi60 index. The estimated $C/N0$ can be seen in Figure 6.40(a) and scintillation indices are shown in Figure 6.40(b). With an average power of the continuous wave, $P_{cwi} = -130dB$, the receiver is able to track the signal trough the disturbances but the Phi60 measurements are not always reliable due to interference induced phase errors and consequent decrease of quality of phase estimates.

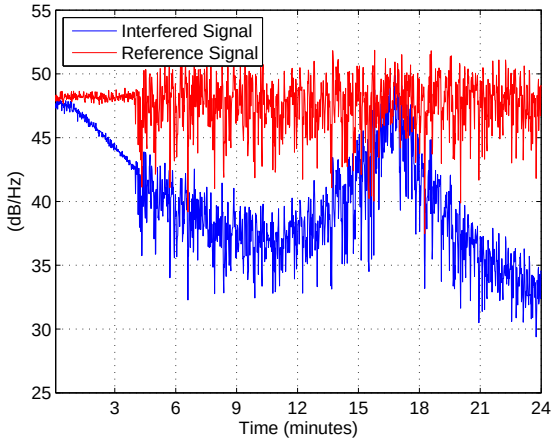

(a) C/N_0

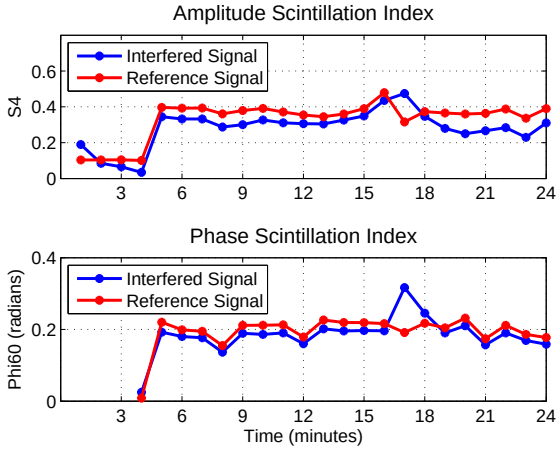

(b) Scintillation Indices

Figure 6.40: CWI effect in a strong scintillation scenario Moderate power case.

6.2.3.3 CWI: Low Power Case

Finally, Figure 6.41 shows the case of a continuous wave interference with weak power, $P_{cwi} = -135dB$, in comparison to the GNSS signal. As observed in Figure 6.41(a) for the $C/N0$ and Figure 6.41(b) for the scintillation indices, despite being close to the GNSS carrier the continuous wave interference effect are negligible.

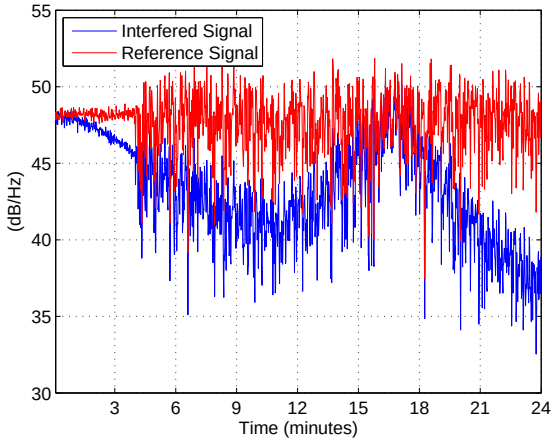

(a) C/N_0

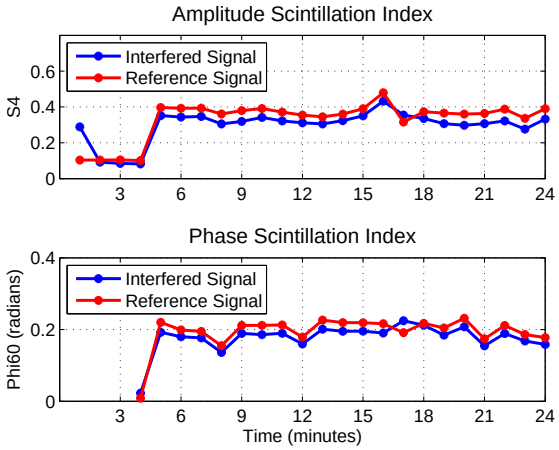

(b) Scintillation Indices

Figure 6.41: CWI effect in a moderate scintillation scenario
Weak power case.

6.2.4 The Galileo Case

The same scenarios of Sections 6.2.1, 6.2.2 and 6.2.3 were also performed using Galileo E1 signals. The findings were quite similar to what was reported previously for GPS when continuous wave interference power is considered. However, due to spectral differences of Galileo signals with respect to GPS the effects of the continuous wave itself are more frequent. As seen during the L1 C/A previous test scenarios the CWI is more harmful when it is aligned with one of the code spectral components, that for the C/A signal are spaced every 1KHz. For Galileo E1 signals, the code period is four times that of the L1C/A and the spectral components are now spaced every 250Hz. This means the continuous wave interference is four times more often aligned with spectral components when affecting a Galileo E1 signal compared to a GPS L1 C/A.

However, another interesting difference is that L1 C/A signal with its BPSK modulation concentrates power around the central frequency in a single main lobe, whereas Galileo signals and their CBOC modulation scheme split the power into two side lobes around the same central frequency, as seen in Chapter 2. As a consequence, when faced by the most critical effects of the CWI,the Galileo E1 has actually more resilience to it than its GPS counterpart [59].

To showcase these differences, an scenario was generated consisting of a scintillating(weak) Galileo E1B signal affected by a CWI with power $P = -125dB$, the highest power used in our GPS tests. The frequency offset was set to $f_{offset} = 1025KHz$, which means the continuous wave is in the vicinity of the center of the right main lobe of the E1 signal. Figure 6.42(a) shows the the correlator outputs, where it is seen that the presence of interference causes the signal power to fluctuate and will likely have an impact in the S4 estimation. Due to the longer code period the phase errors are more frequent for Galileo than what was observed previously in GPS cases, as seen in Figure 6.42(b), which suggest that phase index measurements will not be

reliable.

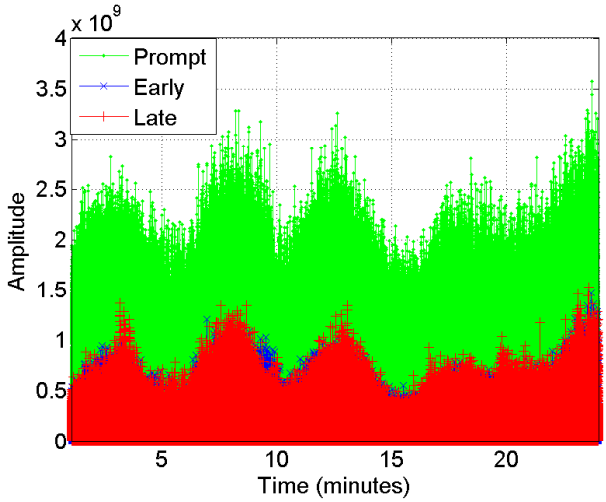

(a) Correlator outputs

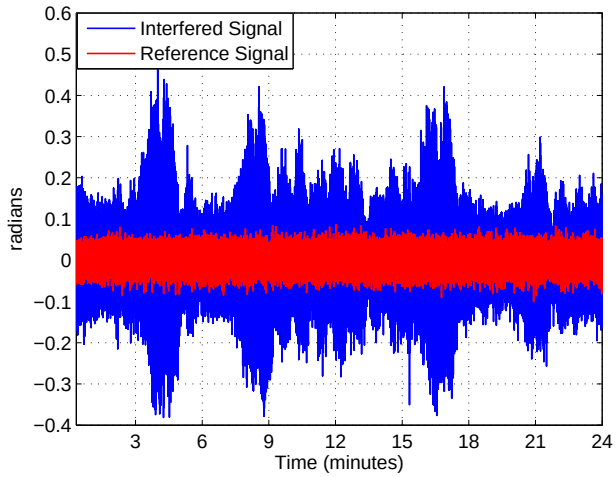

(b) Phase errors

Figure 6.42: CWI effect in Galileo E1B signal (1).

The estimation of $C/N0$ for the current scenario can be seen in Figure 6.43(a), while the estimated scintillation indices are shown in Figure 6.43(b). Receiver tracking effects of the continuous wave cause both amplitude and phase index to show an anomalous behaviour. As was the case in GPS, the lower $C/N0$ causes the S4 index to be set to zero at some points due to the noise factor correction. But as the disruptive effects of the continuous wave happens more often, the amplitude index presents more distortions when compared to an

analogous GPS case. The phase index Phi60 shows an even more erratic behaviour, since the frequent phase errors from the tracking continuously decrease the quality of the phase measurements.

CWI is more disruptive to Galileo signals in the context of ionospheric scintillation measurements, triggering both S4 and Phi60 into erroneous values every time the interference frequency is in the vicinity of the code spectral lines.

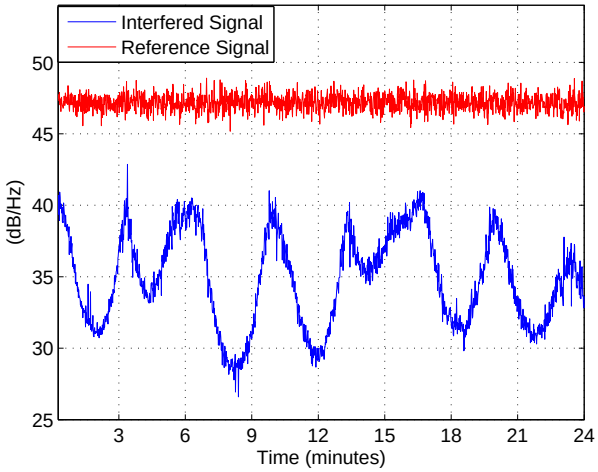

(a) C/N_0

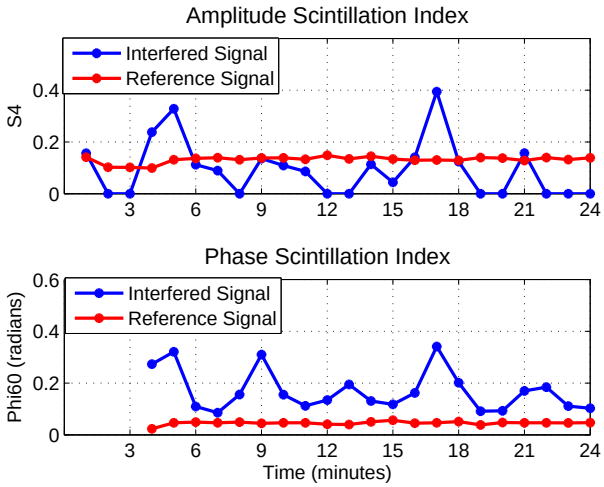

(b) Scintillation indices

Figure 6.43: CWI effect in Galileo E1B signal (2).

A continuous wave interference with the same properties just described, $P =$

$-125dB$ and $f_{offset} = 1025KHz$, was injected to a strong scintillating Galileo E1B signal in order to recreate a worst case scenario similar to the one analyzed for GPS. Correlator and phase error tracking outputs can be seen in Figure 6.44(a) and Figure 6.44(b) respectively. As noticed, the receiver was able to track through both the effects, whereas for the GPS it would immediately lose lock when the continuous wave would be in the vicinity of an spectral line. Here, despite the interference signal being aligned with a code spectral line four times as much as was the case with GPS, in this particular case the PLL was still able to keep track of the signal albeit with decreased quality of phase measurements.

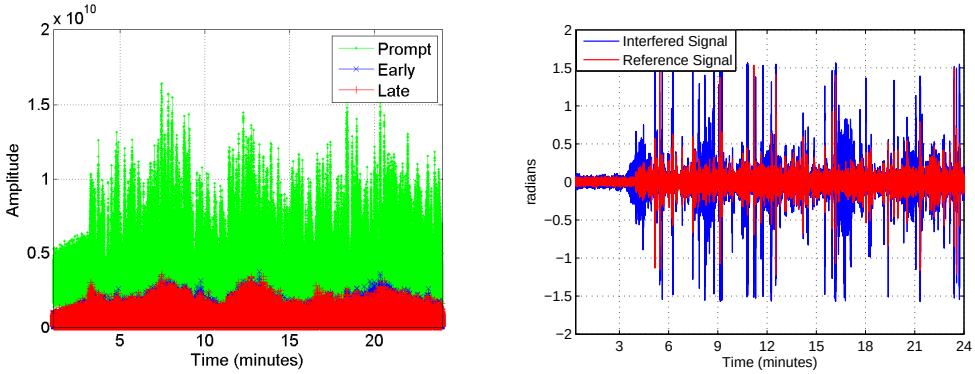

(a) Correlator outputs

(b) Phase errors

Figure 6.44: CWI effect in Galileo E1B signal (3).

The estimated $C/N0$ and scintillation indices for this scenario are shown in Figure 6.45(a) and Figure 6.45(a) respectively. Similar to the GPS cases (before the losses of lock), the estimated $S4$ is in agreement with the reference/non-interfered scenario. However, as was the case with $Phi60$ before, the decreased quality of phase measurements due to the interference can cause large errors to the phase index.

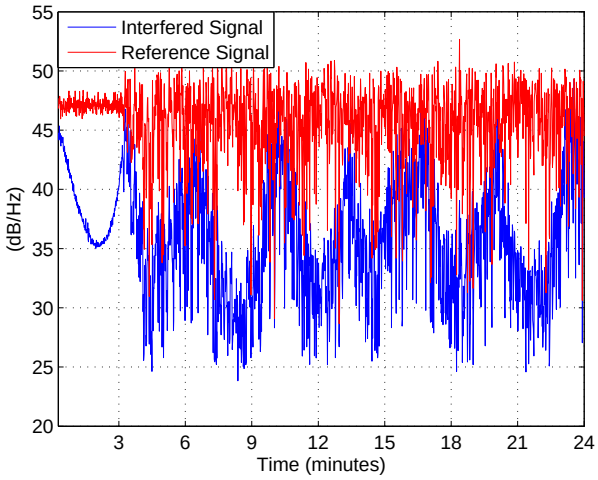

(a) C/N_0

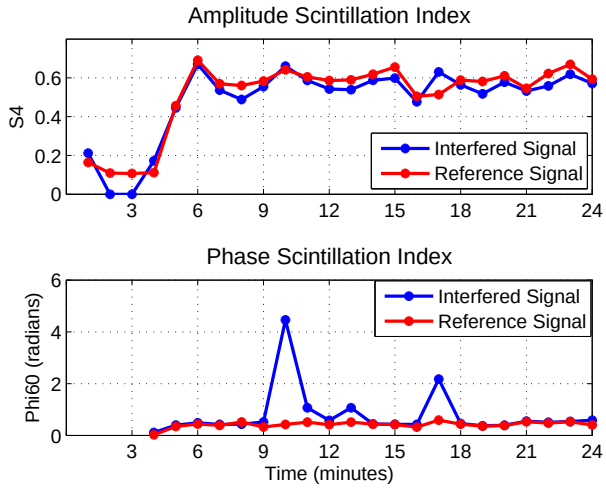

(b) Scintillation indices

Figure 6.45: CWI effect in Galileo E1B signal (4).

6.3 Summary

This chapter gave an overview to the possible disruption interference can introduce to scintillation monitoring activities. As there are many particular characteristics inherent to the type of interference three different type of spurious signals were analysed, namely, continuous wave, wideband noise and chirp signal. Interference induced errors in scintillation activity estimation were found in all three cases. However, the continuous wave interference has

in particular and more harmful effects than the other two types of interference analysed when its frequency is aligned with one the code spectral lines. As interference induced perturbations decrease the quality of receiver tracking estimations, this harmful effects are also translated into the scintillation monitoring estimations.

Given these effects of the continuous wave interference its effects were analysed in scintillating scenarios in more detail, by varying two of its key properties: Its frequency offset and power with respect to the GNSS signal . The worst case scenario for receiver tracking is that of a continuous wave in the vicinity of the carrier frequency that also happens to have high power, when the incoming satellite signal has a moderate or strong scintillation level. In such scenario the signals were completely loss in most of the cases. However, some interesting cases were found were interference power is not sufficient to cause a loss of lock, but induces sufficient distortions to trigger a response from the scintillation indices measurements. Such cases are the most problematic, since in the event interference is not detected it can mislead the detection of scintillation activity.

Chapter 7

Countermeasures to Interference in GNSS

GNSS receivers can be designed with precautions against interference such as bandpass RF filtering to minimize out-of-band interference, adequate number of quantizing levels, an appropriate AGC to ensure full processing gain, and careful design of the code and carrier tracking loops. However, sufficiently high levels of interference will overload any type of radionavigation system, and GNSS, even with spread spectrum techniques, are no exception [10].

Detection and mitigation of radio frequency signals interfering with the GNSS signals rely on the possibility to clearly identify the presence of spurious components and, possibly, to remove them, without damaging the structure of the useful signal. Once an interference signal is detected, GNSS receivers can activate mitigation techniques to counter its effects according to its time-frequency characteristics.

In a scenario where interference has been detected and mitigated, it might still be possible in some cases to retrieve the original ionospheric scintillation information embedded in the signal. The present chapter will give an overview of interference mitigation techniques in GNSS. In Chapter 6 it was shown that spurious signals such as continuous wave and wideband interferences can

mislead the estimation of scintillation activity. Our interest in this chapter is to investigate whether for a scintillating signal affected by interference, the scintillation information can still be extracted once the interference has been mitigated.

Interference Mitigation

Digital signal processing techniques proposed in literature to deal with Radio Frequency interference in the GNSS bands are, in general, classified according to the domain in which the interference mitigation is implemented [60]:

- **Frequency domain techniques:** Interference suppression is performed in the frequency domain, looking at the characteristics of the spectrum of the interfered GNSS signal that is received.

- **Time domain techniques:** Here, either receiver parameters are modified depending on the characteristics of the received signals in order to mitigate the impact of interference on the following stages, or a gating operation is carried on the GNSS signal itself in order to cut off portions of the signal that are believed to be affected by the interference.

- **Time-Space domain techniques:** Based on the principle of spatial filtering, introducing attenuation in the direction of arrival of the interfering signals. Such techniques typically require complex hardware configurations as they are implemented, in general, by exploiting antenna arrays.

However, it can be useful to search for a representation of the received signal in a domain different from the classical time and frequency domains where useful and spurious contributions can be better isolated. Such new family of algorithms are referred as **Transformed Domain (TD) techniques** and will also be analysed.

7.1 Frequency Domain Techniques

The approach of these techniques is to filter out the harmonic components of the interfering signal while preserving as much as possible the original spectrum of the GNSS signal. They are effective when the interfering signal occupies a limited portion of the frequency spectrum, i.e., it can be classified as NBI or CWI. On the other hand, the techniques are weak against pulsed interference, as the presence of the interfering signal for a limited time is often lost in the phase of spectral estimation.

7.1.1 Notch filter

It is an efficient mitigation algorithm for pure sinusoids family of interfering signals, such as the continuous wave interference described in Chapter 5, which appears as a spike in the spectral domain. Notch filters are usually characterized by a pass-band frequency response with a very narrow portion of rejection spectrum in correspondence to the CWI carrier frequency, thus providing attenuation of the interfering signal and preserving as much as possible the useful GNSS signal spectral components. An example of notch filter frequency response is shown in Figure 7.1.

The most common implementation of notch filters is by means of Infinite Impulse Response (IIR) digital filters. A causal IIR filter can be written in terms of a general difference equation where the output signal at a given instant is the linear combination of samples of the input and output signal at previous time instant:

$$y[n] = -\sum_{m=1}^{N} a_m y[n-m] + \sum_{m=0}^{m} b_m x[n-m] \tag{7.1}$$

Given that CWI presents two spectra lines corresponding to the frequencies f_i and $-f_i$, the transfer function in Z-domain of a two-pole notch filter for

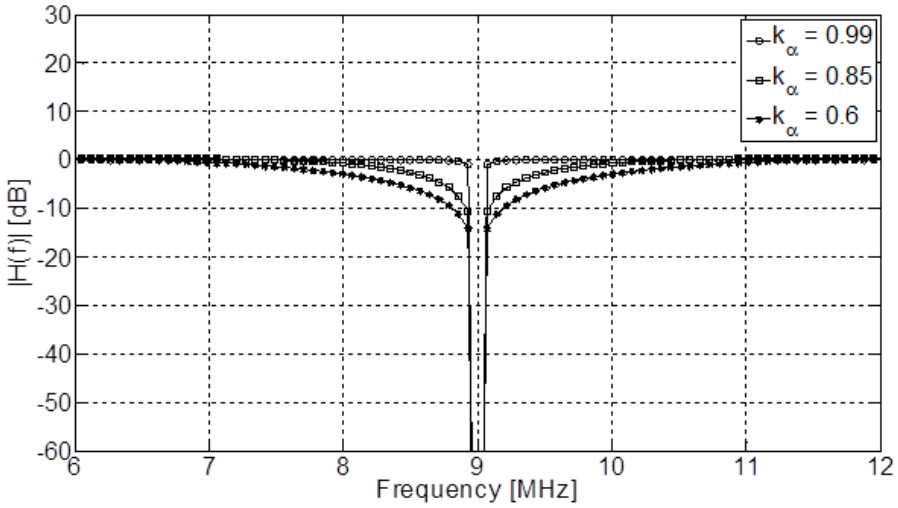

Figure 7.1: Notch filter frequency response.

CWI mitigation is given by [61]:

$$H(z) = \frac{1 - 2\Re\{z_0\}z^{-1} + \mid z_0 \mid^2 z^{-2}}{1 - 2k_\alpha\Re\{z_0\}z^{-1} + k_\alpha^2 \mid z_0 \mid^2 z^{-2}} \tag{7.2}$$

where z_0 is placed in correspondence of the interfering frequency $z_0 = \beta exp\{j2\pi f_i\}$. The parameter $0 < k_\alpha < 1$, known as pole contraction factor, determines the width of the notch filter. The closer k_α is to the unity the narrower is the notch filter. This would mean a reduction of the distortion on the useful GNSS signal, however, k_α cannot be chosen arbitrarily close to unity for stability reasons and thus a compromise has to be found.

Interfering signals might also change their spectral characteristic in time, thus requiring a flexibility of the mitigation unit to adapt to the actual interfering scenario. This may be the case of low-cost commercial jammers that aim at disturbing a wider portion of the spectrum, frequency-modulating a narrow-band signal in order to span a larger frequency interval over time. In those scenarios, techniques such as the Adaptive Notch Filter [61], which integrates the two-pole notch filter with an adaptive unit in charge of the CWI carrier frequency estimation or the Frequency Domain Adaptive Filtering [62] might be used.

7.2 Time Domain Techniques

Observation of the signal in the time domain is often useful for interference detection purposes, but is not always the best domain for applying mitigation techniques. In fact most of the interfering signals are mixed to the incoming GNSS signals, and it is not possible to act independently on the interference and on GNSS signal components. An exception are the pulsed interference signals which, in general, are limited in the time domain, but they do affect the whole frequency spectrum. For such signals the pulse blanking technique is investigated [60].

7.2.1 Pulse Blanking

The most common pulsed interference countermeasure, already implemented in modern GNSS receivers is represented by the pulse blanking circuitry. A block scheme of the digital pulse blanking implementation within the digital GNSS receiver front-end is shown in Figure 7.2. Such digital circuitry pro-

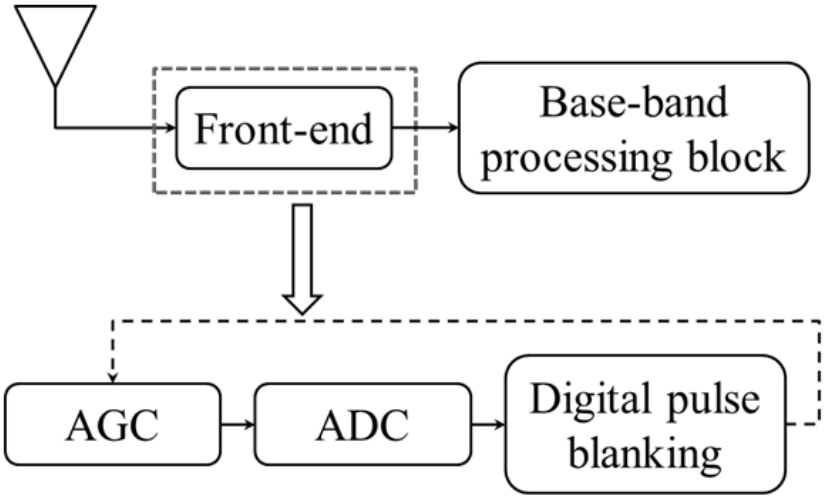

Figure 7.2: Digital pulse blanking implementation.

vides pulsed interference excision by means of a thresholding operation on the samples at the ADC output. Each sample is compared to a digital threshold

level, which is set according to an estimation of the thermal noise power only, and it is blanked whenever the threshold is exceeded.

It relies on the fact that pulses are short and have very large amplitude as compared to the noise level. Its implementation requires the presence of an ADC quantizing the incoming signal over a large number of bits. In this way, the AGC can be tuned in order to map the received signal level exploiting a limited number of bits (e.g. 2 or 3), leaving the higher bits for pulse detection purposes. Otherwise, the AGC, tuned in order to exploit the full ADC scale, would suppress considerably the useful GNSS signal during the on active state of the pulse, thus masking the presence of the pulse itself to the blanking circuitry. The detection threshold is chosen as a compromise between the ability to detect pulses and the C/N0 degradation in the absence of pulses.

The typical use of pulse blankers is in GNSS receivers designed to operate in aviation scenarios, where the interference affecting the on-board GNSS receiver is represented by the composite strong pulsed signals transmitted from all the Aeronautical Radio Navigation Systems.

7.3 Space Domain Techniques

Space domain techniques requires high complex hardware configuration exploiting antenna array. Two family of space domain techniques can be identified. First are null steering techniques which exploit the use of Controlled Radiation Pattern Array (CRPA) and second are digital beamforming techniques [63].

The use of CRPA is a very effective technique against continuous interference. This technique nulls out the signal in the direction of the interference and is capable to mitigate wide or narrow-band interference. It can be also used against pulsed interference sources like DME. CRPA technique is the reference technique in context of RF/IF analogue beam forming. The major advantage

of the analogue approach is that it can be designed to prevent saturation effects in RF/IF part of the receiver signal processing and the distortion of A/D conversion process. Its disadvantage is that all satellite signals are processed in a single RF/IF channel and can also eliminate desired signals when the directions of arrival of a GNSS satellite and interference signal coincide.

Digital beam forming is a variation of the CRPA technique where the beam forming takes place in the digital signal processing part of the receiver. The use of digital beamforming enables to process individual satellite signals in separated signal processing channels. As a result, in addition to the simple null-steering effect in the direction of arrival of the interfering signal, the digital beam forming in each channel can be optimized to the reception of a particular GNSS signal, for example by producing an additional antenna gain into the satellite direction. This digital approach is much cheaper than traditional analogue CRPA but it does not prevent front-end saturation from high power interference.

7.4 Transformed Domain Techniques

The availability of the samples of the received signals at the Analog to Digital Converter (ADC) ouput allows the investigation of a new family of detection solutions based on the use of advanced signal processing techniques. This allows the representation of the digitized signal in a different domain, where the signal distortion can be better identified, isolated, processed and in some cases mitigated. The different logical steps of the process are summarized in Figure 7.3. In the analog domain, a signal $x(t)$ can be represented in a transformed domain $X(\alpha,\beta,\gamma,...)$ exploiting a set of basis functions $h(\alpha,\beta,\gamma,...)$ such that

$$X(\alpha,\beta,\gamma,...) = \langle x(t),h(\alpha,\beta,\gamma,...)\rangle = \int_{-\infty}^{+\infty} x(t)h^*(\alpha,\beta,\gamma,...)dt \qquad (7.3)$$

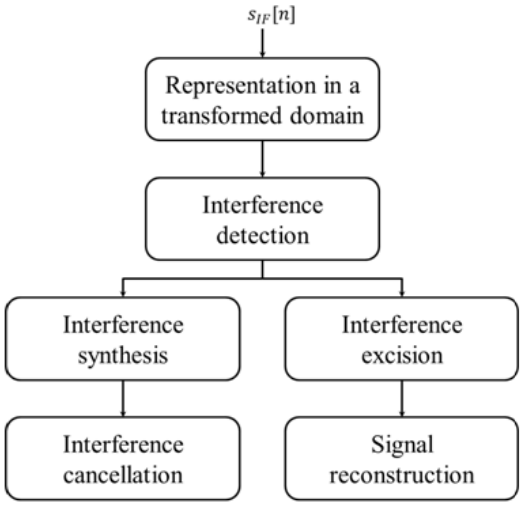

Figure 7.3: Transformed Domain technique block diagram.

$X(\alpha,\beta,\gamma,...)$ is the representation of the signal in the transformed domain, where the set of variables $(\alpha,\beta,\gamma,...)$ represents the dimension of the transformed domain.

In general the set of functions is discretized choosing discrete values of $(\alpha,\beta,\gamma,...)$ in order to obtain a set of orthonormal functions $h_k(\alpha,\beta,\gamma,...)$. The choice of the basis functions, and thus the decomposition, should allow to identify the components $X_k(\alpha,\beta,\gamma,...)$ belonging to the interfering signal thus separating them from the useful components. The signal is then represented in such a domain by $X_k(\alpha,\beta,\gamma,...)$ weighting the set of basis functions. Thus, the reconstruction of $x(t)$ can be achieved by

$$x(t) = \sum_k X_k(\alpha,\beta,\gamma,...)h_k(t,\alpha,\beta,\gamma,...) \tag{7.4}$$

The majority of the TD techniques rely on a detection algorithm based on a thresholding operation. Basically, the values of $X_k(\alpha,\beta,\gamma,...)$ are compared to a mask which represents the expected GNSS signal representation in absence of interference. From there, two options for interference suppression algorithm can be considered.

First, a synthetic reconstruction of the interfering signal by means of an anti-transformation process based on the identified interference coefficients can

be performed. Once the interference signal is reconstructed it is subtracted from the composite received signal (interference cancellation). The second approach is based on a direct suppression in the transformed domain of the interference components believed to belong to the interference, before performing an anti-transformation operation for the signal reconstruction (interference excision) [63].

It is clear that the chosen transformation must be invertible in order both to be able to generate the synthetic version of the interfering signals in case of mitigation by cancellation, as well as to reconstruct the interference-free GNSS signal in case of mitigation by excision in the transformed domain.

Due to the typical architecture of modern GNSS receivers transformation that allow efficient implementation in the digital domain, are preferable. In fact detection/mitigation units based on TD techniques could be implemented in the receiver right after the analog-to-digital conversion stage, processing the signal samples before feeding them to the acquisition and tracking stages of the receiver, as seen in Figure 7.4.

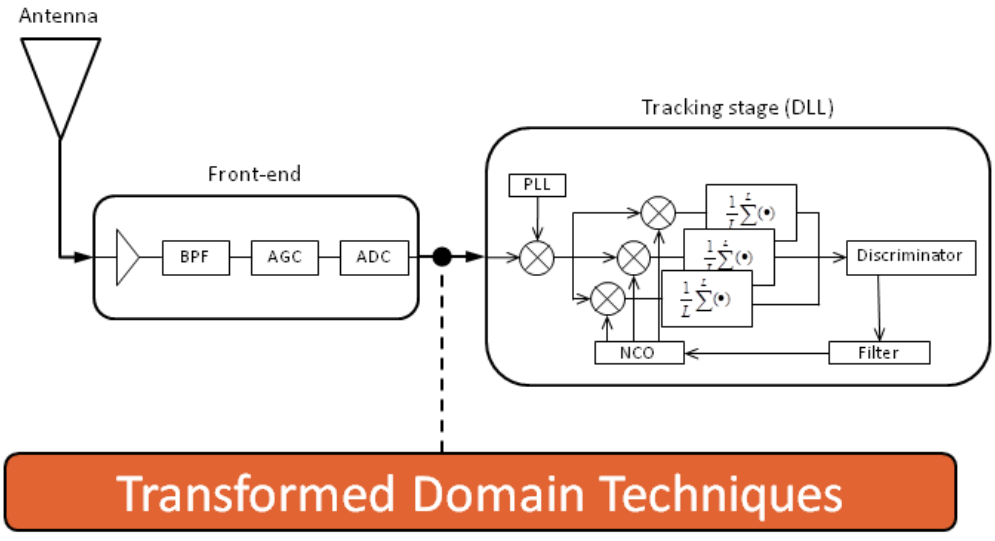

Figure 7.4: Transformed Domain technique within the receiver processing chain.

7.4.1 Wavelet Packet Decomposition

Wavelet Transform (WT) is a well know technique used in the field of signal processing for different purposes. The WT of a signal provides a representation of the signal components in a domain, spanned by a set of functions which, differently from the short-time Fourier transform, can be seen as band-pass filters with a bandwidth decreasing as their central frequency increases, thus granting a uniform resolution in the decomposition of the signal under analysis.

The basis functions employed in the wavelet transform belong to the set

$$h_k(t) = a^{-k/2} h(a^{-k} t) \tag{7.5}$$

or equivalently in the frequency domain

$$H_h(j\Omega) = ak/2 H(j a^k \Omega) \tag{7.6}$$

where $a > 1$ and $k \in \mathbb{Z}$. It can be shown that a digital implementation of the WT can be equivalently implemented by using digital filters [64]. The equivalent expression of (7.6) for digital filters would be

$$H_k(e^{j\omega}) = H(e^{j2^k\omega} \rightarrow H_k(z) = H(z^{2^k}) \tag{7.7}$$

where k is a nonnegative integer. In [65] it is shown that $H_k(z)$ is a multiband (rather than passband) filter. In order to obtain passband filters, a low pass filter $G(z)$ is employed. In [66], $G(z)$ is defined as the mirror filter of $H(z)$ and together are called quadrature mirror filters. According to a dyadic scaling operation, the nonuniform filters bank responses are obtained as follows

$$H(z), G(z)H(z^2), G(z)G(z^2)H(z^4)\ldots \tag{7.8}$$

The wavelet transform can be iterated at the higher frequency branch of the wavelet decomposition in order to obtain a uniform filter bank, performing the so-called Wavelet Packet Decomposition (WPD). Here the discrete-time signal is passed trough a uniform wavelet based filter bank. Each stage of

uniform filters is composed by a filtering process through $H(z)$ and $G(z)$, which outputs provide a set of coefficients representing a determined frequency portion of the incoming decomposed signal, as observed in Figure 7.5.

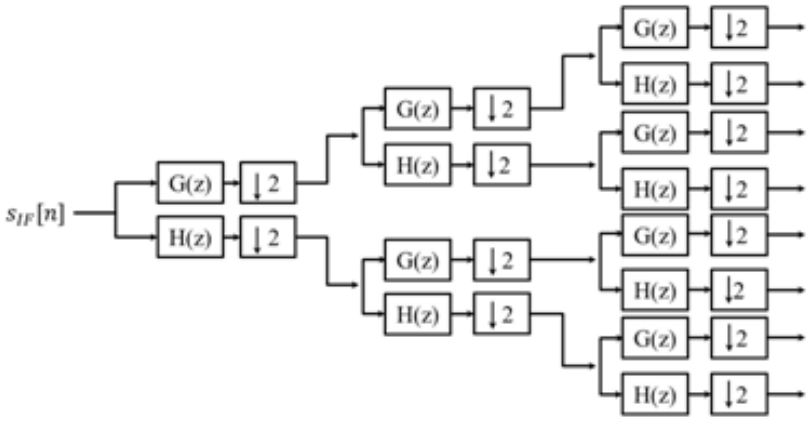

Figure 7.5: Wavelet Packet Decomposition.

7.4.2 WPD based Interference Mitigation

The algorithm for interference detection and suppression based on wavelet packet decomposition is composed of three phases [64].

- **Decomposition**, where the incoming GNSS interfered signal is passed through the uniform filter bank to achieve a time-scale representation.
- **Detection-Mitigation**, performed in each scale obtained at the output of the filters bank. The interference excision is performed based on the suppression of the coefficients in each scale crossing a determined blanking threshold level.
- **Reconstruction**, achieved through an inverse wavelet transform from the modified scales after the interference coefficients suppression.

As an example Figure 7.6 shows the comparison of time-scale representation of GPS C/A signal with and without the presence of interference, in this

example a Narrow-band interference. It is observed how the time-scale floor, after 4 stages of WPD, shows the narrow-band interference components. The fact that those are located in determined scales clearly above the noise floor time-scale eases the detection process. Once the excision is performed, the

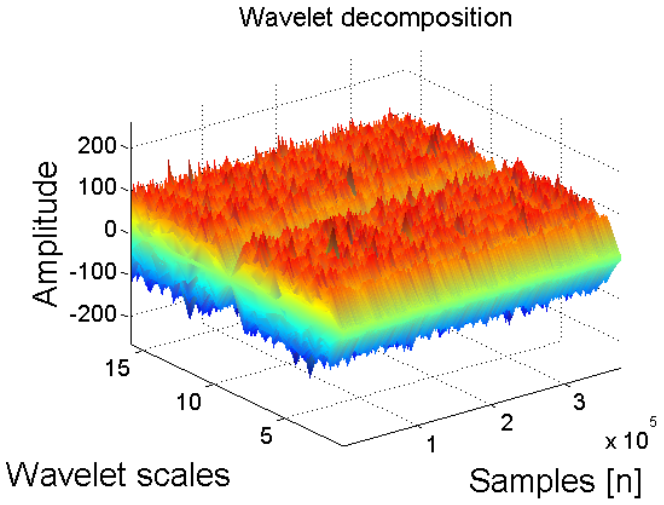

(a) No interference case

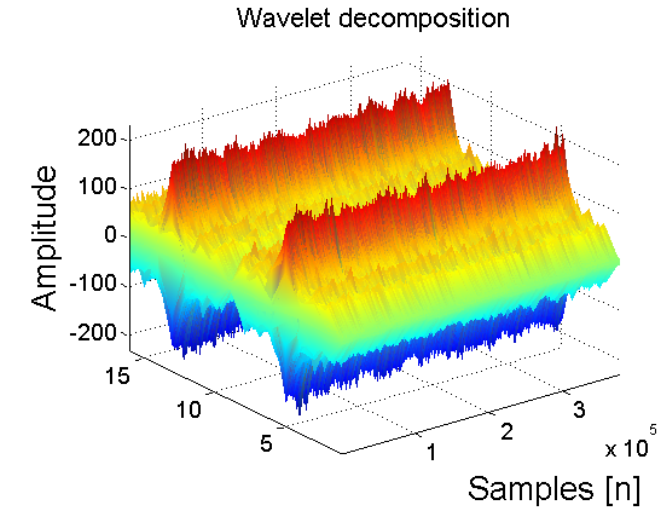

(b) Interference case

Figure 7.6: Wavelet Decomposition.

signal is reconstructed in time domain through the inverse wavelet transform. Figure 7.7(a) and Figure 7.7(b) show, respectively, comparisons of time and frequency domains of the signal before and after the mitigation was performed.

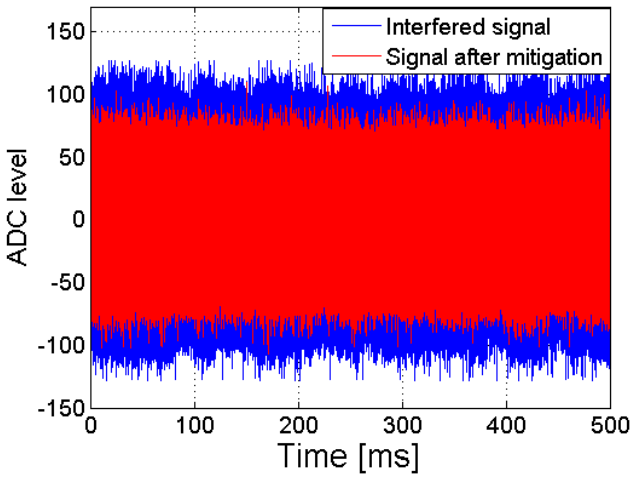

(a) Time domain reconstruction

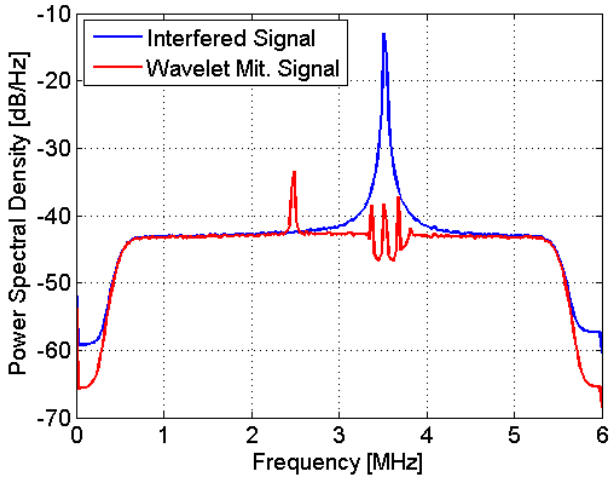

(b) Spectra

Figure 7.7: Wavelet mitigation.

7.5 Interference Mitigation in a Scintillation Scenario

As observed in Chapter 6 GNSS Scintillation Monitoring is susceptible to errors in the presence of interference. It was shown that spurious signals such as continuous wave and wideband interferences can mislead the estimation of scintillation activity. It is then of interest to analyse if by applying interference mitigation techniques such as the ones summarized in this chapter, it could

still be possible to retrieve the original scintillation information that was embedded in the signal.

To this effect, we will perform our analysis with two of the techniques previously presented: The Notch filtering and the Wavelet Packet Decomposition techniques. This operation could proved useful for scintillation monitoring even in challenging scenarios where interference is present.

Similar to the scenarios presented in Section 6.2, we will compare our interference/scintillating scenarios against reference scenarios where only scintillation is affecting the signal.

7.5.1 Notch filter study case

Notch filter is an efficient mitigation algorithm for pure sinusoids family of interfering signals, such as the continuous wave interference. It can provide attenuation of the interfering signal while preserving as much as possible the useful GNSS signal spectral components. Figure 7.8 presents an example of severe CWI interference on a scintillating satellite. The CWI signal has the following characteristics: $f_{offset} = 25KHz$, $Power = -125dB$. The incoming scintillating signals is affected by a strong scintillation fluctuations, as observed from the S4 index reference values. As it was presented through our examples in Section 6.2, this represents a worse case scenario where the combined high power level and frequency vicinity to the GNSS carrier of the interference combined with high levels of scintillation cause a complete loss of tracking of the GNSS signal in the receiver.

Assuming a correct detection of the interference signal, notch filtering was applied to the signal samples at the output of the ADC. Figure 7.9 shows a comparison of the spectra before and after the filtering was applied. In this case, the filter was able to correctly suppress the interference power while preserving the GNSS signal. Once the interference has been suppressed, the mitigated signal can be tracked without the receiver losing lock thus,

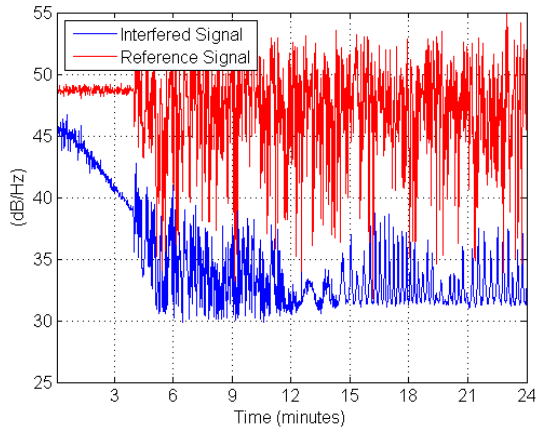

(a) C/N_0

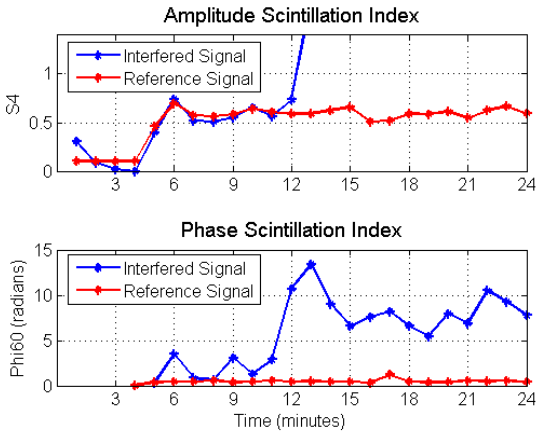

(b) Scintillation indices

Figure 7.8: CWI in a strongly scintillating scenario (1).

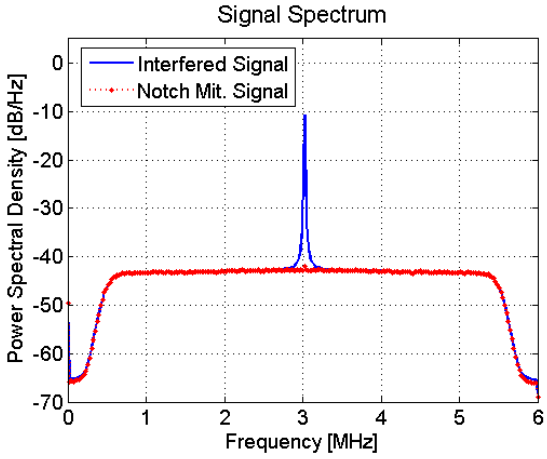

Figure 7.9: Notch filter interference mitigation

scintillation information is correctly estimated. Figure 7.10 shows the signal C/N_0 and scintillation indices after the notch filtering.

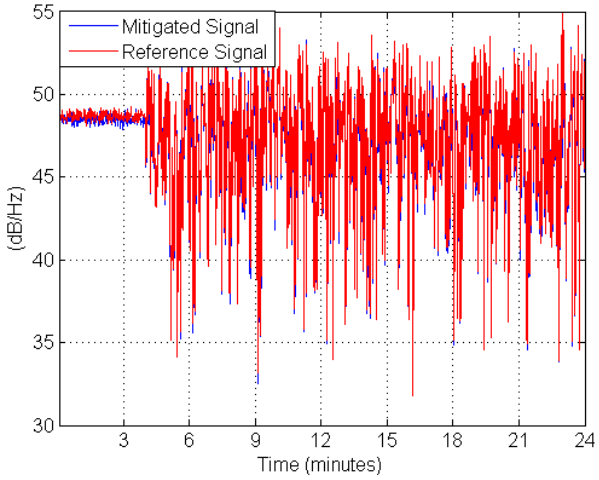

(a) C/N_0

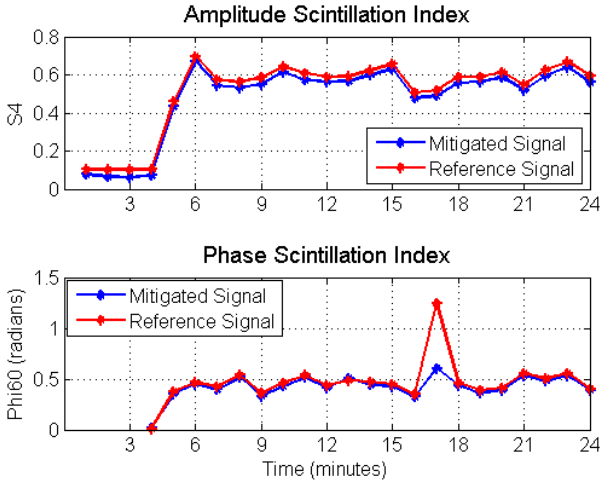

(b) Scintillation indices

Figure 7.10: Notch filtered mitigated signal

7.5.2 Wavelet decomposition study case

A similar test was performed with the Wavelet decomposition technique. Figure 7.11 shows another example of GNSS signal affect by a continuous wave interference. The CWI signal has the following characteristics:

$f_{offset} = 525KHz$, $Power = -125dB$. The level of scintillation was kept at high levels as evidenced in the reference measurements. In this case the signal had not loss lock due to the effect of interference given that is 500KHz apart from the carrier, where in the previous example was at 25KHz. However the interference induced distortions were enough for the phase index to show a wrong value at minute 10.

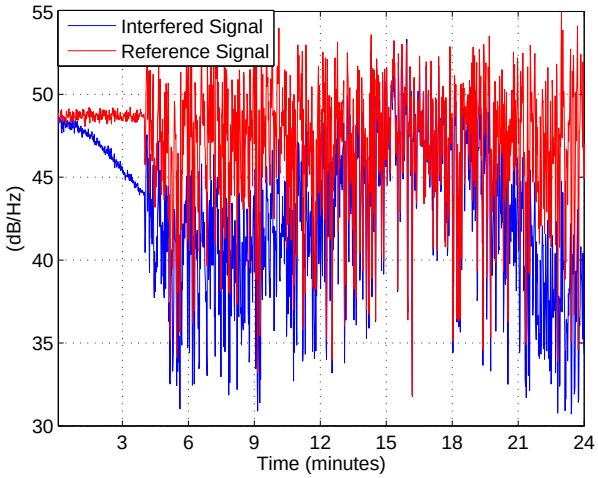

(a) C/N_0

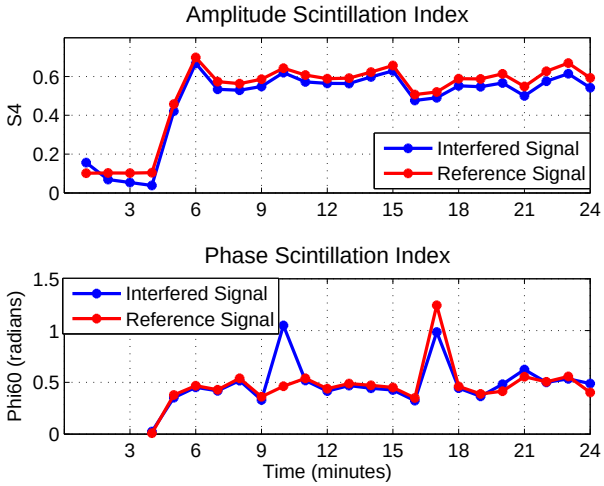

(b) Scintillation indices

Figure 7.11: CWI in a strongly scintillating scenario (2).

The interfered GNSS signals is decomposed by means of the transform in order to detect the interference components, suppress them and reconstruct back

the scintillating GNSS signal without the foreign signal elements. Figure 7.12 shows the recalculated C/N_0 and scintillation indices after the wavelet based interference mitigation was applied to the input signal. As seen in the figure,

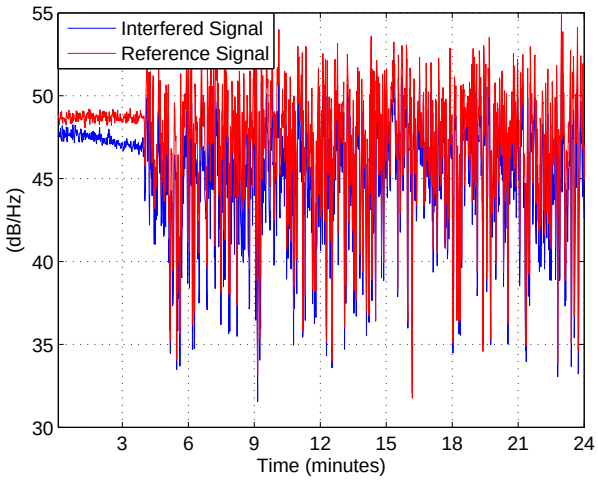

(a) C/N_0

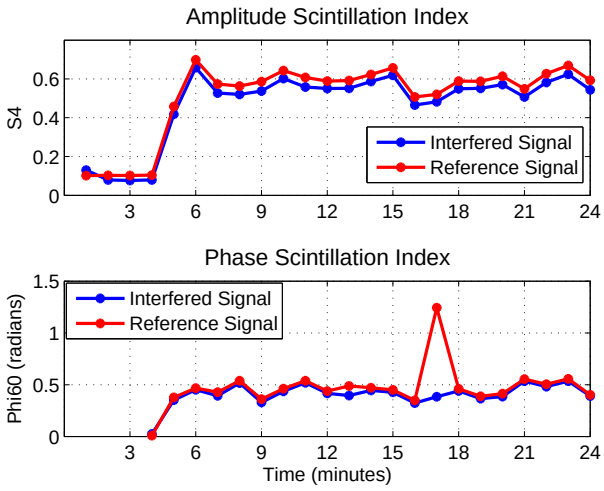

(b) Scintillation indices

Figure 7.12: Wavelet packet mitigated signal.

the technique works well to suppress the foreign signal while preserving the scintillation features in the GNSS signal.

7.5.3 A Comparative case

The effectiveness of the interference mitigation techniques depends on the chosen technique being the best match to suppress the type of interference affecting the signal. As mentioned in Section 7.1 , for example, frequency domain techniques are weak against pulsed interference given that the interfering signal would only be present for a limited time.

The notch filter is the best technique to suppress the interferer given the very narrow portion of rejection spectrum. In the previous example were CWI is affecting the signal, though being a critical case being the interference signal power very high and its frequency very close to the carrier ($f_{offset} = 25KHz$, $Power = -125dB$), it was shown that by applying such mitigation technique it was possible to completely clean the signal of the interference. Following example analyses the same interference critical case but applying this time the wavelet decomposition mitigation. Figure 7.13 shows the spectra of the notch filter mitigated case against the wavelet decomposition mitigated.

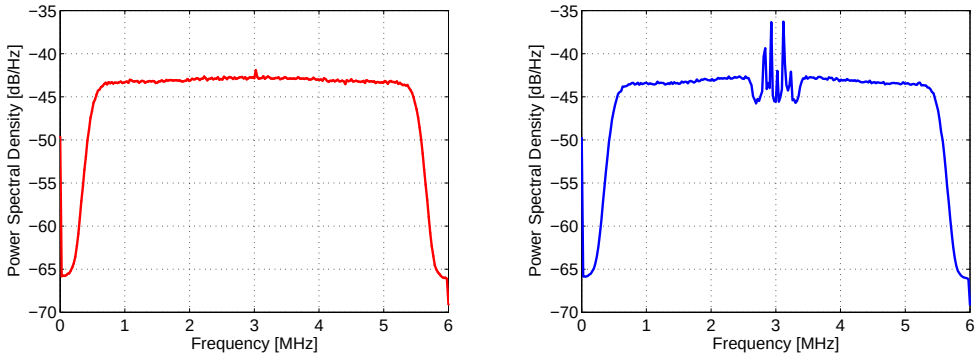

(a) Notch Filter (b) Wavelet Filer

Figure 7.13: Spectra of mitigated signal.

As observed in Figure 7.13, the wavelet filtering technique can not be as narrow as the notch filter even when increasing the filtering stages. As a consequence, a part of the useful signal spectra is suppressed as well when applying the technique. In the present example this is of grave consequences

given that the interference was at the center of the main lobe, thus the mitigation technique has suppressed part of the most vital spectrum section of the useful signal. As a consequence, the satellites signals cannot be tracked by the receiver after the mitigation was applied, as observer in Figure 7.14

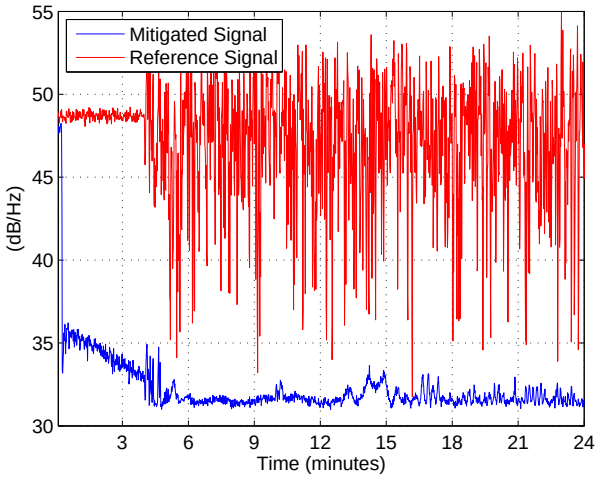

(a) C/N_0

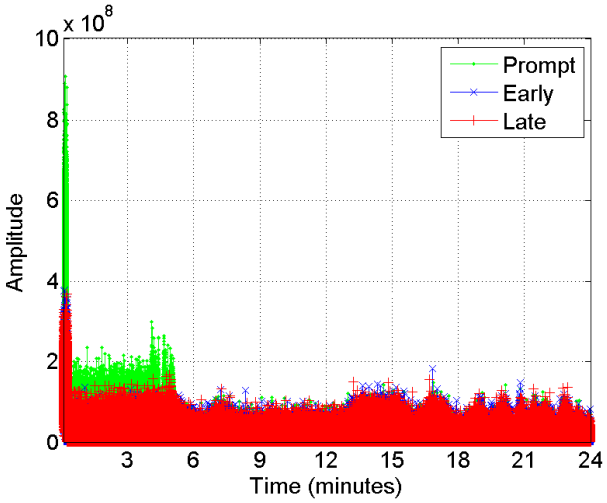

(b) Tracking correlators

Figure 7.14: Receiver outputs.

7.6 Summary

This Chapter introduced the most common digital signal processing techniques for interference mitigation in GNSS receivers, covering the main strategies devised in the frequency, time, and space domains. As interference signals have many different features, no single mitigation technique works against all kinds of interference and the best choice for mitigation is always based upon characteristics of the interference signal itself.

A particularly challenging scenario was presented where not only interference is affecting the signal but also ionospheric scintillation induced perturbations are present. In such scenario, mitigation techniques have proven useful to suppress the spurious signal while making possible to retrieve the features belonging to scintillation. However, for this to be possible the appropriate mitigation technique according to the incoming interference characteristics must be chosen, as was the case with the notch filtering and wavelet based mitigation techniques in the analysed case of continuous wave interference.

Chapter 8

Training Research and Applications Network to Support the Mitigation of Ionospheric Threats

This last chapter gives a short summary of the Training Research and Application Network to Support the Mitigation of Ionospheric Threats, TRANSMIT project, that funded the research of this thesis.

TRANSMIT project was a Marie Curie Initial Training Network (ITN) funded by the European Commission. The final goal of the project was to develop integrated state of the art tools to mitigate ionospheric threats to Global Navigation Satellite Systems (GNSS) and several applications that rely on these systems. In particular, Scientific and Industrial Applications Reliant on GNSS was the TRANSMIT sub-project dedicated to the assessment of ionospheric effects on GNSS and related applications and aimed to develop countermeasures to mitigate them at receiver level. In this context, a tool was been designed and implemented with the purpose to process

both GPS and GALILEO signals using different receiver tracking architectures/configurations and providing scintillation monitoring capabilities

8.1 TRANSMIT PROJECT

Ionospheric effects are especially concerning for GNSS users and service providers demanding high reliability, availability and accuracy of positioning and navigation.

At a COST 296 MIERS (Mitigation of Ionospheric Effects on Radio Systems) workshop held in 2008, the establishment of a sophisticated Ionospheric Perturbation Detection and Monitoring (IPDM) network [67] was proposed and supported by the European Space Agency (ESA) as the way forward to deliver the state of the art to protect the range of essential systems vulnerable to ionospheric threats.

In a bid to initiate research and training of scientists in Europe for the development of the IPDM network, the Training Research and Applications Network to Support the Mitigation of Ionospheric Threats (TRANSMIT) project (www.transmit-ionopshere.net) was proposed. It was funded by the European Commission through their FP7 PEOPLE Programme in the form of a Marie Curie Initial Training Network (ITN). TRANSMIT focused on the mitigation of space weather events which can affect the operation of several systems and applications playing a strategic role in the modern society. In fact GNSS satellite signals and any other system operating below 10 GHz, such as remote sensing and Earth observation systems, are extremely vulnerable to space weather events. Consequently, the latter may have significant safety and economic consequences.

The final aim of the TRANSMIT project was to set up a prototype of the proposed IPDM network and related service. This task implied the achievement of different objectives steered by both science and industrial requirements.

They included the development of new techniques to detect and monitor ionospheric threats, as well as the enhancement of existing physical models of the underlying processes associated with the ionospheric plasma.

As seen in Chapter 3, GPS signals are currently one of the preferred sources to measure ionospheric scintillations given the fact that they have been continuously available in a global basis for many years. With the deployment of the European GNSS Galileo, which is to be fully compatible and interoperable with GPS (i.e. sharing the same carriers for some services), there will be a noticeable increase in the number of available satellites that allow us sampling the ionosphere while taking advantage of the infrastructures (equipment and algorithms) already existing for data collection with GPS L1 C/A. However, as introduced in Chapter 5 and Chapter 6, with the increasing number of telecommunications system operating at frequency bands close to GNSS signals the effectiveness of scintillation monitoring could be impaired by the presence of Radio Frequency Interference (RFI) in the operational area. Robust tracking of GNSS signals under such conditions must be guaranteed and it must also be ensured as best as possible that the typical scintillation indices are not affected by additional error sources.

Following sections provide a general overview of the TRANSMIT prototype. Later on it is described in detail a software tool aimed to design a robust scintillation receiver architecture through the development of advanced tracking schemes while, at the same time, taking into account the presence of radio frequency interference as an additional error source that may impair scintillation monitoring for both GPS and Galileo. The processor has been designed to cope with different scenarios, including scintillation and other types of interference. The specific scenario of interest can be determined by a generic user through the selection of input parameters detailed later on in the chapter. Once the scenario is defined, the processor can provide the related outputs defining the performance of the receiver tracking scheme and characterizing the scintillation level.

8.2 The TRANSMIT Prototype

The TRANSMIT prototype is a web-based demonstrator consisting of three tools, called processors, addressing six applications [68]. TRANSMIT processors are designed to be able to exchange their outcomes and use them as inputs to other related applications via the prototype network. The design of data flow in the prototype system is characterized as a cross-institutional network approach. The main concept of the prototype network is to clearly divide the functions of the partner institutions.

The user/demonstration portal, data archive and processor applications are hosted by different institutions distributed over Europe. The data flow design in the TRANSMIT prototype service is shown in Figure 8.1. The demonstration portal, denoted as Institution C, receives queries sent by the users. The user queries can be parameter input or selection of particular ionospheric event that will be used in the processor applications.

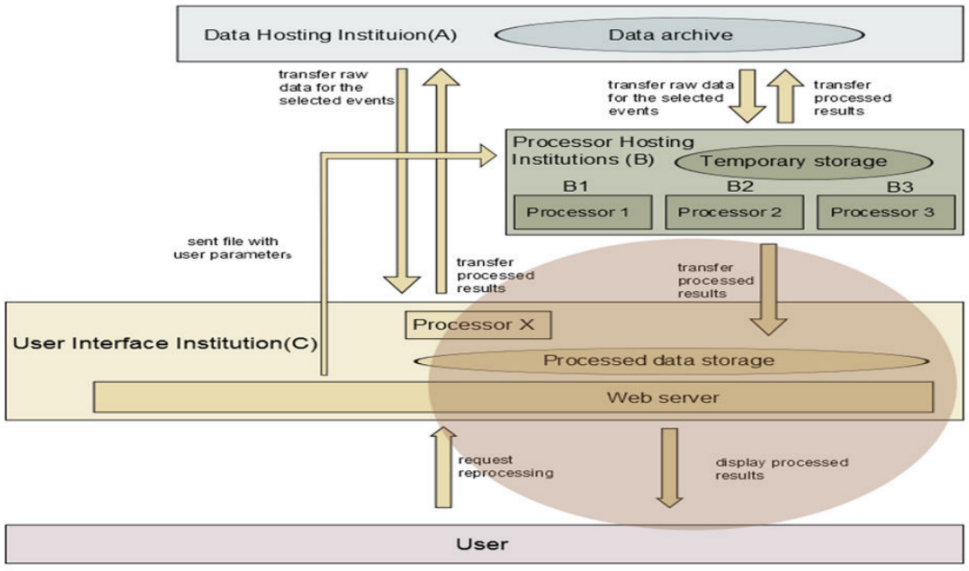

Figure 8.1: Schematic diagram of TRANSMIT prototype network and modeled data flow.

Once the users define parameters and store them in the portal, those parameters are forwarded directly to the processor hosting institutions denoted as B. The processors parse the parameters and determine whether to computes locally or request the necessary data from the data archive hosting institute A.

The computation time can vary from less than one minute to a few hours depending on the processor. When a user selects a quick processing application, the results can be displayed on the prototype portal directly after the task is completed. Processors with longer processing time implement an email notification function.

- **Processor 1: Scintillation index prediction by Spline model**: This processor aimed to develop an $S4$ index and TEC value prediction model over the European high and middle latitude regions. The advantage of this modelling is to combine the ground based measurements with in-situ (directly observed) plasma parameters by spacecraft orbiting over the concerned region.

- **Processor 2: Improved tracking architecture and positioning error mitigation**: This processor investigated and mitigated the effects of ionospheric disturbances at receiver and positioning level. The focus was on the following research topics: analysis of the effect of mitigation techniques on the accuracy of positioning applications and the design of a robust receiver architecture able to cope with different scintillation and radio frequency interference scenarios.

- **Processor 3: Ionospheric models and applications**: The purpose of this processor was to provide a new insight on existing ionospheric models. A new TEC prediction model was developed by means of a data assimilation technique. It performed a comparative study of the developed model against the most widely used models. As an application

of the modeling approach, it demonstrated the error caused by the assumption residing in a common modeling method in Radio Occultation remote sensing for ionospheric research.

8.3 Scientific and Industrial Applications Reliant on GNSS (Processor overview)

The research work described in this chapter was part of a specific TRANSMIT sub-project titled Scientific and Industrial Applications Reliant on GNSS. The latter was dedicated to the assessment of ionospheric effects on GNSS and related applications and was steered by industrial requirements. The scope of this sub-project, within processor 2, was to quantify the effect of ionospheric scintillation and mitigate it at different receiver stages from the tracking to the positioning level. However, the particular tool here described does not deal with the positioning stage but focuses on the tracking stage. In particular, on the techniques to render this receiver link more robust when scintillation and also other types of external errors such as interference from other telecommunication systems are present.

The processor was developed with the collaboration of TRANSMIT researchers from University of Nottingham and University of Nova Gorica.

8.3.1 Processor Overview

Here is described the design and implementation of a software based tool, a processor, implemented to accomplish the following main tasks:

- Scintillation monitoring. This is performed by computing the scintillation indices S4 and Phi60 which quantify, respectively, the level of amplitude and phase scintillation.

- Robust tracking under scintillation. The processor includes three different tracking schemes, namely a traditional Phase Locked Loop (PLL) with fixed bandwidth and two types of adaptive Kalman Filter based PLLs, namely a conventional adaptive KF (AKF) PLL and a scintillation based KF (SAKF) PLL exploiting the knowledge about the scintillation level to tune its covariance matrix.

- Interference mitigation. This task is fulfilled in order to remove any RFI that could potentially affect the scintillation indices computation and decrease the tracking performance.

Furthermore, the processor, whose general scheme is reported in Figure 8.2, had been designed to be tested under different scenarios defined by the characteristics of the input signal. Three different scenarios can be selected based on scintillation levels affecting the signal (low, medium, high) or, alternatively, a scenario where the signal is free of scintillation. The selected signal could either be fed to the receiver or being contaminated before by radio frequency interference. Two type of interference scenarios have been selected, i.e. continuous wave and wideband noise. Similarly to the scintillation case, three different levels (low, medium, high) of the interfered signal have been defined based on its power with respect to the GNSS signal itself.

Once the signal scenario of interest has been defined, the notch filter or wavelet mitigation algorithm can be activated to cope with the simulated interference, if it is present. The signal will then be processed by a software based receiver from which the three mentioned tracking architectures can be chosen.

According to the selected tracking architecture further parameters can be set. They are the loop bandwidth for the conventional PLL and the integration time for any of the three tracking schemes. Finally, when the signal and the receiver architecture have been defined, the processor will provide the scintillation indices and some parameters useful to assess and compare the

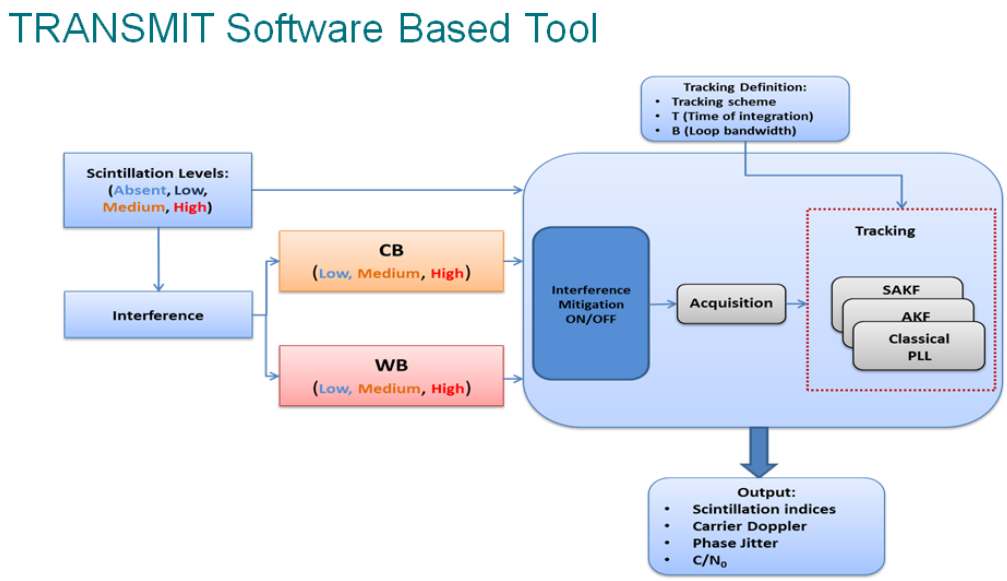

Figure 8.2: General overview of the processor.

performance of the implemented tracking schemes. Specifically, the following outputs are given:

- S4, namely the level of amplitude variation and the corrected version of the parameter.
- Phi 60, indicating the scintillation phase variation.
- C/N0 which is the signal to noise ratio and can be used to monitor the signal quality.
- Phase Jitter which is the standard deviation of the discriminator output.
- Phase Lock Indicator (PLI), a metric to evaluate the performance of the PLL.

8.3.2 Carrier Tracking Architecture

A receiver robust under scintillation should be able to track weak signals produced by amplitude scintillation and fast dynamics due to phase scintillation.

These scintillation effects can be particularly challenging for the PLL of a GNSS receiver. Conventional PLL tracking schemes require a smart selection of loop parameters in order to cope with scintillation events. Narrow bandwidth values, or long periods of integration, should be preferred in presence of signal fading while wider bandwidth, or short integration periods, should be selected in presence of fast dynamics. This trade-off represents the main limitation of a conventional PLL algorithm which is based on a priori fixed loop parameters.

To overcome this problem, alternative tracking schemes are proposed in the literature in order to deal with challenging scenarios. An extensive overview of carrier tracking techniques robust under harsh scenarios can be found in [69]. A possible approach to cope with scintillation is to combine the PLL with a FLL in order to exploit the advantages of both tracking schemes. In fact a FLL is less accurate than a PLL but it is also less sensitive to high dynamics and weak signals.

Consequently the FLL can be used as backup solution when the PLL experiences a loss of lock [70]. Alternatively, FLL assisted PLL techniques can be employed. They are based on the simultaneous estimation of the frequency and phase errors which are then combined to drive the numeric controlled oscillator [71]. In order to cope with scintillation effects, another possible strategy consists in using adaptive PLL schemes which select the optimum loop parameters on the basis of a specific performance metric [72].

Among the adaptive techniques, the KF based PLL schemes are particularly suitable in challenging conditions as the ones produced by scintillation. In fact KF provide the optimum coefficient loop filters able to minimize the mean square error between the input signal and the replica generated by the numerical controlled oscillator NCO [73]. However the optimality of the KF is conditioned by specific assumptions. First of all, the additive noise should be white and Gaussian, then the process noise covariance and the measurement noise should be a priori known. In fact, wrong a priori statistic could lead

to sub-optimum solutions or, in the worst case, to non-stationary systems inducing a divergence of the filter.

This is a sensitive aspect in case of scintillation scenarios where the signal propagation conditions can suddenly change. For this reason, in highly variable scenarios, adaptive KF schemes should be preferred. For example, the signal quality, monitored through C/N_0 and the scintillation spectral parameters could be exploited to adapt the noise covariance and the measurement noise statistics. This approach is used in the mentioned SAKF PLL which exploits the slope of the phase power spectral density (PSD) and the spectral strength of the phase noise at 1 Hz to self-tune its covariance matrix. Furthermore, this PLL scheme uses C/N_0 to adapt the measurement noise. The details about the design and the implementation of the above PLL algorithm can be found in [74].

The latter tracking scheme, a classical adaptive KF (AKF), also detailed in [74] and, a conventional third order PLL has been implemented into the processor. The conventional PLL exploits fixed bandwidth and time of integration. As sample case the tracking of a GPS L1C/A signal affected by moderate-severe scintillation has been analyzed in order to show the tracking capabilities of the processor. The three tracking schemes included into the processor with time of integration $T_s = 1ms$ have been exploited to post-process the data. Furthermore, for the conventional PLL a bandwidth $Bw = 15Hz$ has been selected.

A comparison of the carrier Doppler for the three tracking schemes is reported in Figure 8.3(a). The KF PLLs allows a reduction of the noise with the SAKF PLL achieving the best results. Similarly, a comparison of the phase jitter for the three tracking schemes can be seen in Figure 8.3(b). The phase jitter is obtained by evaluating the standard deviation of the discriminator output over one minute.

Again the KF PLLs, and in particular the SAKF PLL, allow obtaining the

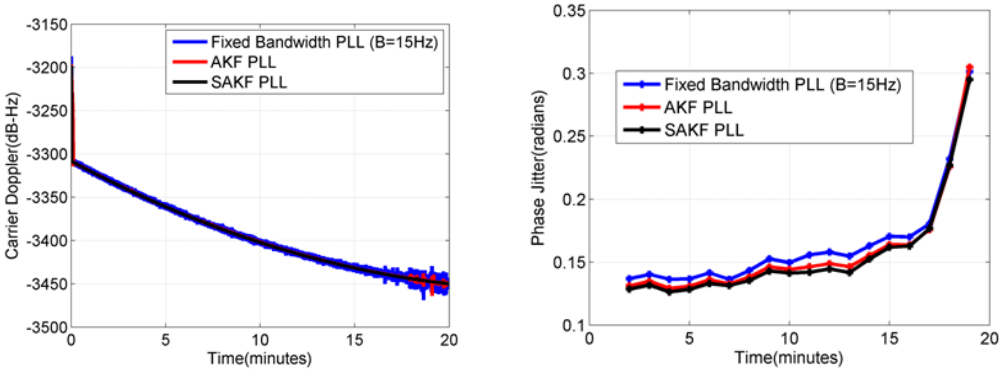

(a) Carrier doppler (b) Phase jitter

Figure 8.3: Tracking architectures comparison.

lower phase jitter values and consequently, the higher performance. Apart from tracking robustness, another important feature of a scintillation monitoring receiver is given by the capability of interference mitigation. For this reason the processor includes a stage to remove interference through notch filtering and wavelet based mitigation methods.

8.3.3 A user interface for the proposed tool

In order to provide a user friendly interface to select the different scenarios and receiver architectures characterizing the processor, a Graphical User Interface (GUI) has been developed. The latter, shown in Figure 8.4, allows selecting different data sets fixed a priori and corresponding to the cases where only scintillation or scintillation plus interference are present. The user can select the scenario of interest by checking the related field and defining the associated level of scintillation/RFI as defined in Section 8.3.1. For the interference case also the power level can be specified. If no fields are checked in the Inputs section, a default scenario, free of scintillation and RFI interference, will be used. Then, by clicking on the option Click to set Rx Parameters the receiver architecture can be defined in order to process the data. Specifically, the receiver architecture definition consists in the selection of one of

the three carrier tracking architectures and in the activation/deactivation of the interference mitigation block, as described in Section 8.3.2, according to the presence/absence of interference.

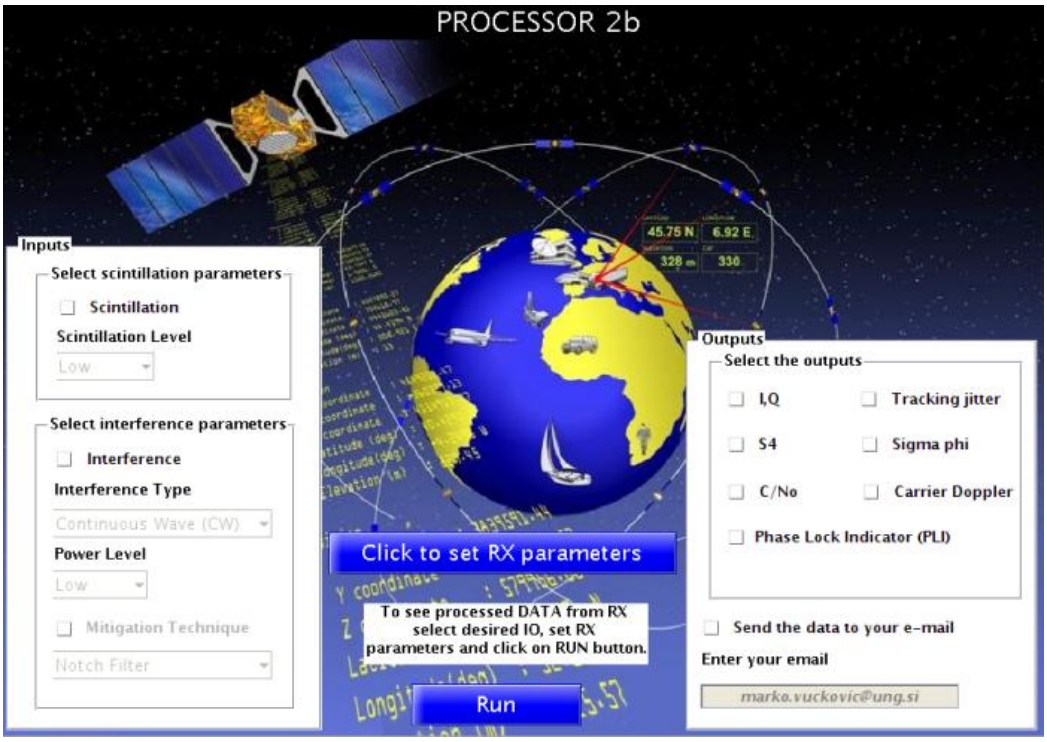

Figure 8.4: Graphical user interface.

Finally, by checking the fields of interest in the Outputs section, the parameters of interest can be visualized. Specifically, a number of parameters are available. They are the prompt correlator output (I and Q), the scintillation indices (S4 and Phi60), and some metrics (phase jitter, carrier doppler, phase lock indicator) to evaluate the carrier tracking performance of the selected PLL scheme under the considered scenario.

8.4 Summary

This chapter presented the TRANSMIT processor designed to provide a GPS and GALILEO receiver architecture robust to scintillation. The latter has been implemented to be flexible and to allow processing of GPS and

GALILEO signals using three different tracking architectures: a traditional third order PLL, a classical adaptive KF PLL and a scintillation based adaptive KF PLL. This tool allows to compare the performance of these algorithms under a number of scenarios including different levels of scintillation. The growing threat of interference in GNSS systems has also been taken into account and its integration into the prototype will allow not only the analysis that power leaks from other telecommunication systems may have in scintillation monitoring, but also the possibility to retrieve the true scintillation information once the interference effect have been suppressed. Future test will continue in order to improve the algorithms and tune them to the scenarios most relevant in the context of scintillation monitoring.

Chapter 9

Final Conclusions and Future Activities

This chapter discusses main results and achievements obtained during the thesis. Topics of interest for future research activities, arising from the research carried out in this work, are also mentioned.

9.0.1 Summary of Contributions

The main objective of this research work has been to explore within the field of GNSS, the incidence that external errors such as interference can have over the ionospheric scintillation monitoring activities. The main contributions can be summarized in two main parts encompassing several aspects of the research performed.

Ionospheric Scintillation Monitoring: In this part we have studied the most relevant processes in the ionosphere that generate scintillations in transionospheric signals. Our work has not only covered the effects that scintillating signals have over GNSS receivers, but also how to take advantage of the receiver itself to estimate the amount of ionospheric scintillation activity. Relevant models dealing with scintillation effects on GNSS were also detailed,

in particular, we made use of the Cornell scintillation model in order to test our receiver algorithms under controlled scenarios.

All the previous points were successfully brought together in order to run a campaign of scintillation data collection, in an equatorial region, in collaboration with several partners. We have summarized in detail software and hardware considerations to take into account in order to successfully estimate amplitude and phase scintillation activities from real data collections. Our findings have been summarized in this thesis, hoping that it can be useful to those looking to set up similar scintillation data collection campaigns at lower cost with respect to professional solutions in the market.

Interference Effect in Scintillation Monitoring: Second important part of the thesis have dealt with the effect interference can have over scintillation monitoring activity. In the literature we found indications regarding external errors, such as multipath and interference, as factors that may impair scintillation indices computation but no description or characterisation of such effects is given. In this thesis we took to the task of investigating the effects of interference. As there are many interference signals that might be encountered in GNSS environments, our studies focused on the most commonly found types. Upon investigation of their effect, continuous wave interference surfaced as one that is particular harmful given its particular effects on the receiver, inducing the biggest errors over the scintillation activity estimation with GNSS receivers.

We have then shown a sample of analysed study cases based on different levels of scintillation activity and of different characteristics of the interference itself, such as its power and frequency offset with respect to the GNSS carrier. Our results show that amplitude scintillation measurements are more prone to errors when the actual scintillation level in the GNSS signal is low, given that interference induced fluctuations in amplitude erroneously trigger S4 index if the interference effect is severe. When scintillation levels in the GNSS signal are at an intermediate or strong level, we have found that is very difficult for

an interference to induce fluctuations that in average overpass those originated from scintillations. In these cases the S4 might show slight but not dramatic changes. Phase scintillations in particular, are susceptible to errors in the presence of interference. The tracking PLL is the weakest link in the receiver and the block in charge of performing phase measurements, same ones that will be used to calculate the scintillation index Phi60. As interference induces the PLL into errors, Phi60 measurements become unreliable and should not be trusted. These scenarios were performed over GPS L1 C/A signal, the most widely used for scintillation monitoring. Given that Galileo E1 band has been designed to be interoperable with GPS C/A signal, the civil signal in E1 have also been analysed and interesting results were found in comparison with GPS. Due to the spectral characteristics of E1, it is more resilient to the worst effects of the continuous wave and thus can keep better track of the signal in a challenging scintillating plus interference scenario. However, its longer code also makes it more vulnerable to the particular continuous wave interference induced errors, showing more disruptions in the estimation of the scintillating activity when interference is present.

Our analysis also included the study of interference mitigation techniques. Among the different kind of methods, we chose notch filtering and a novel wavelet based mitigation techniques as study cases. Both of these techniques are suitable to suppress continuous wave interference, the one we performed most of the analysis with, in our experiments. Interference mitigation techniques have shown that is possible to retrieve the original scintillation activity in our tests with continuous wave . But as different types of interferences have also varying effects on GNSS receivers, it still an open point that could be investigated further with other types of interference an suitable mitigation techniques according to their characteristics.

9.0.2 Future Work

Scintillation monitoring is a growing scientific activity at the moment. There is the need to collect more information on ionospheric activity that could help future models to forecast the occurrence of scintillations. Trough the experience we have acquired by now in collecting, processing and estimating scintillation activity from GNSS signals with the help of software receivers, we are now involved in several projects to continue monitoring and analysing scintillation activity over both equatorial and polar regions.

Receiver related research can also be unlocked through the study of scintillation phenomena. A hot topic research is to improve the robustness of the GNSS receiver against scintillations. Advanced tracking techniques such as vector tracking might be analysed in the future in the context of scintillation environments.

Bibliography

[1] E.D. Kaplan and C.J. Hegarty. *Understanding GPS Principles and Applications*. Artech House, 2nd edition edition, 2006.

[2] P. Misra and P. Enge. *Global Positioning System: Signals, Measurements, and Performance* . Ganga-Jamuna Press, second edition, 2006.

[3] Kung Chie Yeh and Chao-Han Liu. Radio wave scintillations in the ionosphere. *Proceedings of the IEEE*, 70(4):324–360, 1982.

[4] National Research Council. *Severe Space Weather Events - Understanding Societal and Economic Impacts: A Workshop Report*. The National Academies Press, 2008.

[5] A.J. Van Dierendonck and Q.H. Klobuchar. Ionospheric Scintillation Monitoring Using Commercial Single Frequency C/A Code Receivers. In *Proc. ION GPS*, pages 1333–1342, 1993.

[6] T.L. Beach and P.M. Kintner. Development and use of a GPS ionospheric scintillation monitor. *Geoscience and Remote Sensing, IEEE Transactions on*, 39(5):918,928, May 2001.

[7] A.J. Van Dierendonck and B. Arbesser-Rastburg. Measuring Ionospheric Scintillation in the Equatorial Region Over Africa, Including Measurements From SBAS Geostationary Satellite Signals. In *Proceedings of the 17th International Technical Meeting of the Satellite Division of The Institute of Navigation (ION GNSS)*, 2004.

[8] B. Bougard, J.M. Sleewaegen, L. Spogli, S.V. Veettil, and J.F Galera. CIGALA: Challenging the Solar Maximum in Brazil with PolaRxS. In

Proceedings of the 24th International Technical Meeting of The Satellite Division of the Institute of Navigation (ION GNSS 2011), pages 2572,2579, September 2011.

[9] B. Motella, M. Pini, and F. Dovis. Investigation on the Effect of Strong Out-of-Band Signals on Global Navigation Satellite Systems Receivers. *GPS Solutions*, 12:77–86, 2008.

[10] B.W. Parkinson and J.J. Spilker. *Global Positioning System: Theory and Applications*, volume I. American Institute of Aeronautics and Astronautics, 1996.

[11] ESA. Navipedia: The reference for Global Navigation Satellite Systems. Retrieved on 21/01/2015 from http://www.navipedia.net/index.php/MainPage.

[12] GSA. Galileo Services. Retrieved on 09/03/2015 from http://www.gsa.europa.eu/galileo/services.

[13] J.-A. Avila-Rodriguez, G.W. Hein, S. Wallner, and J.-L Issler. The MBOC Modulation: The Final Touch to the Galileo Frequency and Signal Plan. In *Proceedings of the International Technical Meeting of the Institute of Navigation, ION-GNSS*, September 2006.

[14] L. Scott, A. Jovancevic, and S. Ganguly. Rapid signal acquisition techniques for civilian and military user equipment using DSP based FFT processing. In *Proceedings of 14th International Technical Meeting of the Satellite Division of the Institute of Navigation*, 2001.

[15] C. Ma, G. Lachapelle, and M.E. Cannon. Implementation of a software gps receiver . In *Proceedings of the 17th International Technical Meeting of the Satellite Division of the Institute of Navigation (ION GNSS 2004)*, pages 956–970, September 2004.

[16] I.G. Petrovski and T. Tsujii. *Digital Satellite Navigation and Geophysiscs*. Cambridge University Press, 2012.

[17] R.B. Langley. GPS, the Ionosphere, and the Solar Maximum. *GPS World*, 11:44, 2000.

[18] S. Bassiri and G.A. Hajj. Higher-Order Ionospheric Effects on the GPS Observable and means of modeling them. *Advances in Astronautical Sciences*, 02, 1993.

[19] J.A. Klobuchar. Ionospheric Time-Delay Algorithm for Single-Frequency GPS users. *IEEE Transactions on Antennas and Propagation*, pages 325–331, 1987.

[20] A. Aragon-Angel, R. Orus, M. Amarillo, M. Hernandez-Pajares, J. Juan, and J. Sanz. Preliminary NeQuick assessment for future single frequency users of Galileo. In *Proceedings of the 6th Geomatic Week*, 2005.

[21] R. Notarpietro, F. Dovis, G. De Franceschi, and M. Aquino, editors. *Mitigation of Ionospheric Threats to GNSS: an Appraisal of the Scientific and Technological Outputs of the TRANSMIT Project*. InTech, 2014.

[22] Y. Beniguel, V. Romano, L. Alfonsi, M. Aquino, A. Bourdillon, and P. Cannon. Ionospheric Scintillation Monitoring and Modeling. *Annals of Geophysics*, 52:183, 2009.

[23] SBAS Ionospheric Working Group. Ionospheric Scintillations: How Irregularities in Electron Density Perturb Satellite Navigation Systems. *GPS World*, 23(4):44–50, April 2012.

[24] P. Kintner and T.E. Humphreys. GNSS and Ionospheric Scintillation: How to survive the next solar maximum. *Inside GNSS*, July-August 2009.

[25] P. H. Doherty, S.H. Delay, C.E. Valladares, and J.A. Klobuchar. Ionospheric Scintillation Effects in the Equatorial and Auroral Regions. In *Proceedings of the 13th International Technical Meeting of the Satellite Division of the Institute of Navigation ION GPS 2000*, pages 662–671, September 2000.

[26] Su. BaSu, S. Basu, J.J. Makela, R.E. Sheehan, E. Mackenzie, P. Doherty, and J.W. Wright. Two components of ionospheric plasma structuring at midlatitudes observed during the large magnetic storm of October 30, 2003. *Geophysical Research Letters*, 32(12), June 2005.

[27] M.C. Kelley. *The Earth's Ionosphere: Plasma Physics & Electrodynamics*. Academic Press, 2nd edition, 2009.

[28] NASA. Heliophysics. the new science of the sun-solar system connection. Retrieved in February 2015 from http://sec.gsfc.nasa.gov.

[29] A.J. Van Dierendonck and H. Quyen. Measuring Ionospheric Scintillation Effects from GPS Signals. In *Proceedings of the 57th Annual Meeting of The Institute of Navigation*, pages 391–396, 2001.

[30] R. Xu, Z. Liu, M. Li, Y. Morton, and W. Chen. An Analysis of Low-Latitude Ionospheric Scintillation and Its Effects on Precise Point Positioning. *Journal of Global Positioning Systems*, 11:22–32, 2012.

[31] C.L. Rino. A power law phase screen model for ionospheric scintillation: 1. Weak scatter. *Radio Science*, 14:1135–1145, 1979.

[32] A.J. Van Dierendonck. Evolution of Modernized GNSS Ionospheric Scintillation and TEC Monitoring. Workshop on Science Applications of GNSS in Developing Countries, May 2012.

[33] Luxembourg: Publications Office of the European Union. European GNSS (Galileo) open service: Signal in space interface control document. Technical report, European Union, 2010.

[34] E.J. Fremouw and C.L. Rino. An empirical model for average F-layer scintillation at VHF/UGH. *Radio Science*, 8:213–222, 1973.

[35] ITU-R Recommendation P.2097-0: Transionospheric radio propagation. The Global Ionospheric Scintillation Model (GISM), 2007.

[36] B. Forte and S.M. Radicella. Comparison of ionospheric scintillation models with experimental data for satellite navigation applications. *Annals of Geophysics*, 48(3), 2005.

[37] E.J. Fremouw and J.A. Secan. Modeling and scientific application of scintillation results. *Radio Science*, 19:687–694, 1984.

[38] T.E. Humphreys, M.L. Psiaki, , and P.M. Kintner. Modeling the Effects of Ionospheric Scintillation on GPS Carrier Phase Tracking. *Aerospace and Electronic Systems, IEEE Transactions on*, 46(4):1624–1637,

October 2010.

[39] T.E. Humphreys, M.L. Psiaki, J.C. O'Hanlon, and P.M. Kintner. Simulating Ionosphere-Induced Scintillation for Testing GPS Receiver Phase Tracking Loops. *Selected Topics in Signal Processing, IEEE Journal of*, 3(4):707–715, August 2009.

[40] J.G. Proakis and M. Salehi. *Communication System Engineering*. Prentice Hall International Editions, 1994.

[41] K. Borre, D.M. Akos, N. Bertelsen, P. Rinder, and S.H. Jensen. *A Software-Defined GPS and Galileo Receiver*. Birkhäuser, 2007.

[42] G. Crowley, G.S. Bust, A. Reynolds, I. Azeem, R. Wilder, B.W. O'Hanlo, M.L. Psiaki, S. Powell, T. Humphreys, and J. Bhatti. CASES: A Novel Low-Cost Ground-based Dual-Frequency GPS Software Receiver and Space Weather Monitor. *Proceedings of the ION GNSS*, 2011.

[43] X. Rui, Z. Liu, M. Li M. Li. Morton, and W. Chen. An Analysis of Low-Latitude Ionospheric Scintillation and Its Effects on Precise Point Positioning. *Journal of Global Positioning Systems*, 11(1):22–32, 2012.

[44] S. Peng and Y. Morton. A USRP2-based reconfigurable multi-constellation multi-frequency GNSS software receiver front end. *GPS Solutions*, 2012.

[45] Septentrio. Septentrio satellite navigation. http://www.septentrio.com/.

[46] PF. De Bakker, J. Samson, P. Joosten, M. Spelat, M. Hoolreiser, and B. Ambrosius. Effect of radio frequency interference on GNSS receiver output. In *ESA workshop on satellite navigation user equipment technologies. NAVITEC, ESA/ESTEC, Noordwijk (NL)*, 2006.

[47] F. Dovis, L. Musumeci, B. Motella, and E. Falleti. *GNSS Interference, Threats and Countermeasures: Classification of Interfering Sources and Analysis of the Effects on GNSS Receiver*. Artech House, 2015.

[48] L. Musumeci, F. Dovis, and J. Samson. Performance comparison of transformed-domain techniques for pulsed interference mitigation. In

International Conference on Localization and GNSS (ICL-GNSS), 2013.

[49] L. Musumeci and F. Dovis. Performance assessment of wavelet based techniques in mitigating narrow-band interference. In *International Conference on Localization and GNSS (ICL-GNSS)*, 2013.

[50] R.J. Landry and A. Renard. Analysis of potential interference sources and assessment of present solutions for GPS/GNSS receivers. In *4th Saint-Petersburg on INS*, 1997.

[51] P. Craven, R. Wong, N. Fedora, and P. Crampton. Studying the Effects of Interference on GNSS Signals. In *ITM Proceedings*. The Institute of Navigation, 2013.

[52] R.H. Mitch, R.C. Dougherty, M.L. Psiaki, S.P. Powell, B.W. O'Hanlon, J.A. Bhatti, and T.E. Humphreys. Signal Characteristics of Civil GPS Jammers. In *ION GNSS*, 2011.

[53] Septentrio. GNSS Interference . Retrieved on 21/01/2015 from http://www.insidegnss.com/elib-chipsets.

[54] M. Wildemeersch, E. Cano Pons, A. Rabbachin, and J. fortuny. Impact study of Unintentional Interference on GNSS Receivers. Technical report, European Comission Joint Research Center, 2010.

[55] D. Symeonidis, J. Fortuny-Guasch, C. O'Driscoll, and A. Belenguer. Scintillation Parameter Estimation Using Unmodified Professional GNSS Receivers: A Feasibility Study. In *Proceedings of the 24th International Technical Meeting of The Satellite Division of the Institute of Navigation (ION GNSS 2011)*, September 2011.

[56] R. Romero and F. Dovis. Effect of Interference in the Calculation of the Amplitude Scintillation Index S4. *International Conference on Localization and GNSS (ICL-GNSS)*, 1:25–27, 2013.

[57] A.S. Balaei, B. Motella, and A. Dempster. A preventive approach to mitigating CW interference in GPS receivers. *GPS Solutions*, 12:199–209, 2008.

[58] J. Jang, M. Paonni, and B. Eissfeller. CW Interference Effects on Tracking Performance of GNSS Receivers. *IEEE Transactions on Aerospace and Electronic Systems*, 48(1), 2012.

[59] J. Zhang and E-S. Lohan. Effect of Narrowband Interference on Galileo E1 Signal Receiver Performance. *International Journal of Navigation and Observation*, page 10, 2011.

[60] L. Musumeci and F. Dovis. *GNSS Interference, Threats and Countermeasures: Classical Digital Signal Processing Countermeasures to Interference in GNSS*. Artech House, 2015.

[61] F.. Camoriano D BoDovis and L. Lo Presti. Two Pole and Multi Pole Notch Filters: A Computationally Effective Solution for GNSS Interference Detection and Mitigation. *IEEE Systems Journal*, 2(1):38–47, 2008.

[62] A.V. Oppenheim and R. Schafer. *Discrete-Time Signal Processing*. Pearson Education, 2006.

[63] L. Musumeci and F. Dovis. *GNSS Interference, Threats and Countermeasures: Interference Mitigation Based on Trasformed Domain Techniques*. Artech House, 2015.

[64] L. Musumeci and F. Dovis. Use of Wavelet Transform for Interference Detection and Mitigation in GNSS. *International Journal of Navigation and Observation*, page 14, 2014.

[65] P.P. Vaidyanathan. *Multirate SySystem and Filter Banks*. Prentice-Hall, 1993.

[66] S. G. Mallat. Theory for multiresolution signal decomposition: the wavelet representation. *IEEE Transactions on Pattern Analysis and Machine Intelligence*, 7(7):674–693, 1989.

[67] University of Nottingham. http://ipdm.nottingham.ac.uk/.

[68] H. Sato, N. Hlubek, and M. Aquino. *The concept of the TRANSMIT prototype-network based service for mitigation of ionospheric threats*. InTech, 2014.

[69] Lopez-Salcedo J., Peral-Rosado J., and Seco-Granados G. Survey on Robust Tracking Techniques. *IEEE Communications Surveys and Tutorials*, 12:77–86, 2013.

[70] Fantinato S., Rovelli D., and P. Crosta. The switching carrier tracking loop under severe ionospheric scintillation. In *6th ESA Workshop on Satellite Navigation Technologies and European Workshop on GNSS Signals and Signal Processing, (NAVITEC)*, 2012.

[71] Chiou T., Gebre-Egziabher D., Walter T., and Enge P. Model analysis on the performance for an inertial aided FLL-assisted PLL carrier tracking loop in the presence of ionospheric scintillation. In *Proceedings of the 2007 National Technical Meeting of The Institute of Navigation*, 2007.

[72] S. Skone, G. Lachapelle, Yao W., and Watson R. Investigating the Impact of Ionospheric Scintillation using a Software Receiver. In *Proceedings of ION GPS/GNSS*, pages 1126–1137, 2005.

[73] Brown R.G. and Hwang P.Y. *Introduction to Random Signals and Applied Kalman Filtering.* John Wiley and Sons, 1997.

[74] M. Susi, M. Aquino, R. Romero, and F. DovF. Dovis. Andreotti. Design of a robust receiver architecture for scintillation monitoring. In *Position, Location and Navigation Symposium - PLANS 2014, 2014 IEEE/ION*, pages 73–81, May 2014.